PREPARATION AND CHARACTERIZATION OF SnO_2 THIN FILMS

AND

RADIATION DAMAGE STUDIES

PREPARATION AND CHARACTERIZATION OF SnO_2 THIN FILMS

and

RADIATION DAMAGE STUDIES

By

ENRICO GIANI

A Thesis

Submitted to the Faculty of Graduate Studies

in Partial Fulfilment of the Requirements

for the Degree

Master of Science

McMaster University

June, 1971

MASTER OF SCIENCE (1971)
(Materials Science)

McMASTER UNIVERSITY
Hamilton, Ontario

TITLE: Preparation and Characterization of SnO_2 Thin Films and Radiation Damage Studies.

AUTHOR: Enrico Giani, Dottore in Fisica (Università degli Studi di Milano, Milano, Italy)

SUPERVISOR: Professor R. Kelly

NUMBER OF PAGES: X, 128

SCOPE AND CONTENTS:

Part One deals with thin films of SnO_2 which were prepared by ion-beam sputtering, reactive sputtering, and anodic oxidation. The films were found to be either amorphous or crystalline in their as-prepared state.

The structure of the as-deposited amorphous films, as revealed by transmission electron microscipy, presented interesting features: there was a continuous structure in the case of high-temperature deposition, whereas an "island structure" was revealed in the case of low-temperature deposition. Furthermore, heat treatment of films having an "island structure" showed this structure to be maintained provided the heating was done with unsupported films, while the structure became

continuous when heat treatment was performed on supported specimens.

The crystalline form of the films has been worked out, and found to generally be cassiterite; nevertheless a phase different from cassiterite has been occasionally noticed during this work. In some cases it could be tentatively identified as SnO, while in other cases it remains unidentified. Crystallization temperatures found here are somewhat different from those indicated in the literature, namely: 500, 300, 225°C according to substrate temperature and nature and type of heat treatment. Anodic oxidation of tin has been performed(apparently for the first time) in a non-solvent electrolyte, the films being consistently crystalline.

The results obtained in the case of films deposited on water-cooled substrates, have revealed a dependence of film structure on film thickness and this effect has been confirmed in supplementary experiments. Thus thick films appear to crystallize spontaneously at room temperature.

Part Two deals with radiation damage studies. Our experiments on krypton-ion bombarded SnO_2 films show that amorphous specimens remain amorphous following ion bombardment. The electron-microscope evidence of whether crystalline SnO_2 is amorphized by ion bombardment was tentatively negative, while the gas-release evidence was strongly negative.

Part Three deals with diffusion in inert-gas implanted SnO_2. In the first section we give the theoretical background that enabled

us to deduce from our experiments rough estimates of the melting temperature, self-diffusion temperature, and activation-energy for self-diffusion of the less mobile ion in SnO_2. In particular, we obtained the following results:

$T_{melting}$ = 2600 - 3000°K

$T_{self\text{-}diffusion}$ = 1480 - 1870°K for a 2 min. time scale and 134±44Å distance scale.

$\Delta H_{self\text{-}diffusion}$ = 87,200 - 131,000 cal/mole

Note that the melting point for tin oxide is variously reported in different handbooks to lie between 1400 and 2200°K. From a comparison with other work we have concluded that our value for ΔH is very likely that for oxygen-ion diffusion.

Acknowledgments

The author wishes to express his gratitude to Dr. R. Kelly for his kind and indispensable guidance throughout the course of this work.

The author also wishes to thank Dr. J.P. Marton (Welwyn Canada Ltd.,) for providing SnO_2 single crystal samples.

This project was supported by grants from the Defence Research Board and National Research Council of Canada to Dr. Kelly and from the Ontario Government and McMaster University to the author.

LIST OF ILLUSTRATIONS

LIST OF TABLES

TABLE OF CONTENTS

Part One

PREPARATION AND CHARACTERIZATION OF SnO_2 THIN FILMS

CHAPTER 1

Introduction

1.1

The great interest in Tin Oxide films for industrial applications has led to a considerable amount of work on its electrical and optical properties. Tin Oxide films have, for example, been used for anti-static coatings on glass, while tin-oxide coated panels are used as radiant heaters in drying ovens (Corning Glass Works, U.S.A.) and as heating elements in aircraft (Ward, 1955). The major interest, however, has been in the development of resistors and infrared reflectors, a broad study (Loch, 1963) of SnO_2-based compositions as semiconductors having been undertaken and more recently SnO_2 having been studied to improve the properties of thin film transistors of this material (Klasens and Koelmans, 1964). On the other hand, the literature is noticeably sparse about physical properties such as film structure, crystal growth, amorphousness, and diffusion in SnO_2 films.

1.2

Methods for preparing tin oxide films have been known for some time, and the patent literature is rich on this subject (Littleton, U.S. Pat. 2, 118, 795, McMaster, U.S. Patent 2, 429, 420; Libbey-Owens-Ford Glass Co., and McMaster, Brit. Pat. 632, 256, Oct. 1942.). The films are usually prepared by hydrolyzing a volatile tin compound on a hot surface (normally a glass substrate), e.g.

$$SnCl_4 + 2H_2O \xrightarrow{500\text{-}800^\circ C} SnO_2 + 4HCl,$$

a process closely analogous to that used to prepare SiC, SiO_2 and Si_3N_4 films for electronics applications.

For example, optically transparent and electrically conducting SnO_2 films were prepared by Ishiguro et al. (1958), by spraying aq. or alc. $SnCl_4 \cdot 5H_2O$ solution on substrates at 500-600°C. Substrates were glass, fused silica or NaCl cleavage plates. Groth et al. (1962), prepared layers of SnO_2 using the already mentioned spraying technique, by which a solution of $SnCl_4$ in butyl acetate is sprayed into a furnace held at a temperature of 550°C. The SnO_2 was deposited on glass or quartz plates. Powell et al. (1966) prepared SnO_2 thin films by the hydrolysis of stannic chloride on substrate heated to 650°C.

1.3

As an alternative to the chemical preparation of SnO_2 films, it was found by Preston (1950) that films deposited by sputtering of a tin cathode in an oxygen-containing atmosphere were identifiable by electron diffraction (reflection) as tin oxide. Holland and Siddal (1953) have also prepared tin oxide films by reactive sputtering. Their technique involved reaction of the cathode with oxygen before film deposition and sputtering was then done in a 95%Ar-5%O_2 atmosphere. As sputtered, films showed a very high resistance; upon baking to 400°C the conductivity was increased; a final resitivity of 3 kΩ/sq. was obtained, while the deposited film (15 minutes sputtering) had a resistance of about 500 kΩ/sq.

1.4

Still a further alternative is vacuum evaporation. Thus Shiojiri et al. (1966) prepared SnO_2 films by vacuum evaporation from a tungsten basket onto the surface at NaCl cleavages at room temperature. The deposited films showed structurless microscopic images and gave rise to an amorphous pattern in electron diffraction. Electron irradiation of the

order of 0.01 to 0.10 amperes/cm^2 made in the electron microscope by using a large condenser lens aperture or by removing it, was necessary for obtaining a crystallized product. The amorphous tin oxide film was found to crystallize into fine granules as did rutile prepared in the same way. Spence (1967) obtained SnO_2 films by the evaporation of tin (99.999%) from a tungsten boat under a $2x10^{-5}$ to $2x10^{-4}$ Torr partial pressure of oxygen onto glass substrate at 300°C. Chin (private communication) prepared vacuum deposited tin oxide films, the substrate material being of quartz. The author observed a factor of 10^7 decline in electrical resistance upon baking at 150°C.

1.5

A fourth class of film-preparation technique is the one by which oxides are prepared on substrates of the parent metal. The simplest method of doing this is by anodization. As the name implies, the film is made to grow on the anode in an electrolytic cell, the basic equations that govern the process being often written as,

$$M + nH_2O \rightarrow MO_n + 2nH^+ + 2ne \quad \text{at anode} \qquad (1a)$$

$$2ne + 2nH_2O \rightarrow nH_2\uparrow + 2nOH^- \quad \text{at cathode} \qquad (1b)$$

Thus, an oxide grows on the metal anode surface and hydrogen is evolved at the cathode. With some materials this may not be the anodizing reaction, with the metal of the anode instead going into solution or oxygen being evolved. Electrolytes used for anodizing can be broadly divided into two groups, (i) those which have solvent action on the oxide and (ii) those which have limited or no solvent action on the oxide. In solvent electrolytes the oxide growth continues as long as potential is applied

to the electrodes since the oxide coating is rendered porous by the solvent action of the electrolyte. In the non solvent type of electrolyte, the film grows to form a "glass like" coating which acts as a barrier to further oxidation.

The anodization current can, under these circumstances, be readily shown to be given approximately by,

$$i \simeq A \exp [-(\Delta H - qaV/x)/kT] + i_{electronic} \qquad (2)$$

where:

V/x = electric field

q = charge on the current-carrying ion

a = distance from minimum to maximum potential energy ("half barrier width")

ΔH = activation energy at zero field

The current thus decreases rapidly with time, and an apparently limiting film thickness results which is dependent only upon the applied voltage. 1.6

As far as we know, nobody has so far prepared SnO_2 films by anodic oxidation of metallic tin in a non-solvent electrolyte. Thanks to Mr. M. Arora, however, who suggested a novel electrolyte, we have been able to prepare SnO_2 films that, stripped and observed in the electron microscope, could be shown to be continuous and stable. This will be discussed in detail later (section 3.11).

1.7

It is worth emphasizing that in all these experiments, sprayed or anodized layers showed a crystalline structure of the material, whereas evaporated layers showed an amorphous structure (van der Maesen and Witmer, 1963) This suggests that the

SnO_2 system will show certain complications not shared by other oxides.

1.8

Of closest interest to the present research are the results obtained by reactive sputtering, since this has mostly been the preparation technique we have used. Besides the examples referred to earlier (section 1.3), Sinclair and Peters (1963) prepared tin oxide films by reactive sputtering, a tin electrode being sputtered in oxygen. If we assume the oxide films to be formed by reaction between metallic tin and gaseous oxygen at the substrate, the basic reactions may be assumed to be (Hollands and Campbell, 1960):

$$\text{Site} + \tfrac{1}{2}O_2 \rightleftharpoons O - \text{chemisorbed}$$

$$O - \text{chemisorbed} + Sn \xrightarrow{\text{absorption}} Sn/O \text{ solid solution.}$$

The formation of oxidized films depends upon the incorporation of oxygen-atoms into the growing metal film. Only oxygen-atoms which have energy above that of the activation energy for the absorption process will succeed in reacting. At any given temperature, and at a constant rate of metal deposition, the degree of oxidation of the sputtered films therefore increases with the partial pressure of oxygen, according to the formula:

$$[O^-]_{\text{chemisorbed}} = \frac{Kp_{O_2}^{1/2}}{(RT)^{1/2}}$$

Similarly Jackson et al. (1966) found that the highest oxidation state in lead-titanium oxide films was not achieved unless sputtering was performed in pure oxygen. By contrast, Valletta and Pliskin (1967), studying the manganese oxygen system, found that (above $1\%O_2$) the composition

of the sputtering gas made very little difference to the stoichiometry of the film (as well as to the deposition rate); stoichiometry was found to depend almost exclusively on the substrate temperature.

Returning to work by Sinclair and Peters, films deposited in unheated substrates were determined to be amorphous, as indicated by electron diffraction results on the unsupported films and by X-ray diffraction results on supported films. On heating the films to 400°C or higher, the writers found that films crystallized to the rutile-like structure of cassiterite with an average crystalline diameter of about 400Å. Amorphousness of deposited films and heating-induced crystalline structure have been confirmed by Sinclair et al. (1965).

Vainshtein (1965) obtained SnO_2 films by sputtering of a tin cathode in an Ar-O mixture, the structure being polycrystalline, as dictated by electron diffraction patterns. Lieberman and Medrud (1969) prepared oxide films of eleven metals by reactive sputtering. The use of a refrigerated (liquid nitrogen) substrate, to decrease the atomic mobility (especially that involved in surface diffusion), resulted in amorphous films in eight of the metal oxide systems including Sn. Reactive sputtering was performed in a nominally 1:1 argon-oxygen mixture. Films of tin oxide were again confirmed to crystallize as the rutile analog of SnO_2. Specifically amorphous SnO_2 heated for 1 hour at 250°C gave cassiterite-type SnO_2. The same authors report that Sarjeant and Roy (1967) have examined the phases of metal oxides obtained from splat cooling and other rapid quenching techniques and were unable to prepare amorphous SnO_2. Yamanaka and Oohashi (1969) prepared SnO_2 films by ion-beam sputtering of a SnO_2 cathode. Films were sputtered in different gases, i.e. A, O_2, N_2, Air. All films were composed of crystallites of approximately 100Å in size, of which the structure was the same rutile type (i.e. cassiterite) as that of the bulk material. Electron diffraction patterns of the films exhibited preferred

orientation in (001) plane.

The reader will have noted at this point the continuing confusion in the literature is to the crystal state of the SnO_2 films. This confusion is not merely of academic interest but lies at the heart of using SnO_2 as a semi-conductor, for the conductivity of a solid is strongly dependent on whether it is crystalline (Mogab and Kingery, 1968; Kennedy et al., 1967).

1.9

Some attractive features of reactive sputtering are: (a) high purity oxides can be obtained, (b) film thickness can be varied and controlled rather easily, (c) films have excellent adherence to different substrates, (d) temperature of deposition can be maintained quite low and (e) mixed oxides can be prepared by nonpreferential alloy sputtering (or else using multiple cathodes).

CHAPTER 2

THE SPUTTERING PROCESS

2.1 The Mechanism of Sputtering

2.1.1.

Before giving the details of our experimental procedure and results, it may be worth while to give a general idea about the phenomenon of sputtering, since this has been the main tool of our research.

Sputtering is the term describing the ejection of atoms from a solid surface under the impact of high velocity ions. The momentum of impacting ions is transferred to the surface atoms, ejecting them with fairly high velocities of their own. The ejected atoms can thus be deposited on a substrate, providing a method of constructing thin films atom by atom. Since sputtering is a non-evaporative process, high-melting point materials like tantalum and tungsten, and even ceramics, can be deposited without difficulty.

2.1.3

In actual practice a solid surface is bombarded with particles of high kinetic energy, usually in excess of 1000 electron volts. Usually heavy ions are used, since such particles have high sputtering yields. In Table I are reported the data obtained by Rosenberg and Wehner (1962), showing a comparision of sputtering yields (atoms/ion) for He^+, Kr^+, and Xe^+-ion bombardment. Noble-gas ions are commonly used in sputtering, as well as in radiation damage studies, due to operational problems. Noble-gases have the further advantage of being chemically inert, i.e. zero valence in the target. Besides, irradiation with nucleons often results in

a nuclear reaction having inert gas as the final product. Kr and Xe for example form 33% of fission products in nuclear reactors, while He, Ar and Kr commonly result from (n,α) or (n,p) reactions:

$$B^{10}\ (n,\alpha)Li^{7}$$

$$K^{41}\ (n,p)Ar^{41}$$

If the conditions are right, we can eject atoms from the surface of the target so that they will travel to a secondary surface, or substrate, and form a film there. Researchers have found that, in sputtering, the material is always transferred in the same composition, except for an initial transient (Gillam, 1959), so that the deposited films have the same composition as the original target, even if that target is some complex alloy.

TABLE I

Sputtering Yields for 30 Elements under He^{+}, Kr^{+} and Xe^{-} Ion Bombardment. Numbers in Brackets are Doubtful due to Surface Layers.

	Helium				Krypton				Xenon			
Target	100 (ev)	200 (ev)	300 (ev)	600 (ev)	100 (ev)	200 (ev)	300 (ev)	600 (ev)	100 (ev)	200 (ev)	300 (ev)	600 (ev)
Be	(0.040)	(0.095)	(0.15)	(0.34)	0.03	0.17	0.24	0.61	···	0.12	0.24	0.42
C	0.008	0.020	0.035	0.085	0.005	0.045	0.090	0.18	···	0.04	0.08	0.21
Al	···	0.005	0.008	0.021	0.09	0.30	0.52	1.11	0.06	0.24	0.45	1.02
Si	0.015	0.045	0.075	0.15	0.05	0.12	0.23	0.64	···	0.08	0.21	0.51
Ti	0.010	0.038	0.05	0.08	0.03	0.16	0.29	0.53	···	0.13	0.24	0.50
V	(0.003)	(0.020)	(0.038)	(0.09)	0.06	0.21	0.35	0.69	0.05	0.20	0.39	0.72
Cr	0.030	0.070	0.105	0.20	0.21	0.56	0.88	1.55	0.13	0.44	0.85	1.90
Mn	···	···	···	···	0.11	0.40	0.69	1.80	0.08	0.44	0.60	1.67
Fe	0.030	0.065	0.09	0.17	0.12	0.38	0.64	1.23	0.06	0.29	0.54	1.20
Co	0.010	0.042	0.075	0.15	0.08	0.30	0.50	1.33	0.09	0.38	0.61	1.30
Ni	0.028	0.060	0.095	0.18	0.16	0.47	0.75	1.50	0.10	0.37	0.71	1.48
Cu	0.045	0.11	0.16	0.27	0.33	0.92	1.42	2.80	0.26	0.79	1.29	2.44
Ge	0.010	0.03	0.05	0.08	0.12	0.37	0.66	1.35	0.08	0.31	0.54	1.20
Zr	···	(0.004)	(0.013)	(0.025)	0.04	0.18	0.34	0.72	0.03	0.18	0.31	0.71
Nb	···	0.005	0.010	0.030	0.03	0.17	0.30	0.68	0.02	0.17	0.31	0.61
Mo	(0.001)	(0.005)	0.015	0.040	0.07	0.32	0.54	1.05	0.06	0.28	0.51	1.06
Ru	···	···	···	···	0.08	0.45	0.77	1.45	0.05	0.37	0.71	1.42
Rh	0.004	0.015	0.030	0.065	0.16	0.54	0.90	1.70	0.12	0.51	0.84	1.60
Pd	0.020	0.057	0.082	0.16	0.33	0.97	1.47	2.55	0.34	0.93	1.39	2.48
Ag	0.030	0.082	0.125	0.23	0.40	1.35	1.85	3.90	0.40	1.05	1.80	4.20
Hf	···	···	(0.002)	(0.010)	0.12	0.39	0.59	1.02	···	0.30	0.55	1.17
Ta	···	0.002	0.003	0.012	0.07	0.33	0.53	0.98	0.05	0.32	0.50	1.00
W	···	0.001	0.004	0.008	0.06	0.36	0.58	1.07	0.03	0.35	0.60	1.18
Re	···	···	···	···	0.08	0.42	0.74	1.43	0.02	0.31	0.80	1.40
Os	(0.0005)	(0.002)	(0.004)	(0.022)	0.05	0.39	0.73	1.45	0.03	0.39	0.74	1.53
Ir	···	(0.001)	(0.003)	(0.010)	0.10	0.42	0.66	1.58	0.05	0.52	0.86	1.79
Pt	···	0.004	0.010	0.035	0.15	0.67	1.15	2.11	0.19	0.72	1.25	2.23
Au	···	0.020	0.035	0.08	0.42	1.10	1.90	3.42	0.16	1.00	1.83	3.10
Th	···	(0.0005)	···	(0.002)	0.09	0.36	0.60	1.07	0.08	0.35	0.60	1.22
U	···	0.002	0.004	0.013	0.14	0.47	0.79	1.46	···	0.24	0.45	1.00

This ability to deposit material without influencing its composition is one of the distinct advantages of sputtering over evaporation; in fact SnO_2 cannot be formed by evaporation unless O_2 is present due to the reaction:

$$SnO_2 = SnO_x + \frac{2-x}{2} O_2$$

Notice, however, that this does not mean that the properties of the target material remain unchanged after sputtering deposition. This may be so, depending upon whether or not we create the right conditions at the substrate so that arriving atoms can migrate on the surface into the right crystal structure. This depends on both the substrate temperature, the nature of the substrate, and the ambient pressure.

2.1.3

At this point we should explore briefly what is going on at the fundamental level in order to see what the main controlling parameters are.

First, a quick look at the physical setup, which is quite simple in its conceptional form. The items involved are:

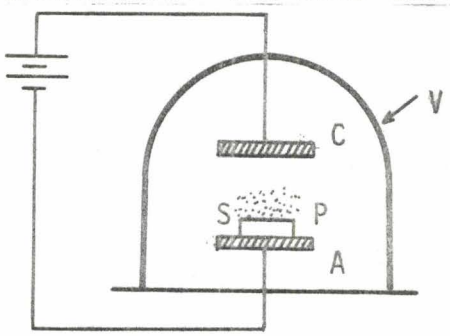

V = Vacuum chamber
C = Cathode (target)
A = Anode
P = Plasma
S = Substrate

a cathode and an anode for establishing a gas-discharge plasma; a source of sputtered material (which is the same as the cathode in this case); and a substrate, the deposition site. All these are housed in a chamber evacuated to a pressure of anywhere from 1 to 100 militorr. A voltage of from 500 to 5,000 volts between cathode and anode is sufficient to generate the plasma and induce sputtering. Positive ions from the plasma

are attracted to the cathode (target) by the large cathode potential and, in doing so, gather enough energy to induce physical disintegration of its surface.

This is the simplest arrangement for so-called dc sputtering. In other systems, the ion plasma is generated by radio frequency fields or with the help of a thermoionic cathode. Also specially designed sources of ions can be used to provide a more concentrated stream of ions than the essentially random ion source represented by the glow discharge around a cathode.

2.1.4.

Let us now visualize a solid surface consisting of atoms bound together by certain forces. Our projectile first approaches this target surface as an ion, but because the electric field between the ion and the metal surface becomes very high, the ion pulls out a field-emitted electron and becomes actually neutralized before impact ("Auger" neutralization). The ion strikes a surface atom, and this atom transfers the impact to one of its neighbours which, in its turn, impacts others.

2.1.5.

What we must accomplish is to optimize this interaction so that there are just enough collisions between just enough partner atoms to change the net direction of the momentum transfer and knock an atom out in the opposite direction, that is, to make an atom leave the surface. One of the important factors in this optimization is the kinetic energy of the impinging particle. Clearly, the higher this energy is, the more atoms we can dislodge per ion, a number we call the sputtering yield. If, however, we try for excessively high energies (by increasing the accelerating voltage higher and higher), then our impact kinetic energy penetrates deeper into the lattice, the major part of the momentum transfer occurs

in the interior, and our sputtering yield begins to drop off (Fig. 1).

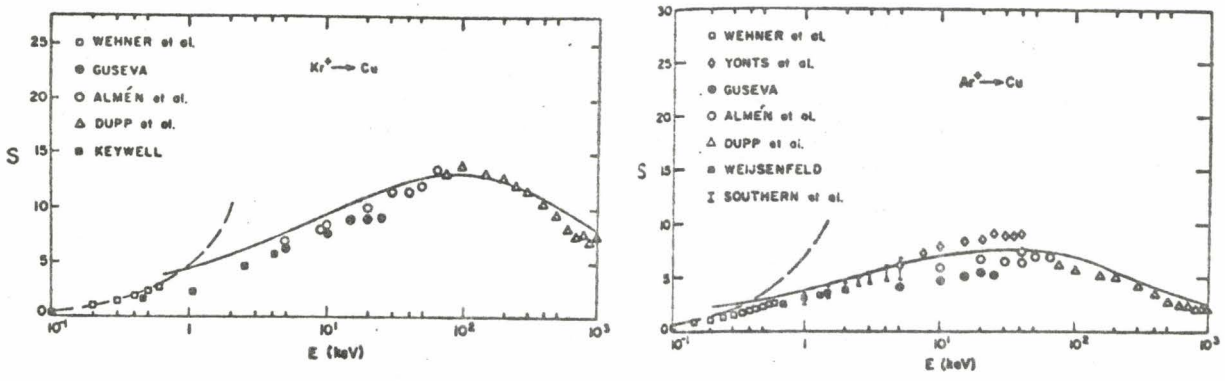

(a) (b)

Fig. 1. (from Sigmund, 1969). Calculated sputtering yields compared with experimental results, (a) Kr^+ ions; (b) Ar^+ ions.

As we carry the impact energy closer to the 100,000-volt level, the result is primarily lattice damage, either temporary or permanent; most of our energy appears as heat in the target and virtually no sputtering is taking place. One can easily understand that a second factor plays a role: the angle of incidence of the bombarding particle. A third one is the masses of the collision particles: the most favorable energy transfer condition is when the masses of the two are similar (cfr. Table I), as is clear from the relation for energy transferred in a head-on collision: $E_2 = \frac{4M_1M_2E_1}{(M_1+M_2)^2}$. A further one is the electron configuration of the target atom. The high yield from metals like gold and silver are mainly attributable to the fact that atoms of these metals have more closed electron shells than those in the center columns of the periodic table, that is they are "harder" and more elastic than atoms of metals whose electron orbits are not completely filled.

Putting these various effects together leads to a simple empirical

sputtering theory, due originally to Rol et al. (1960). Thus we have

$$S = K \cdot \frac{4M_1M_2}{(M_1+M_2)^2} E \cdot \frac{1}{R} \cdot \frac{1}{\cos\chi} \qquad (3)$$

where χ is the angle of incidence, K is a fitting constant and R is a range parameter such as the median range.

The last important parameter concerns how strongly the surface atoms we want to dislodge are bound to their neighbours. This binding energy, E_b, is similar to the heat of atomization (Nghi and Kelly (1970)) and it stretches from about 3 electron volts for materials like copper, silver and gold up to 8-9eV for tungsten. Sigmund has shown that the surface binding energy enters eq.(3) to the power E_b^{-1}.

2.1.6.

Finally it is worth noticing that sputtered atoms have been found to come off the target surface mostly in the close packed directions of the crystal.

Until about 1953 the preferred theory stated that sputtering was an evaporation process such that when a fast-moving ion hit the surface, a localized spot of very high temperature was formed and the material then evaporated from there. Now we are convinced that sputtering is essentially a momentum transfer process unless the target is heated to near the evaporation temperature (Nelson, 1965). The improvement in sputtering yield under conditions of oblique incidence, its reduction in open crystallographic directions and the success of Sigmund's theory have been instrumental in helping to solidify this view of the sputtering process.

2.1.7.

So far, we have focused on the disintegration of the target material under ion bombardment. Let's look now briefly at what happens at the

substrate or deposition site.

2.1.8.

Provided we work at gas pressure low enough, gas-phase scattering is minimized and the atoms travel unimpeded, as in vacuum evaporation, to the substrate.

Sputtered atoms are ejected with fairly high kinetic energy, 50 to 100 times higher than in vacuum evaporation. The fact that sputtering provides higher arrival velocities has certain consequences with respect to film formation. For one thing, higher speed means that the atoms bring with them a certain kinetic energy for reacting with the substrate or for diffusion together to form the same compound again. For another, we may have at the substrate a certain amount of secondary sputtering, the arriving atoms driving off some of the substrate, thus cleaning the substrate and promoting adherence.

This matter of adhesion is not very well understood as yet, although it is an established fact that sputtered films adhere far more strongly to many substrates than films deposited by other techniques such as vacuum-evaporation or plasma-spraying. It appears that the very first atoms that arrive at the substrate, by virtue of their high kinetic energy, may in fact penetrate some layers more deeply providing a tight link to the substrate lattice. But this is largely conjecture, and more careful experimental work needs to be done, comparing, say, vacuum evaporation with sputtering, to see what the influence of the high kinetic energy of the arriving atoms really is.

We already mentioned that the transferred material has the same composition, except for an initial transient, as it had before we began disintegrating our target. This point can be explained in this way:

when we sputter an alloy, for example, at the onset the constituent which has the lowest sputtering yield will become enriched on the target surface, while that with the highest yield becomes momentarily depleted. But if we keep the target cold enough, there can be no diffusion of the depleted constituent from the interior, and thus it cannot be replenished at the surface. Very quickly an equilibrium condition is reached, and from there on the material is transferred in the same composition. The transient situation has been shown in the Cu_3Au to involve 30-80Å. The situation is quite different with vacuum evaporation, since diffusional replenishment tends to prolong the initial transient.

2.1.9.

The last feature we may note about the sputtering process is the deposition rate, which is quite low. The low deposition rates in sputtering arise from the fact that when we bombard a surface with ions, the major part of the energy really appears as heat in the target, and only a small part goes into kinetic energy of the ejected atoms.

This can be demonstrated qualitatively in terms of the Edgeworth expansion for deposited energy. Thus, the amount of energy deposited at depth x in a random solid is given by:

$$C(x)dx = (dx)(2\pi\mu_2)^{-1/2}(\exp[-\xi^2/2])(f[\xi]) \qquad (4)$$

where

$$\mu_n = \langle(x - \langle x\rangle)^n\rangle, \quad \xi = (\langle x\rangle/\mu_2^{1/2})(\frac{x}{\langle x\rangle} - 1),$$

and $f(\xi)$ is a series containing higher-order moments. The point is that the values of $\langle x_d\rangle$, $\mu_{2d}^{1/2}$, etc, are such that only a small part of $C(x)dx$ lies between $x = -\infty$ and $x = 0$.

The deposition rate we expect from sputtering ranges from 50 to

10,000 angstrom per minute, so sputtering is useful for thicknesses up to, but not beyond, the micron range.

2.2 Reactive Sputtering

A special aspect of this deposition method is so-called reactive sputtering, that is, sputtering of a metal or semiconductor electrode in an oxidizing (or other) atmosphere. The general technique and ideas involved in reactive sputtering have been well described by Holland (1956). The technique of preparing sputtered oxide films is quite straightforward, whereas the chemical and physical processes operating during deposition are extremely complex.

When a metal cathode is sputtered in oxygen the following oxidation mechanisms may operate simultaneously: (i) production of an oxide layer on the cathode surface which is removed under positive ion bombardment; (ii) oxygen absorption by the sputtered atoms in transit; (iii) oxygen absorption by the sputtered film during its formation.

Usually in reactive sputtering the residual gas is a mixture of inert gas plus oxygen, and a simple explanation of the role of these two components would be that whereas the ionized oxygen molecules mainly combine with the cathode metal to form an oxide, the ionized inert-gas molecules utilize their energy in sputtering.

More details about the basic process of sputtering are in many articles included in the following volumes:

Advances in Electronics and Electron Physics, Academic Press, Vol. 7, 1955 (by G. Wehner, p. 239).

Ibid, Vol. 17, 1962 (by E. Kay, p. 245).

Ergebnisse der exacten Naturwissenschaften, Springer, Berlin 1964 (by R. Behrisch, p. 295, in German).

Atomic and Ionic Impact Phenomenan, Springer, 1965 (by H. Kaminsky, p. 142).

Two experts in sputtering theory, Harrison of the Naval Postgraduate School, Monterey, Calif., and Sigmund of the University of Aarhus (Denmark), presented summary lectures at the July 1968, Gordon Research Conference on Particle-Solid Interactions. Part of this material has since appeared in Phys. Rev. 184, (1969), 383.

A survey which emphasizes the deposition of thin films, by Maissel, appeared in Physics of Thin Films (Academic, Vol. 3, 1966).

A handbook of Thin Film Technology, edited by Maissel and Glang, has been published by McGraw-Hill, and contains up-to-date information on thin-film deposition.

CHAPTER 3

Experimental and Results

3.1 General Comments

3.1.1

We have prepared SnO_2 films by the following techniques:

1) ion-beam sputtering of sintered SnO_2 pellets
2) reactive sputtering of Sn in a D.C. glow discharge
3) stripping of SnO_2 films from anodically oxidized tin.

The as-deposited films were amorphous in the case of reactive sputtering when deposited on KCl substrates either at $\sim$ -100°C or at $\sim$ +200°C, and when deposited on SnO_2 single crystals.

They were partially amorphous in the case of ion-beam sputtering of SnO_2 pellets, independently of the explored range of temperature of the SnO_2 target.

SnO_2 films were found to be polycrystalline in the case of anodically oxidized tin and in the case of deposition by reactive sputtering on water cooled substrates and on sintered SnO_2 pellets.

3.1.2.

For each of the mentioned preparation techniques, films have been examined by electron microscopy under the following conditions:

a) as prepared
b) heated in air: (i) stripped and heated, (ii) heated on their supports
c) heated in a vacuum

Heating in a vacuum was carried on inside the electron microscope, using either the heating stage or electron-beam heating.

3.1.3.

Subsequent to heat treatment of supported and unsupported films, their structure has been analysed in relation to substrate nature, since films have been deposited variously on KCl, SnO_2 single crystal and SnO_2 pellets.

The crystalline form of the films has been worked out, and found to be cassiterite: nevertheless a phase different from cassiterite has been noticed during the development of our investigation and will be discussed later (section 3.8). We suspect that it may be SnO.

In general the crystallization temperatures and crystalline structure found here for SnO_2 were somewhat different from those indicated in the literature, and explanations will be given for this.

3.2. Ion-beam sputtering of sintered SnO_2 pellets.

3.2.1.

The SnO_2 used as starting material (cathode target) was a disc made from cold pressed powder sintered at 1100°C in air for 2 hours.

This material was sputtered with natural Krypton ions using an 1-40 KeV high-current ion accelerator, the target arrangement of which is shown in Fig. 2.

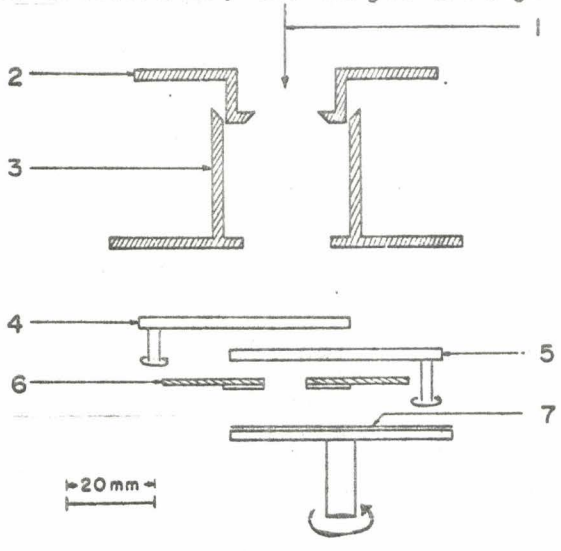

Figure 2. Target arrangement used for sputtering SnO_2 pellets: (1) ion beam; (2) 14 mm. defining iris; (3) centering piece, serving also as electron suppressor; (4) shutter; (5) Zn_2SiO_4 fluorescent screen; (6) Al disc with pieces of KCl attached; (7) Sintered SnO_2 pellet.

The substrates, which were KCl cleavings, were mounted as shown in the figure.

In this type of accelerator the ion plasma is generated by a high frequency (77 MHz) field. The plasma is established between an anode and a cathode, positive ions being extracted from the plasma by applying a positive voltage, with respect to the cathode (i.e. extraction canal), to a probe within the plasma. Those ions are then further accelerated to the target, so that they bombard its surface and sputter atoms from it. A magnet is placed at the position where ions leave the plasma, providing in this way intensification of the plasma. Intermediate electric lenses are placed on top of the target, and are held at a potential slightly more negative than the target itself, to avoid that field emitted electrons from the target give wrong (higher) values of the ionic current.

3.2.2.

SnO_2 is an insulating material; if we bombard an insulator with a stream of ions, the surface would quickly become positively charged and, unless the charges could be drained away, sputtering would have to cease because the accelerating stream of ions could not be maintained. One solution for this problem (not used here) is to sputter with a radio-frequency technique. What is done is to place a metal plate behind the insulator, which we want to sputter, and apply to it an r-f signal in the megacycle range. Then, during one half of the cycle, positive ions are brought in to bombard the surface, and during the other half of the cycle electrons are brought in to neutralize the surface charges. Thus the surface of the insulator is ready again for bombardment on the next half cycle.

3.2.3.

We overcame the problem of SnO_2 being an insulating material by putting close to the target a tungsten filament emitting thermoelectrons. As shown in the sketch, the filament circuit was grounded thru the target meter:

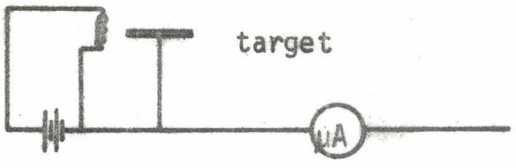

In this way we have been able to obtain ionic currents of 30-60 μA, a background pressure of about $1x10^{-6}$ torr, and an ion energy of either 4 or 5 KV.

We have already mentioned that Yamanaka and Oohashi (1969) prepared SnO_2 films by ion-beam sputtering, the target material being SnO_2 pressed and sintered powder. They don't give details of the experimental technique, except for values of 4.5 KV of the applied voltage and gas pressure of $3x10^{-2}$ torr. They claim that films obtained were composed of crystallites with a rutile-type structure.

3.2.4.

We obtained, in samples of the same sputtering, both amorphous as well as crystalline regions (Fig. 3(a) and (b)), possibly due to temperature gradients in the supports where films have been collected. The crystalline structure has been analyzed from Fig. 3(b). We have measured the radius of the concentric rings appearing in the diffraction pattern; we know that $\frac{R_n}{R_{n+1}} = \frac{d_{n+1}}{d_n}$ where R_n is the radius of the n-th ring measured on the photograph, and d_n is the value of the interplanar

spacing of the set of planes giving in the diffraction pattern a ring of radius R_n. Therefore we can in this way go back to the type of crystalline structure. In our case it turned out to be cassiterite. A comparison of our diffraction data with the ASTM data for SnO_2 is given in Table II.

3.2.5.

Assuming that in our photograph the 3rd ring is actually a superposition of 2 rings of radius R_3 and R_4 very close to each other, Table II shows that it is quite reasonable to assume that our polycrystalline films have a cassiterite structure.

TABLE II

Diffraction Data for Tin Oxide

Tin Oxide Films	SnO_2 (cassiterite) ASTM 5-0467
$R_1/R_2 = 0.792$	$d_2/d_1 = 0.787$
R_3/R_2 } $= 1.13$ R_4/R_2	$d_2/d_3 = 1.114$ $d_2/d_4 = 1.142$
$R_5/R_2 = 1.248$	$d_2/d_5 = 1.245$
$R_6/R_2 = 1.496$	$d_2/d_6 = 1.495$
$R_7/R_2 = 1.575$	$d_2/d_7 = 1.578$
$R_8/R_2 = 1.663$	$d_2/d_8 = 1.66$
$R_9/R_2 = 1.763$	$d_2/d_9 = 1.765$

3.2.6.

A different phase appears in Fig. 4. We are going to meet again, in the development of our research, this kind of diffraction pattern, and we'll deal with it later on (section 3.8).

3.2.7.

In a subsequent series of experiments, a modification of the

target arrangement has been made to keep the target itself refrigerated (a copper rod with one end connected to the target support, and the other end extending out of the bombarding chamber to a dewar of liquid nitrogen). Also in this case we have obtained either amorphous or crystalline films and also either cassiterite or a different phase. Thus, heating the amorphous product inside the microscope by pulse heating gave rise to a crystalline structure (cassiterite), as shown in Fig. 5. Other samples appeared crystalline as deposited (Fig. 6), or could be made to crystallize by heating at 350°C inside the microscope by the heating stage (Fig. 7). The crystal structure here (Fig. 6 & 7) was not cassiterite, however, but rather similar to that appearing in Fig. 4.

3.2.8.

The uncertainty on the structure state of films as deposited, the quite troublesome technique of sputtering an insulating material, and the desire to explore different deposition methods, indicated that we should try another way to obtain amorphous SnO_2 films.

3.3 Reactive Sputtering Deposition

3.3.1.

Thin films of SnO_2 suitable for transmission electron microscopy were next prepared by reactive sputtering. For the present investigation, an apparatus has been appositely constructed which has provisions for either refrigeration or heating of substrates. This sputtering equipment is substantially the simple scheme previously described, the so-called diode type (section 2.1.3.). The diode is made up of an upper cathode disc, from which we sputter, and a lower anode disc which is put parallel to it and on which we put the substrates. We simply establish between these discs a glow discharge.

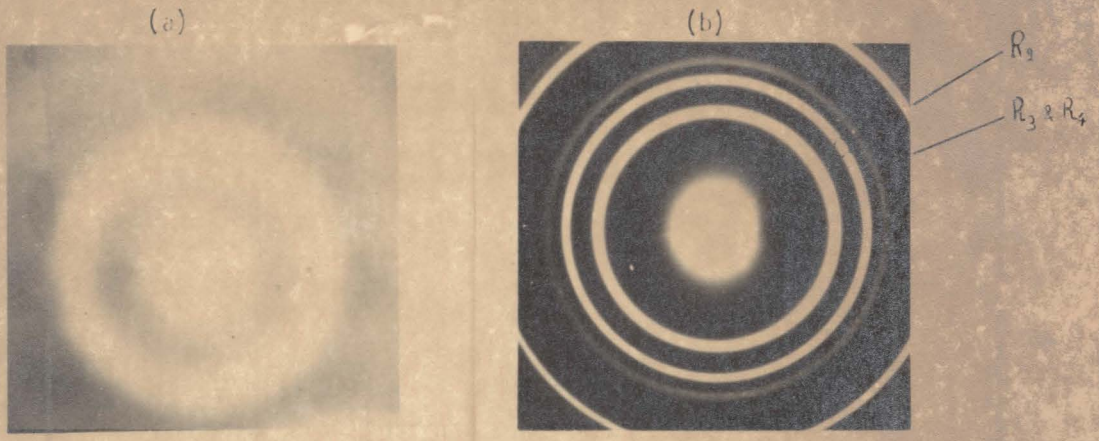

Figure 3. Diffraction Patterns (100 KV) of films obtained by ion beam sputtering of SnO_2 pellet.

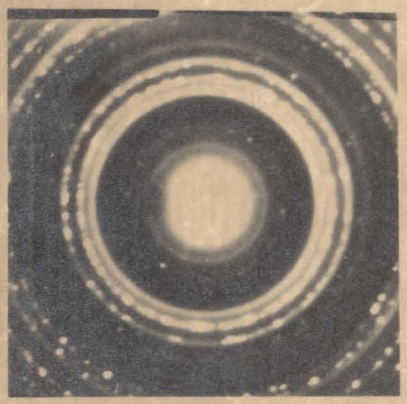

Figure 4. Diffraction Pattern (100 KV) of films obtained by ion beam sputtering of SnO_2 pellet, showing a different structure than in Figure 3(b).

Figure 5. Diffraction Patterns ((a) 80 KV, (b) 60 KV) of films obtained by ion-beam sputtering of SnO_2, with cooled target. (a) as deposited (b) after pulse heating.

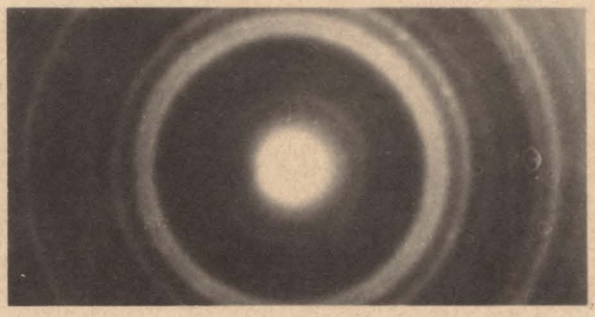

Figure 6. Diffraction Pattern (60 KV) of film obtained by ion-beam sputtering of SnO_2 (cooled target).

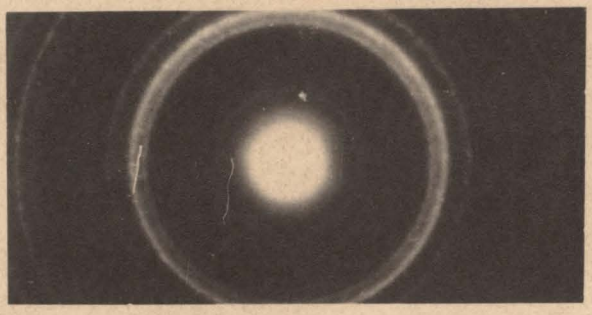

Figure 7. Diffraction Pattern (60 KV) of film obtained by ion-beam sputtering of SnO_2 powder (cooled target). Film heated inside microscope (heating stage) to 350°C.

3.3.2.

The cathode was approximately 50 mm. in diameter and 7 mm. thick. It was prepared from 99.90 per cent pure tin (Allied Chemical). The metal was melted into a pyrex dish where it solidified; tin does not stick to pyrex. During melting an aluminum screw was suspended above the center of the disc so that the screw head was embedded in the solid metal, but the threads were still available for attachment to a copper rod which served as vacuum seal, electrical conductor, and heat dissipator (the latter to avoid target melting during bombardment). The substrate on which the film was to be deposited was simply laid on the anode table. A thermocouple touching the bottom of the anode table was used to measure the temperature of the metal in contact with the substrates. It did not necessarily indicate the exact temperature where the film was deposited as there were probably thermal gradients across the anode and the insulating substrates (due, e.g., to the kinetic energy of sputtered particles, estimated to be several eV/atom as well as due to the temperature of the plasma). The interelectrode distance was about 30 mm. and the dark space region of the discharge usually extended about 20 mm. away from the cathode. A shutter was provided to permit presputtering of the target before the films were deposited on the substrate.

3.3.3.

The gas mixture used could be varied by adjusting valve controls. The chamber was evacuated to 10^{-6} torr. and then the pressure of the gas mixture was adjusted to $\sim 10^{-2}$ torr.

When a mixture of argon and oxygen was used, it was normally 50-50. Applied voltages ranged from 2000 to 3000. The current, depending on gas pressure and voltage, usually ranged from 3 to 10 mA.

In our arrangement a meter was put between the ground and the top

sealing plate of the vacuum chamber, to read the current lost from the top of the cathode (Fig. 8), i.e. the useful current was given by the difference of the meter readings.

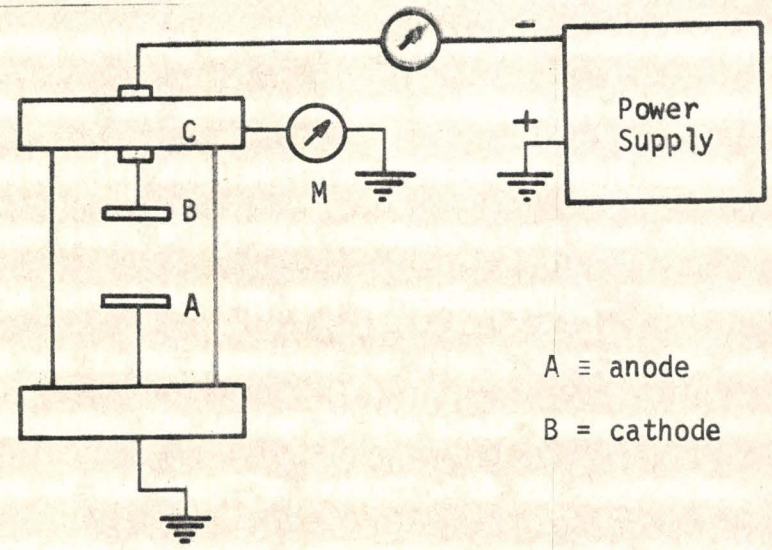

Figure 8. Sketch of our reactive sputtering chamber showing meter (M) to read the current lost from the top of the cathode.

3.4 Deposition on liquid-nitrogen cooled substrate; unsupported during heating in air.

3.4.1.

Our cooling device allowed for substrate temperatures of about -100°C during sputtering. As soon as we let the gas mixture flow into the vacuum chamber, the temperature at the anode increases slightly from a maximum negative value of -170°C; it reaches subsequently, during bombardment, a steady value of about -100°C. Voltages of 2KV and a current of 3-4 mA have been used. The sputtering time has been about 1 hour.

3.4.2.

The sputtered deposit was collected on KCl cleavings. Deposition

on KCl was followed by solution of the salt in water and films were directly mounted on grids for examination in a Philips EM300 microscope operated either at 80 or 100 KV.

As seen in Fig. 9 (a) the films showed, as deposited, a rather spectacular "island structure" with a typical island spacing of 0.05μ. In addition there is tentative evidence for discontinuities on a scale of 50 Å within the islands. In a further experiment, under the same sputtering conditions, the films showed humps possibly caused by vaporization of absorbed water on KCl substrate (see Fig. 9(b)). They disappeared during the crystallization process.

In both cases electron diffraction pattern showed an amorphous structure of the deposited film (see Fig. 10(b)). The apparent particle size in the amorphous film was estimated from the half-width of the halos in the diffraction pattern to be > 1 Å.

3.4.3.

The crystallization of amorphous SnO_2 was investigated by heat treatment of unsupported films in air.

Specimens held either in copper or molybdenum grids were heated isochronally in a furnace with hold times of 6 min. and with microscopic examination made after each heating; specimen holders were Cu-grids till about 450°C and Mo-grids for higher temperatures; separate specimens were used for each heat treatment. Tempeatures scanned were 100, 200, 300, 400, 450, 550, 650, 800, 900 and 1000°C.

In Fig. 10 the effect of heat treatment on the crystallization of a reactively sputtered film is shown. The upper row of transmission micrographed, (unfortunately, at different magnifications) illustrates the transition from an amorphous film on the left to a uniform and completely crystallized structure on the right. The corresponding electron diffraction

patterns of the same films are shown in the lower row. The diffuse bands of an amorphous phase are seen in the diffraction pattern for the as-sputtered film before heat treatment (Fig. 10(b)). A stage just before the onset of crystallization is seen after 6 min. at 450°C (Fig. 10(c)), the diffuse bands of the amorphous phase still being present (Fig. 10(d)). Nearly complete crystallization has occurred at 550°C (Fig. 10(e) and 10(f)), whereas slight crystal growth resulted at 650°C (Fig. 10(g) and 10(h)) and higher, i.e. 1000°C (Fig. 10(i) and 10(j)). The diffraction pattern after heat treatment retains rings of the polycrystalline phase together with a spotty pattern resembling that obtained from a single crystal. Thus, the effect of heating was to initiate the amorphous-crystalline transition at about 550°C; the corresponding diffraction pattern (Fig. 10(f)) retains halos of the amorphous phase, showing grain size comparable to that of Fig. 10(b); superimposed to halos are sharp rings typical of a much larger grain size. The microdensitometer we used to determine grain size, does not, unfortunately, reveal such rings.

3.4.4.

Further examination of the crystallization product was made following the same procedure outlined in section 3.2.4., on the electron diffraction pattern of a specimen heated at about 650°C (see Fig. 11(a)). It resulted in cassiterite, as deduced using the same arguments as in section 3.2.5. A comparison of the data obtained from Fig. 11(a) with the ASTM data for SnO_2 is given in Table III. From a comparison of either Fig. 11(a) with Fig. 11(b) or Table III with Table IV, it is seen that the film structure remains unchanged at a higher temperature, namely 800°C.

Fig. 12 shows micrographs at different (lower) magnification, of films subjected to the same treatment as those of micrographs of Fig. 10(c) and Fig. 10(g). The one micrograph shows that the amorphous films, though they have an island structure, are essentially planar. The other micrograph shows the extreme buckling caused by the crystallization process. This is as one would expect in view of the large density difference that

Table III

Diffraction Data for Tin Oxide

Tin Oxide Film (Fig. 11 (a))	SnO_2 (Cassiterite) ASTM 5-0467
$R_1/R_2 = 0.792$	$d_2/d_1 = 0.787$
R_3/R_2 } = 1.115	$d_2/d_3 = 1.114$
R_4/R_2 } = 1.115	$d_2/d_4 = 1.142$
$R_5/R_2 = 1.215$	$d_2/d_5 = 1.245$
$R_6/R_2 = 1.487$	$d_2/d_6 = 1.495$
$R_7/R_2 = 1.553$	$d_2/d_7 = 1.578$
$R_8/R_2 = 1.645$	$d_2/d_8 = 1.66$
$R_9/R_2 = 1.747$	$d_2/d_9 = 1.765$

Table IV

Diffraction Data for Tin Oxide

Tin Oxide Film (Fig. 11(b))	SnO_2 (Cassiterite) ASTM 5-0467
$R_1/R_2 = 0.792$	$d_2/d_1 = 0.787$
R_3/R_2 } = 1.125	$d_2/d_3 = 1.114$
R_4/R_2	$d_2/d_4 = 1.142$
$R_5/R_2 = 1.23$	$d_2/d_5 = 1.245$
$R_6/R_2 = 1.48$	$d_2/d_6 = 1.495$
$R_7/R_2 = 1.57$	$d_2/d_7 = 1.578$
$R_8/R_2 = 1.654$	$d_2/d_8 = 1.66$
$R_9/R_2 = 1.71$	$d_2/d_9 = 1.765$

normally exists being an amorphous and crystalline phase. Thus we have:

	$\rho_{am.}$	$\rho_{crystalline}$
Al_2O_3	3.12	3.99
MoO_3	4.52	4.69
Ta_2O_5	8.04	8.2
WO_3	6.8	7.16

Lastly, Fig. 13(a) and (b) show dark field equivalents of Fig. 12(b) and 10(i) respectively. These pictures show, which is not obvious from either bright field views or diffraction patterns, that the polycrystallinity of SnO_2 is on a fairly coarse scale (10^3-10^4Å, respectively).

3.5 Deposition on liquid-nitrogen cooled substrates; supported during heating in air

3.5.1.

The effect on progressive crystallization of heating the films directly on KCl supports is shown in Fig. 14, in which films heated on their substrates in air for hold times of 6 min. have been examined by transmission and diffraction electron microscopy.

3.5.2.

This procedure, of course, allows the reaction of the film with the substrate as an additional parameter (other important variables are: differences in chemical composition of the substrate, the heating time, the coefficient of thermal expansion of the substrate, the thickness of the film).

Sputtering and heating conditions were otherwise the same as before. Films were again wet-stripped and examined in the electron microscope, operated either at 80 or 100 KV. Temperatures scanned were 200, 300, 400°C;

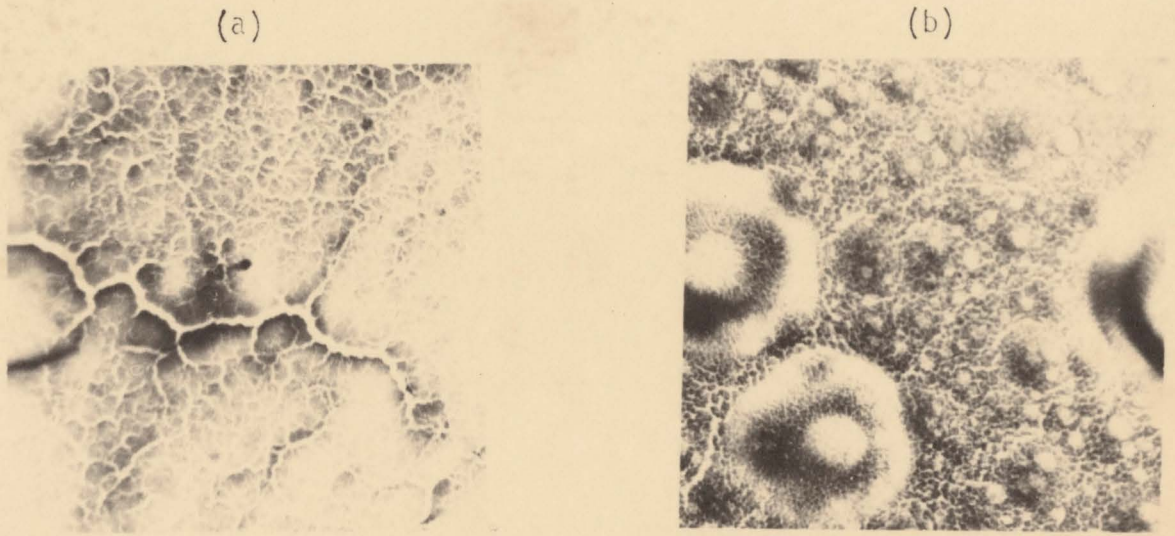

Figure 9. Transmission Electron Micrographs (80KV) of SnO_2 films prepared by reactive sputtering on refrigerated substrates.

(a) magn. 11,000

(b) magn. 43,000

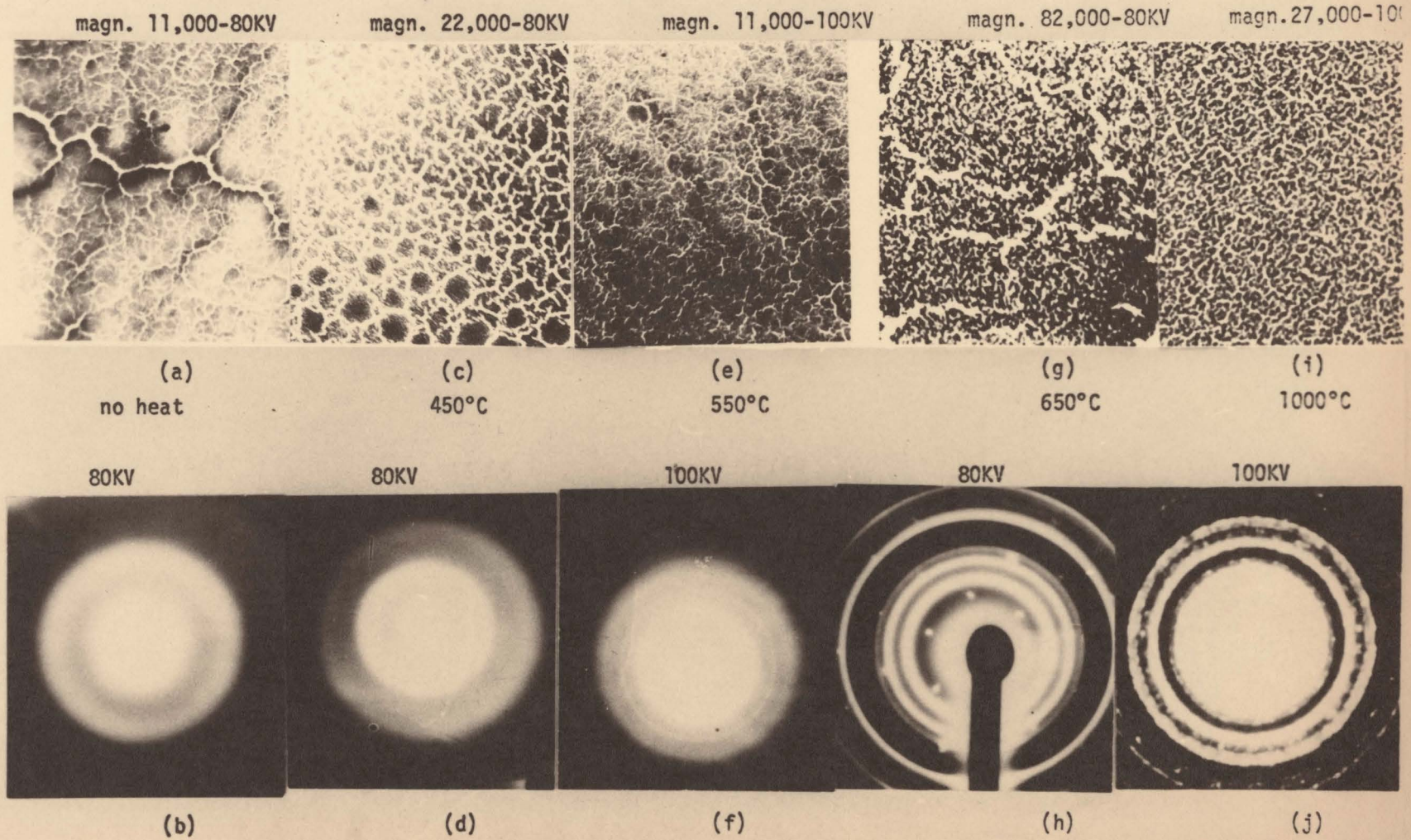

Figure 10. Effect of heat treatment in air on crystallization of reactively sputtered unsupported SnO_2 films.

Figure 11. Diffraction Patterns (a) 80KV, (b) 100KV) of specimens heated at 650°C (a) and 800°C (b).

Figure 12. Micrographs (80 KV) of same specimens as in Fig. 10(c) and Fig. 10(g), at different magnifications. (a) magn. 11,000 (b) magn. 13,000

Figure 13. Dark field of Fig. 12(b) and of Fig. 10(i). (a) 80KV, (b) 100KV.

at the same time electron beam heating effect inside the microscope has been investigated. (The films turned out in fact to be very sensitive to beam intensity, a feature that had not been observed in films stripped from KCl before heating.)

There is a striking difference in the crystallization temperature, which is in this case 300°C (Fig. 14(d)). And, very significantly, the film structure, though it looks very irregular compared to the fairly regular island structure of unsupported films, is evidently continuous. This observation is important since a possible explanation for the drastic change in electron-beam senstivity and the lowering in crystallization temperature is one based on particle size. Polezhaev (1967) and Garvie (1965) have previously made such arguments with ZrO_2, claiming that cubic ZrO_2 is stable if the particle size is small. Similarly, Hollands and Campbell (1968) conclude that Ta is stable as f.c.c. rather than the usual b.c.c., in thin films. The present work suggests, similarly that the diffusional activation energy involved in the crystallization of SnO_2 is larger for small particle sizes.

We do not regard this conclusion as necessarily contradicting the result that the dependence of chemical potential on radius is

$$\mu_r = \mu' + \frac{2\sigma v'}{r}$$

Thus an activation energy is the difference between the energy of an atom in the initial configuration and in the activated state, and could have either a negative or positive change as r decreases. (See Fig.13').

3.5.3.

The crystallization product at 300°C (Fig. 14(d)) has a particle size of 10^3 Å. Note that a particle size of 10^3 Å was revealed in unsupported films only after heat treatment at 650°C (section 3.4.4.).

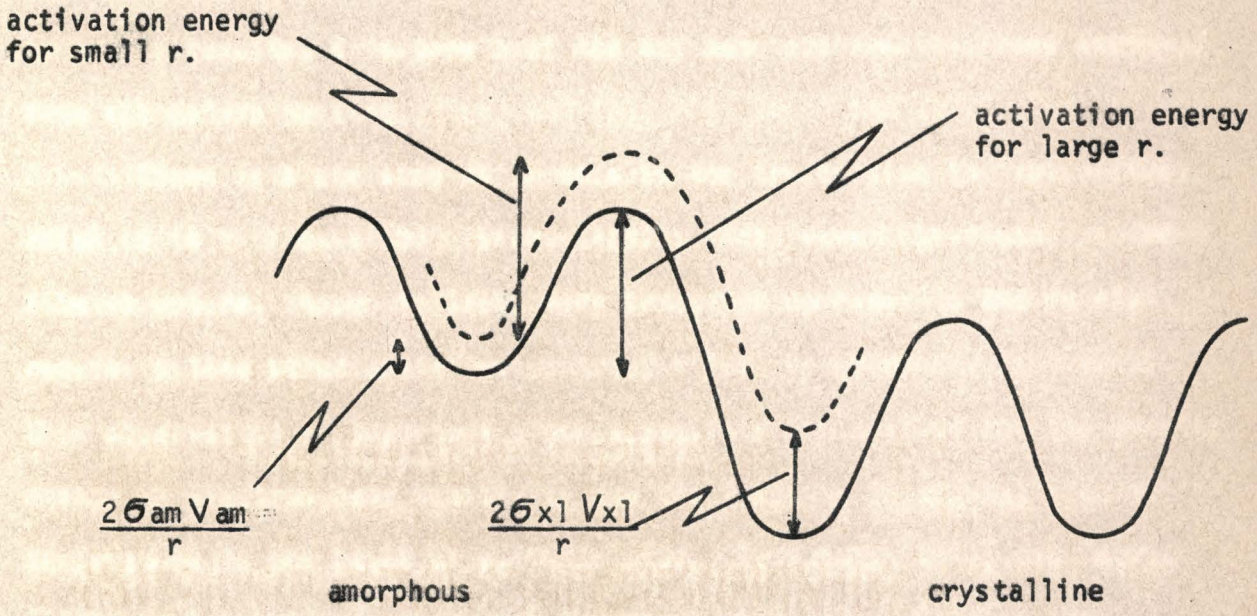

Figure 13' Atomic energy levels showing how the activation energy for crystallization could be increased by a decrease in particle size.

3.5.4.

An increase in the electron current of the microscope through the same area resulted in a growth of the crystal size and in a more extensive crystallinity (Fig. 15(a) and (b), Fig. 16(a) and (b)). The crystalline structure appears to be cassiterite, as seen in Fig. 14(f), 15(a), 16(b). Fig. 15(b), however, shows a different structure. We have already met this type of diffraction pattern (see Fig. 4), and we will return to this point later on.

3.6 Deposition on water cooled substrates

By a modification of the reactive sputtering system, we have provided for refrigerating the film substrates (anode) by running water.

We bombarded as usual using a 50-50 mixture of argon and oxygen, but we used this time a tension of 3KV, a current of 10 mA and a sputtering time of 2 hours, and would therefore expect a much thicker film. Cronologically this has been our first attempt to obtain amorphous SnO_2 films by reactive sputtering.

Since the films we obtained in this way were crystalline (Fig. 17) we didn't investigate further, and we switched first to liquid nitrogen cooled substrates (already discussed), and subsequently, in search of other types of films, to heated substrates.

It might be interesting to make new investigations at this substrate temperature, but with tension and current values changed to the standard ones we used later, in order to confirm the indicated dependence of film structure on film thickness.

Nevertheless, the picture seems compatible with what has gone before. In 3.4 we found discontinuous films to crystallize at about 550°C. In 3.5 we found thin continuous films to crystallize at about 300°C, while here we find that thick continuous films are already crystalline as deposited.

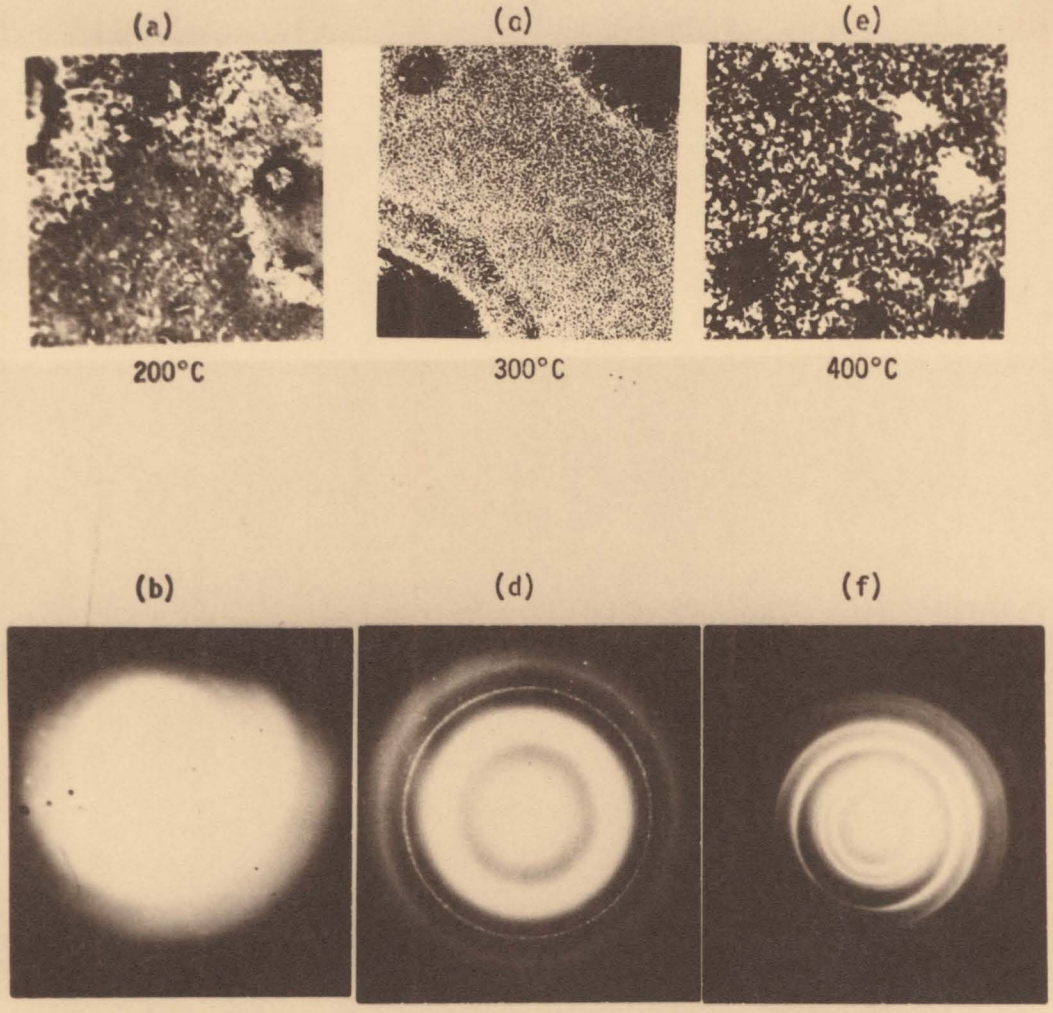

Figure 14. Effect of heat treatment in air on crystallization of supported SnO_2 films.

(b)(d) and (f) are diffraction micrographs of (a) (c) and (e) respectively.

(a) magn. 34,000 - 100 KV; (b) 100KV; (c) magn. 22,000 - 80 KV; (d) 80 KV; (e) magn. 22,000 - 80 KV; (f) 80 KV.

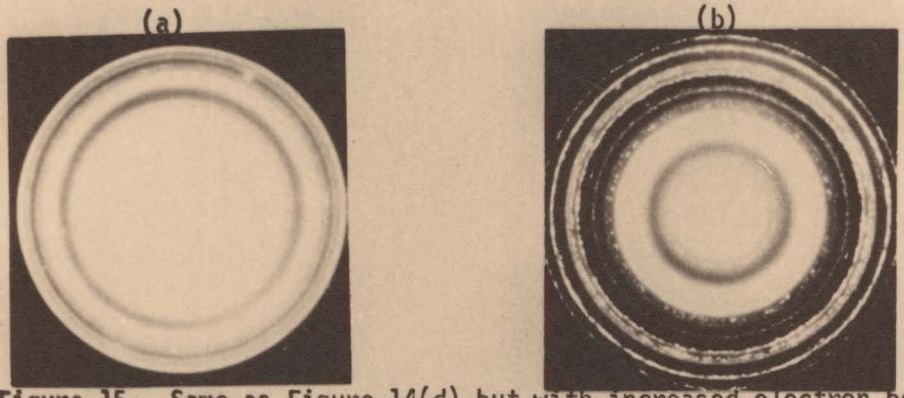

Figure 15. Same as Figure 14(d) but with increased electron beam heating. (temperatures unknown) (a) 100KV; (b) 80 KV.

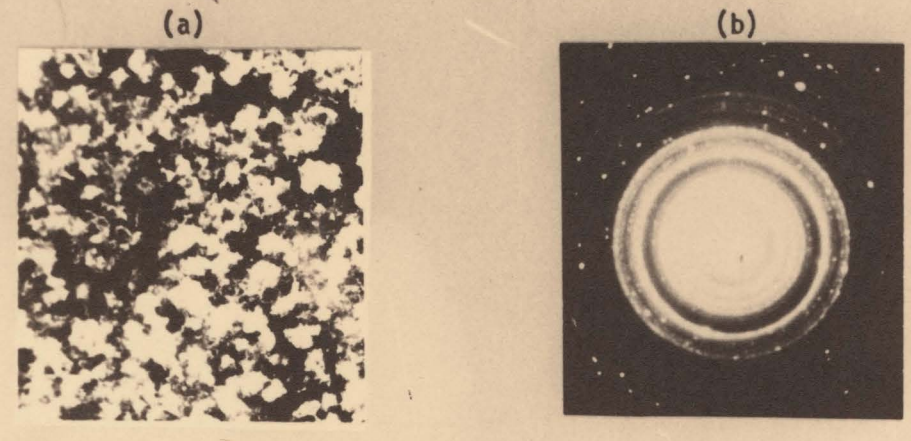

Figure 16. Same as Figure 14(e) and Figure 14(f) respectively, but with increased electron beam heating. (temperatures unknown)

(a) magn. 54,000 - 80 KV

(b) 80 KV

(a)

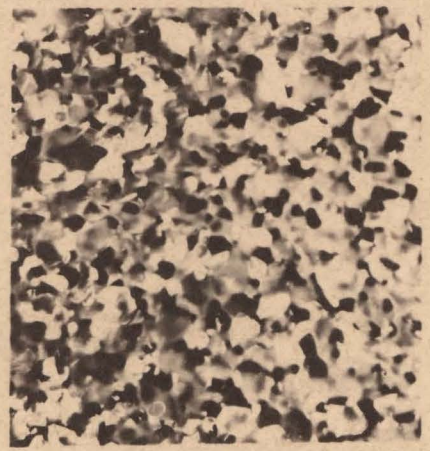

(b)

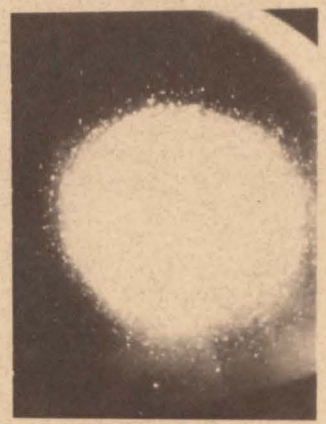

Figure 17. (a) Transmission electron micrograph and (b) electron diffraction pattern of SnO_2 film deposited on water cooled substrates.

(a) magn. 11,000 - 100 KV

(b) 100 KV

3.7 Deposition on heated substrates

3.7.1.

This is the way we got our best quality films, of compact and uniform structure, suitable for our subsequent radiation damage investigations.

Substrates were held at about 200°C during deposition. Films were deposited either on KCl, on SnO_2 single crystals, or on pressed and sintered SnO_2 pellets. A tension of 2 KV and a current of about 4 mA have been used, for a sputtering period of about one hour. The gas mixture was 50%Ar, 50%O_2.

3.7.2.

Films deposited on KCl were stripped in the usual way, and were found to be continuous as in 3.6 and as distinct from having an island structure as in 3.4. They presented a colour ranging from light yellow to transparent, which may be taken as showing they were not quite completely oxidized (Holland); this again constitutes a difference from lower temperature deposition. Concerning the matter of colour, Preston (1950) obtained, by cathodic sputtering, partially oxidized thin films of brown colour. Yamanaka and Oohashi (1969), who prepared SnO_2 films by D.C. glow discharge sputtering, noticed that sputtering in argon gave brown appearance to films, while films sputtered in oxygen were transparent. Chin (1969) vacuum deposited tin oxide films that showed, as deposited, a yellowish transparent colour. Baking at 500°C the yellow colour disappeared.

Thus when tin is sputtered in an argon plus oxygen mixture, at an elevated temperature the degree of oxidation of the deposit appears to depend, as would be expected, upon the relative concentration of the two gases. At high oxygen concentration completely oxidized tin layers are deposited which are optically transparent. When the partial pressure of the oxygen is of a low order, so that the sputtered film is incompletely

oxidized, the deposit ranges in colour from a light yellow to a deep brown. When such a partially oxidized layer is heated in air it becomes completely transparent.

3.7.3.

The colour is probably associated with bound electron states at point defects, possibly oxygen vacancies. According to Yamanaka and Oohashi, on the other hand, the brown appearance of the films means richer oxygen content than the stoichiometric ratio; during heat treatment in vacuum the oxygen ions escape, so the film changes to yellow brown. We regard this interpretation as wrong.

3.7.4.

It might be worth noting also, even if somewhat out of context, the dependence of the deposition rate on the percentage of oxygen and inert gas in the gas mixture. We already (section 2.2) said that a simple explanation for the role of the inert gas plus oxygen mixture would be that whereas the ionized oxygen molecules mainly combine with the cathode metal and/or sputter deposit to form an oxide, the ionized inert gas molecules utilize their energy solely in sputtering. For example, the data on the sputtering coefficients for O_2 and Kr bombardment of TiO_2 and Al_2O_3 reported by Kelly (1968) indicate that Kr is about twice as effective. Kubaschewski and Hopkins (1953) state that the presence of active oxygen does not increase the rate of formation of an oxide film above that of oxygen in its normal state. If the foregoing simplified treatment was correct then, as the ratio of oxygen to inert gas concentration increased, the rate of oxide formation on the cathode and/or sputter deposit would be greater but its rate of removal would decrease. This would appear to be confermed by Helwig (1952) who also reported that CdO-films were sputtered more rapidly in $Ar+O_2$ mixtures than in $N+O_2$ mixtures, and that the rate of

deposition fell as the oxygen content was increased in both cases. The greater deposition rate measured for argon is in keeping with its higher atomic weight than that of nitrogen. Williams et al. (1963), who used reactive sputtering by pure oxygen, noticed that the deposition rates obtained in this way were at least a factor of six lower than those obtainable with a 50-50 argon-oxygen mixture. Sinclair and Peters (1963) stated that when a 50-50 argon-oxygen mixture was used instead of pure oxygen the kinetics were accelerated considerably (fourfold increase); on the other hand they think that the increase in the deposition rate suggests that the sputtered material was oxidized at the point of deposition rather than at the cathode, in disagreement with the just mentioned authors.

3.7.5.

Somewhat surprisingly, the films we obtained were amorphous (Fig. 18), even if "less amorphous" than those obtained by deposition on low temperature substrates. The crystallization process was carried on with stripped films inside the microscope, using the heating stage. Samples were mounted on Mo-grids. The structure change versus temperature was therefore directly observed from the diffraction pattern evolution on the screen of the microscope. We have been able in this way to record structure changes corresponding to known values of the temperature.

3.7.6.

The temperature at which we noticed the onset of crystallization was 500°C (Fig. 19), essentially as found previously (section 3.4) with films showing an island structure. This may be a coincidence. Thus, notice that in the high temperature depositions, heating was carried on in vacuum. Furnace heating in air, as with the low temperature depositions, involves an oxygen containing atmosphere, while heating inside the microscope involves a hydrocarbon atmosphere. Therefore, in one case the crystallizing film is

hypostoichiometric, but not in the other.

3.7.7.

Films have also been examined at higher temperature (Fig. 20) till 800°C. At this temperature films broke and folded, and were unable to support themselves across the 70μ openings in the molybdenum grids. Remnants of film near the edge of an opening were analyzed at 800°C (Fig. 20). The fact that, by a comparison with films deposited on cooled substrates those formed at high temperature show a much less coherent structure was at first unexpected. This lack of coherence can probably be understood as relating to film geometry. Thus when the films are heated, crystallization and crystal growth set in at 500-1000°C and lead to general shape changes. These shape changes are easily accommodated by an island structure but lead to the rupture of a continuous film.

3.7.8.

Electron diffraction patterns show the usual cassiterite structure in vacuum heated films (Fig. 20(d) and 20(f)), while the same structure has also been found in films stripped and heated on Mo-grids in air in a furnace at 600°C for 10 min. (Fig. 21).

3.7.9.

Looking at Fig. 20(b), which is the diffraction pattern of a film heated inside the microscope till 550°C, we see that an inside extra line (with respect to cassiterite structure) is clearly visible. On the other hand, heating in the same way other specimens at higher temperatures, i.e. 600 and 700°C (Fig. 20(d) and 20(f)), no extra lines are noticed with respect to the cassiterite structure. Comparing Fig. 15(a) and Fig. 15(b) we can again notice the evolution from a cassiterite structure to a slightly different one, when electron beam heating is increased. On the other hand, increasing the electron beam heating on a sample previously heated in air

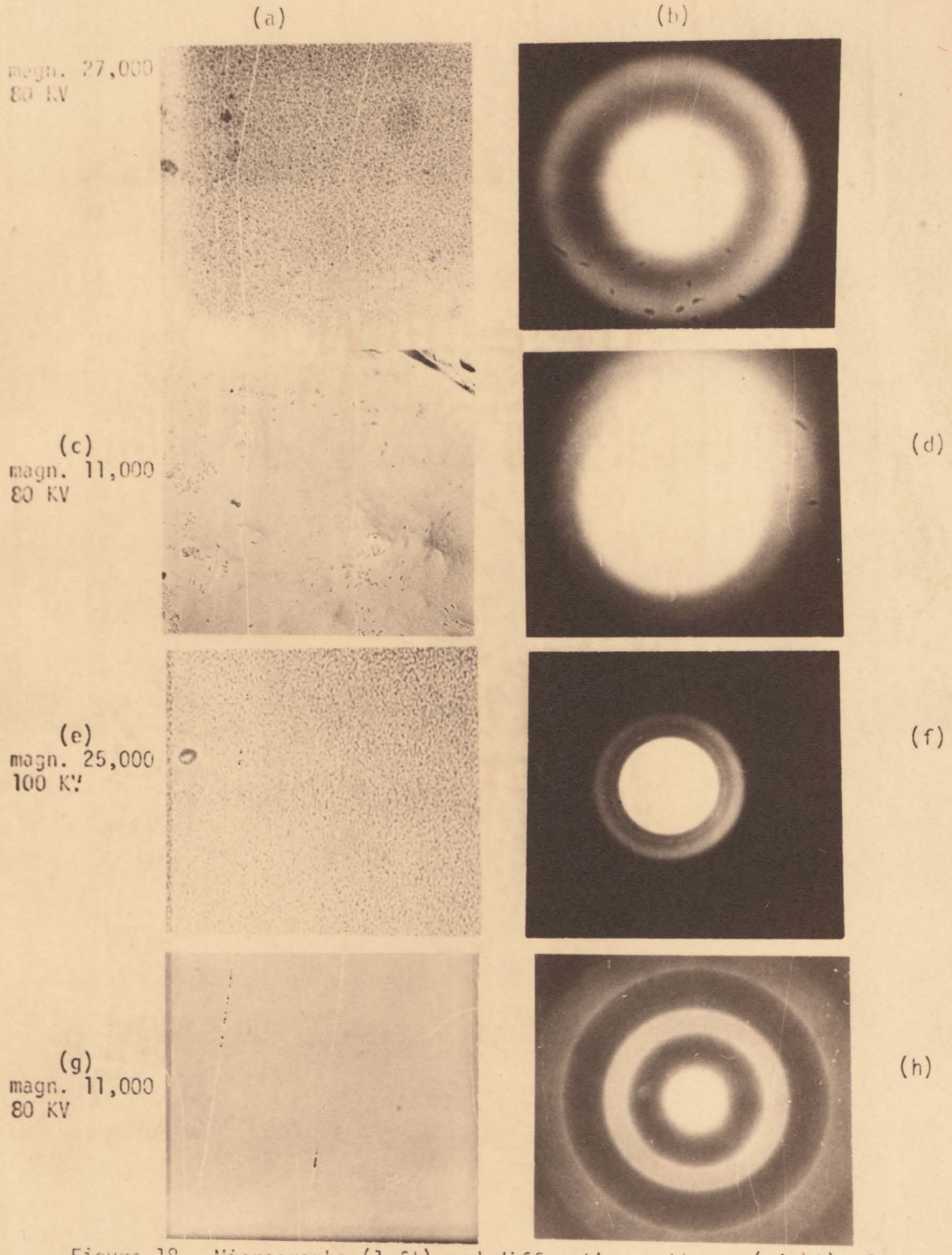

Figure 18. Micrographs (left) and diffraction patterns (right) of amorphous SnO_2 films deposited on KCl substrates at ~ 200°C.

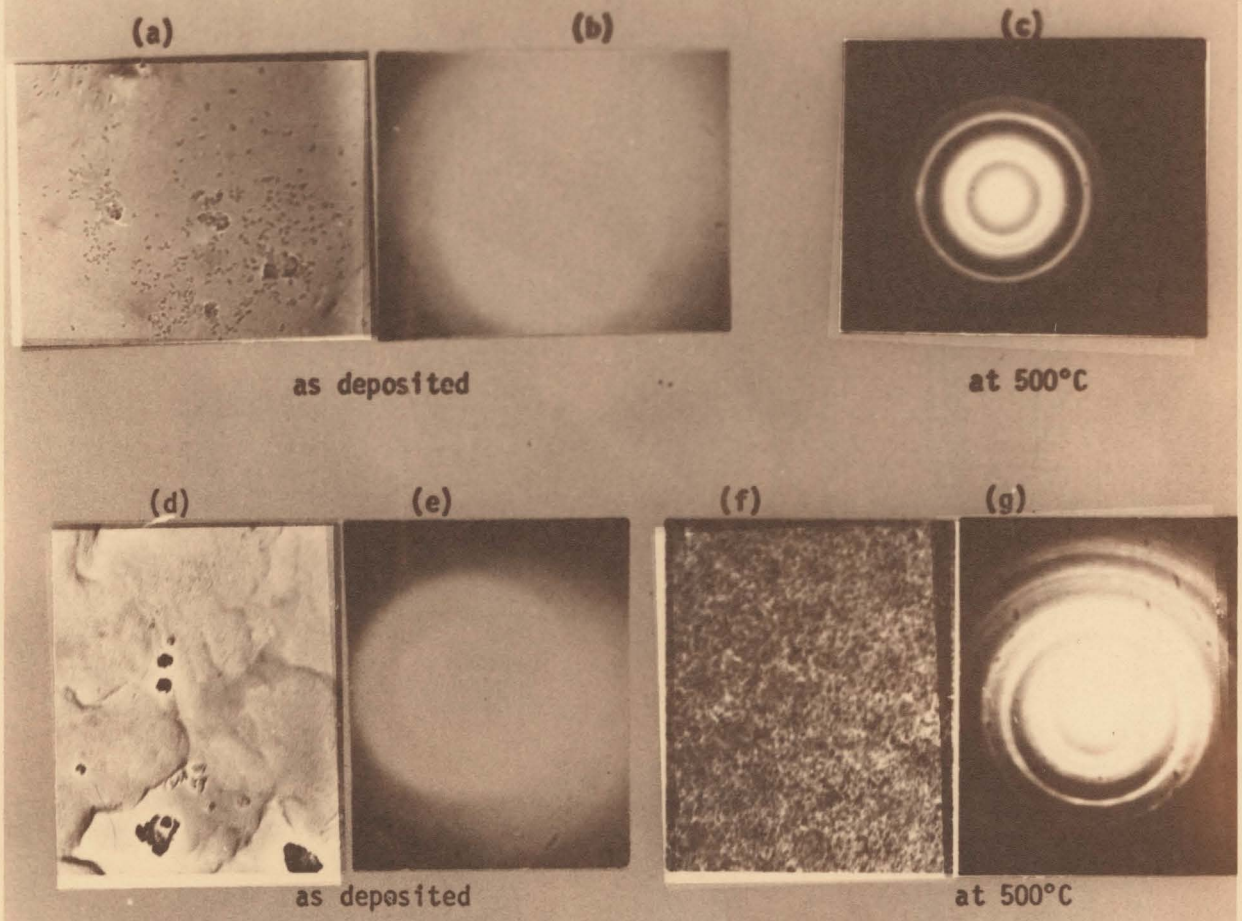

Figure 19. Micrographs and diffraction patterns showing onset of crystallization in samples deposited on heated substrates and subsequently heated inside microscope by heating stage. Magn. 11,000 - 80 KV.

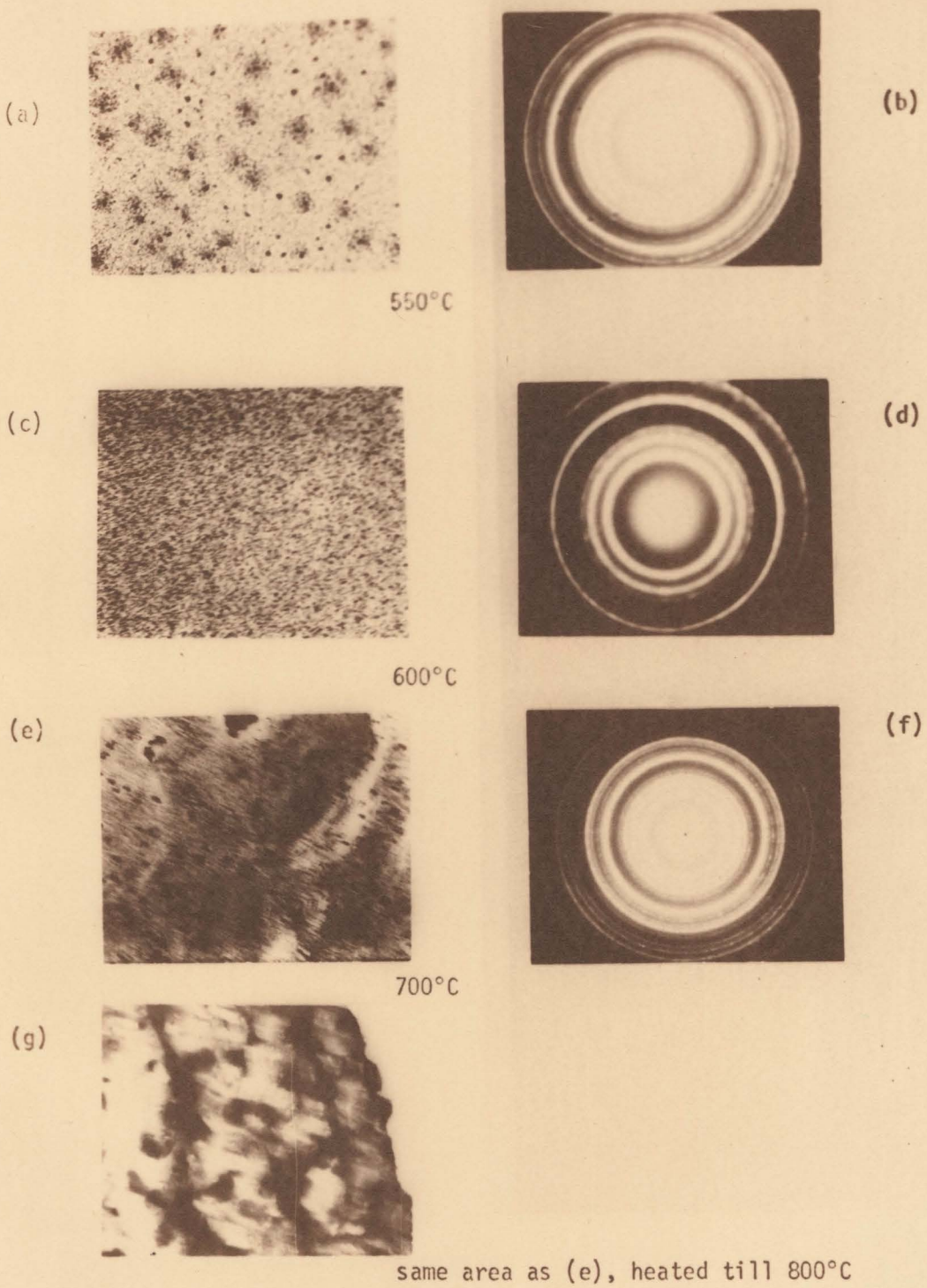

Figure 20. Transmission electron micrographs and diffraction patterns from SnO_2 films heated inside the microscope by heating stage. Magnification of micrographs x 11,000 - 80 KV.

(a)

(b)

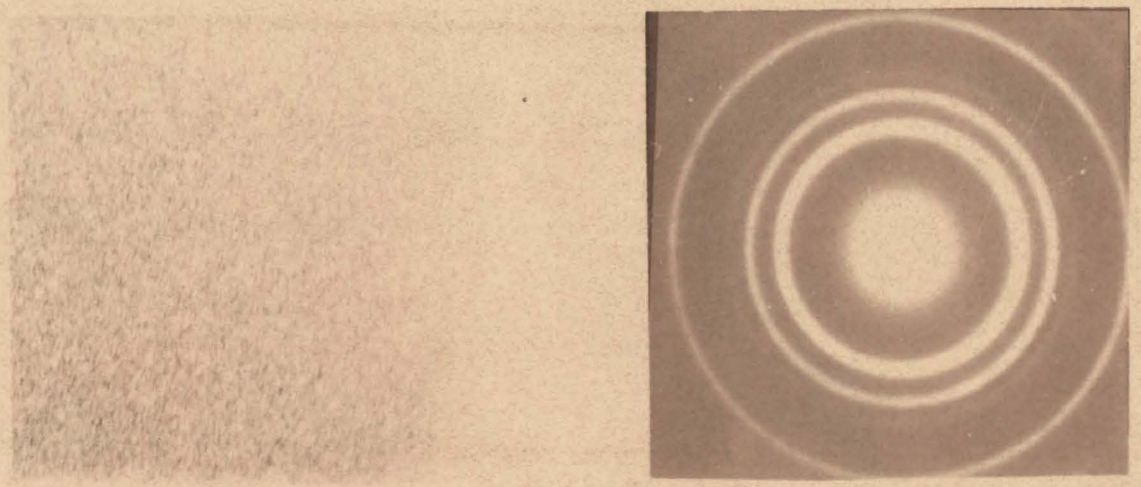

Figure 21. Electron micrograph and electron diffraction pattern of SnO_2 deposited on heated substrate; films were stripped and heated on a Mo-grid for 10 min. in air (600°C). Magn. 11,000 - 80 KV.

at 400°C, did not result in any structure change (Fig. 16(b)).

The implication is that the still unidentified deviant crystal structure occurs transiently during crystallization or heating, though only for particular heating sequences, specimens and/or heating atmospheres. Apparently this transient phase occurs at a temperature slightly greater than the crystallization temperature.

3.8 Tentative identification of the deviant crystal structure

3.8.1.

A structure slightly different from cassiterite and similar to that in Fig. 15(b) can be noticed also in Fig. 4, 6 and 7. Finally we noticed the same inner extra line as in Fig. 20(b) in the electron diffraction pattern of SnO_2 film deposited on KCl at high temperature, stripped, and bombarded with heavy ions at high dose where the crystallization is probably due to ion beam heating rather than ion impact.

3.8.2.

The fact that the new structure appears transiently upon increasing the temperature might mean that a structure related to cassiterite, but not exactly the same, appears when amorphous SnO_2 crystallizes. There is certainly good precedent for such intermediate phases; e.g. with Al_2O_3, TiO_2 and ZrO_2, the attainment of a stable crystalline form is preceded by respectively γ-Al_2O_3, anatase, and cubic-ZrO_2.

On the other hand, the fact that in all cases (Figs. 4, 6, 7, 15b, and 20b) the heating has been carried on in vacuum might mean that oxygen ions have escaped and a change from SnO_2 to SnO (or an intermediate oxide) takes place.

3.8.3.

Fig. 20'(b), 20'(d), and 20'(f) are a two-times magnification of Fig. 20(b), 20(d) and 20(f).

Table V shows a comparison between data obtained from Fig. 20'(d), 20'(f) and the ASTM data for SnO_2, revealing a cassiterite-structure in our film.

Table VI deals with Fig. 20'(b), where two extra lines (w.r.t. the cassiterite structure) appear. Considering the first and the seventh ring as extra rings belonging to some phase different from SnO_2, it is seen from Table VI that the rest of the rings can definitely be ascribed to a cassiterite structure. (N.B. As pointed out in section 3.2.5., we consider the fourth ring of Fig. 20'(b) as the superposition of two rings, R_4 and R_5). On the other hand we get a value of 0.4 for R_1/R_6 (Table VI') and a very similar one, 0.39, for d_6/d_1 where the values of d_6 and d_1 are taken from tabulated values of interplanar spacings in the SnO structure (ASTM-6-0395) Table VI' shows that other SnO lines are probably hidden by the SnO_2 lines.

The appearance of rings corresponding to a SnO structure can be attributed, as we already said, to a release of oxygen during heat treatment in vacuum at about 550°C. Unfortunately this hypothesis is contradicted by the appearance of an SnO_2 structure in other specimens heated in vacuum at 600°C and higher (Fig. 20'(d), 20'(f)), as shown in Table V, and further experiments will be needed to finally resolve the matter.

Fig. 15'(a), 15'(b) and 16'(b) are a two-times magnification of Fig. 15(a), 15(b) and 16(b).

Table VII shows that Fig. 15'(a) and 16'(b) are diffraction patterns typical of a cassiterite structure.

The cassiterite structure appearing in Fig. 15'(a) modifies, under heat treatment in vacuum, to a slightly different structure, as shown in

Fig. 15'(b).

As we already said, a structure similar to that in Fig. 15'(b) can be noticed also in Fig. 4', 6' and 7', that are two-times magnifications of Fig. 4, 6 and 7. It is evident that Fig. 15'(b), Fig. 4', Fig. 6' and Fig. 7' represent the same structure (unknown), even if in Fig. 15'(b) more lines are resolved. In Table VIII data from Fig. 4' are reported.

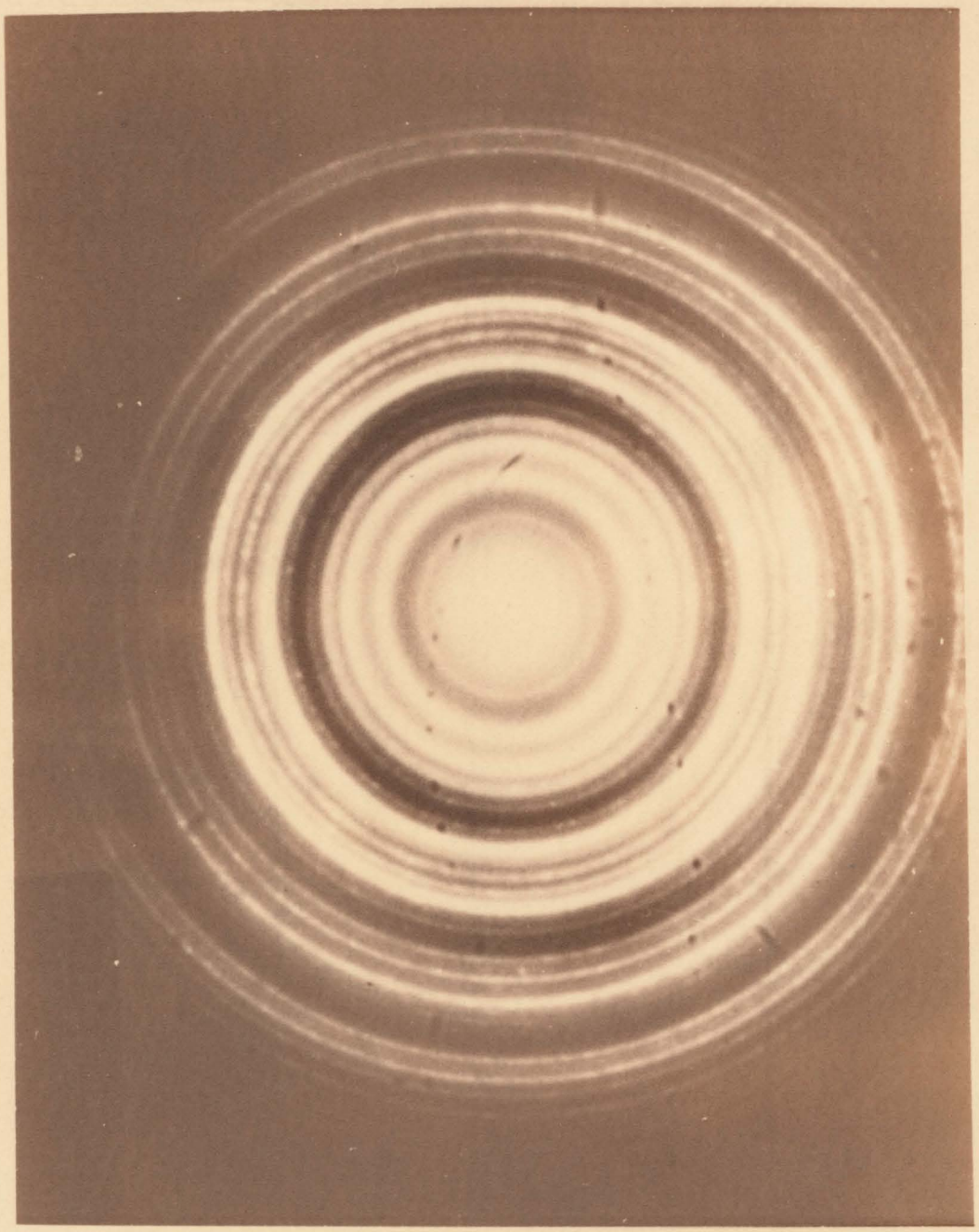

Figure 20'(b) Two-times magnification of Fig. 20(b). The first and the sixth ring appearing in figure are two extra rings w.r.t. the cassiterite structure (20'(d) and 20'(f)). In section 3.8.3. the sixth ring is referred to as the seventh, because we know that the fourth ring appearing in the picture is actually the superposition of 2 rings.

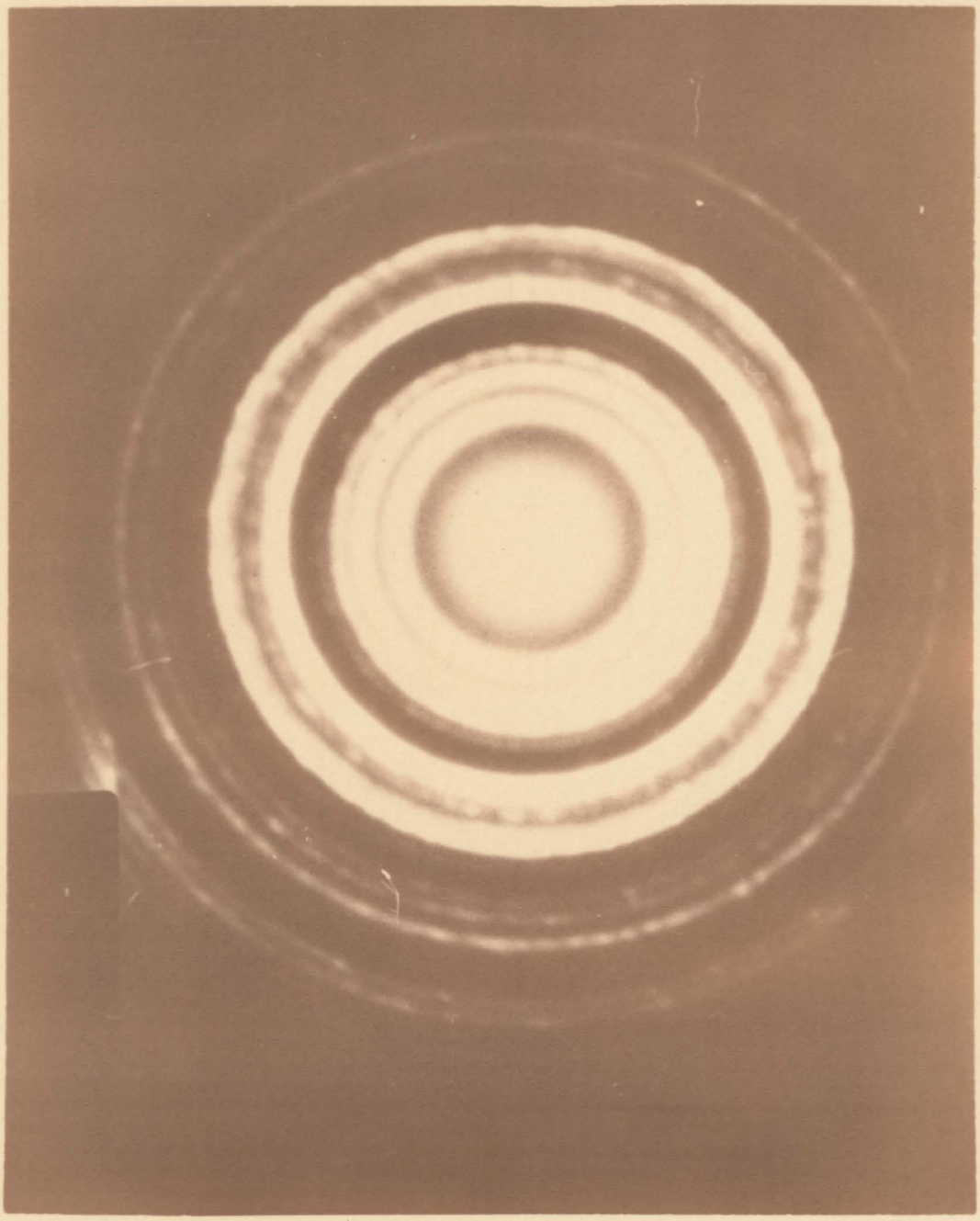

Figure 20'(d). Two-times magnification of Figure 20(d).

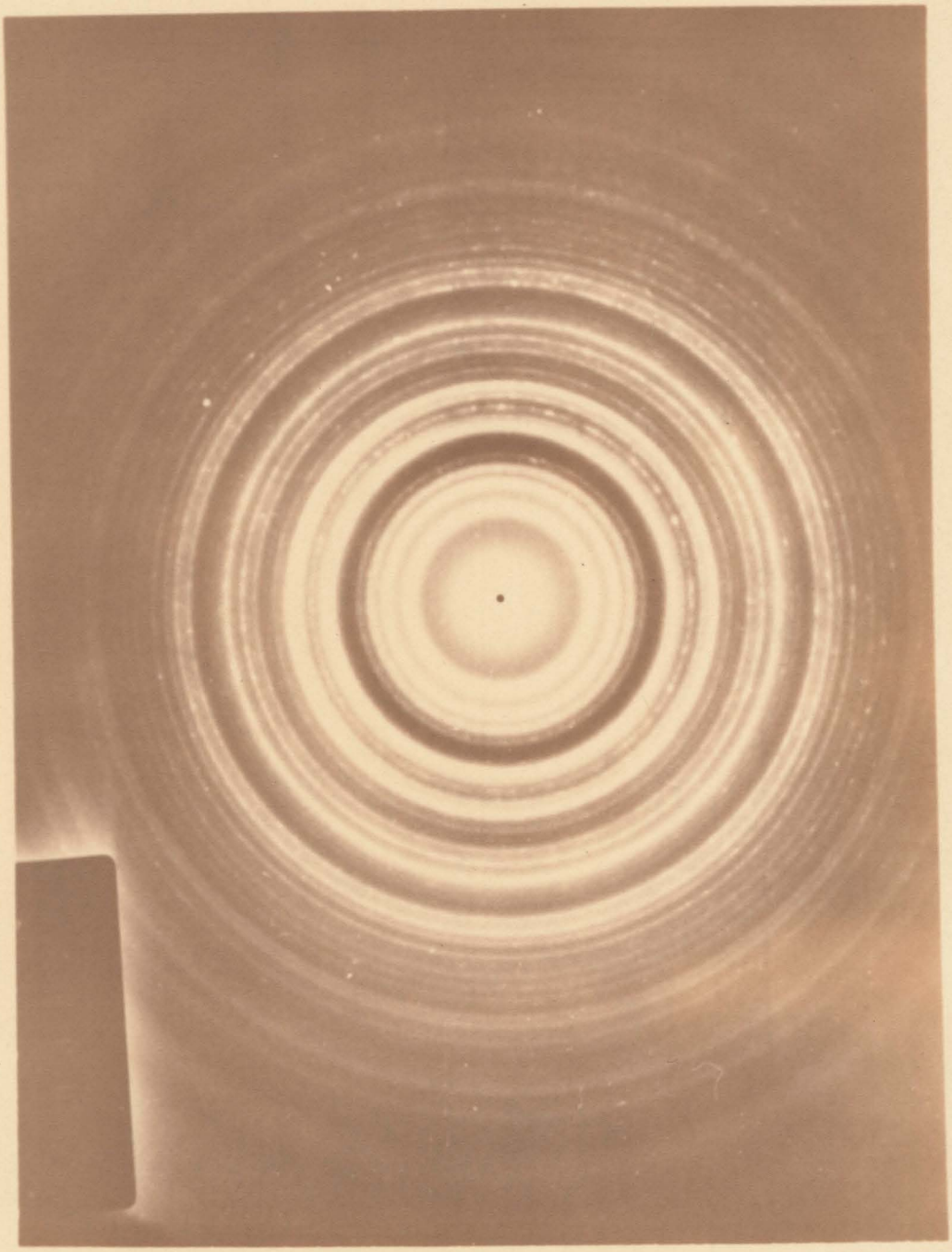

Figure 20'(f). Two-times magnification of Figure 20(f).

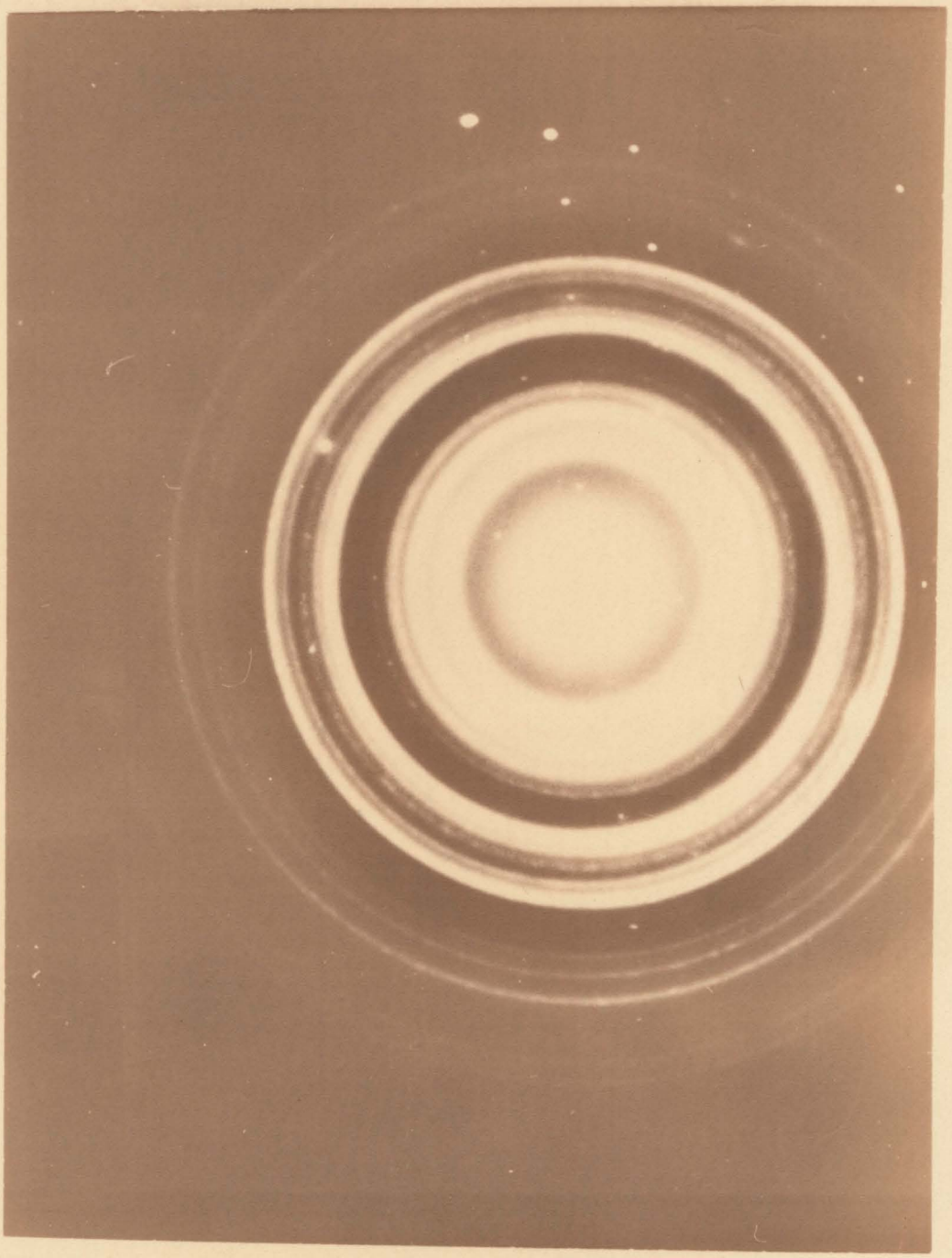

Figure 15'(a). Two-times magnification of Figure 15(a).

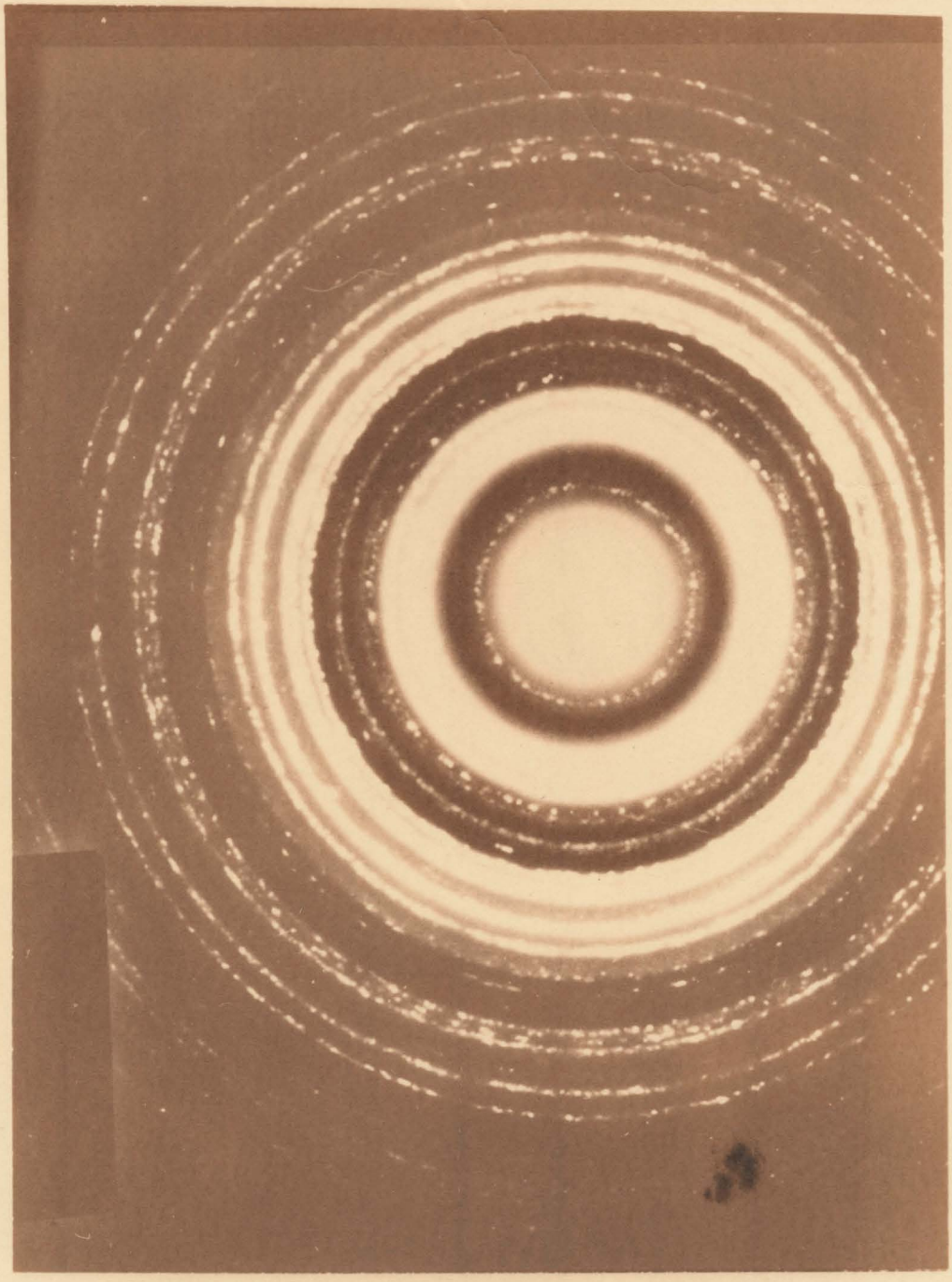

Figure 15'(b). Two-times magnification of Figure 15(b).

Figure 16'(b). Two-times magnification of Figure 16(b).

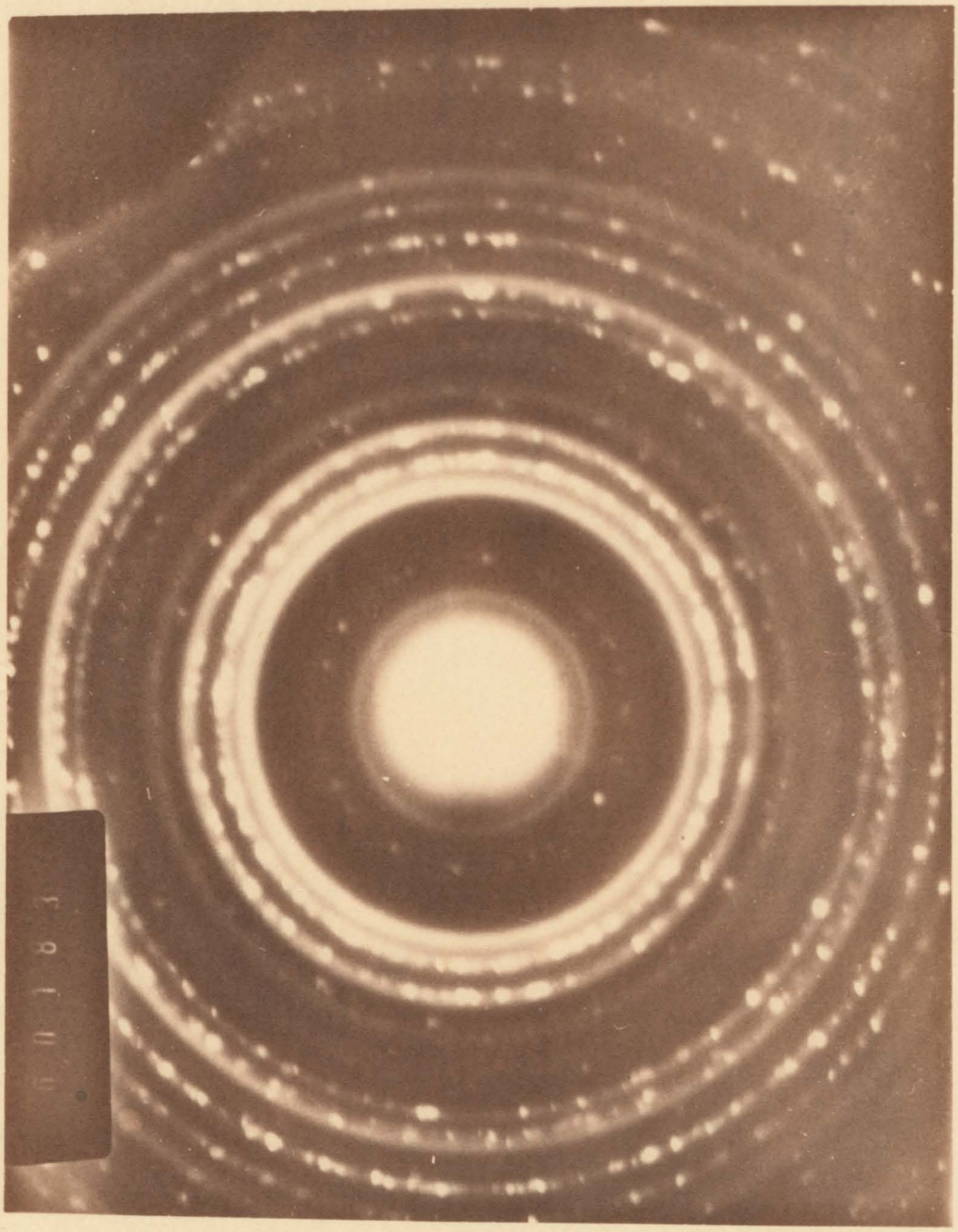

Figure 4'. Two-times magnification of Figure 4.

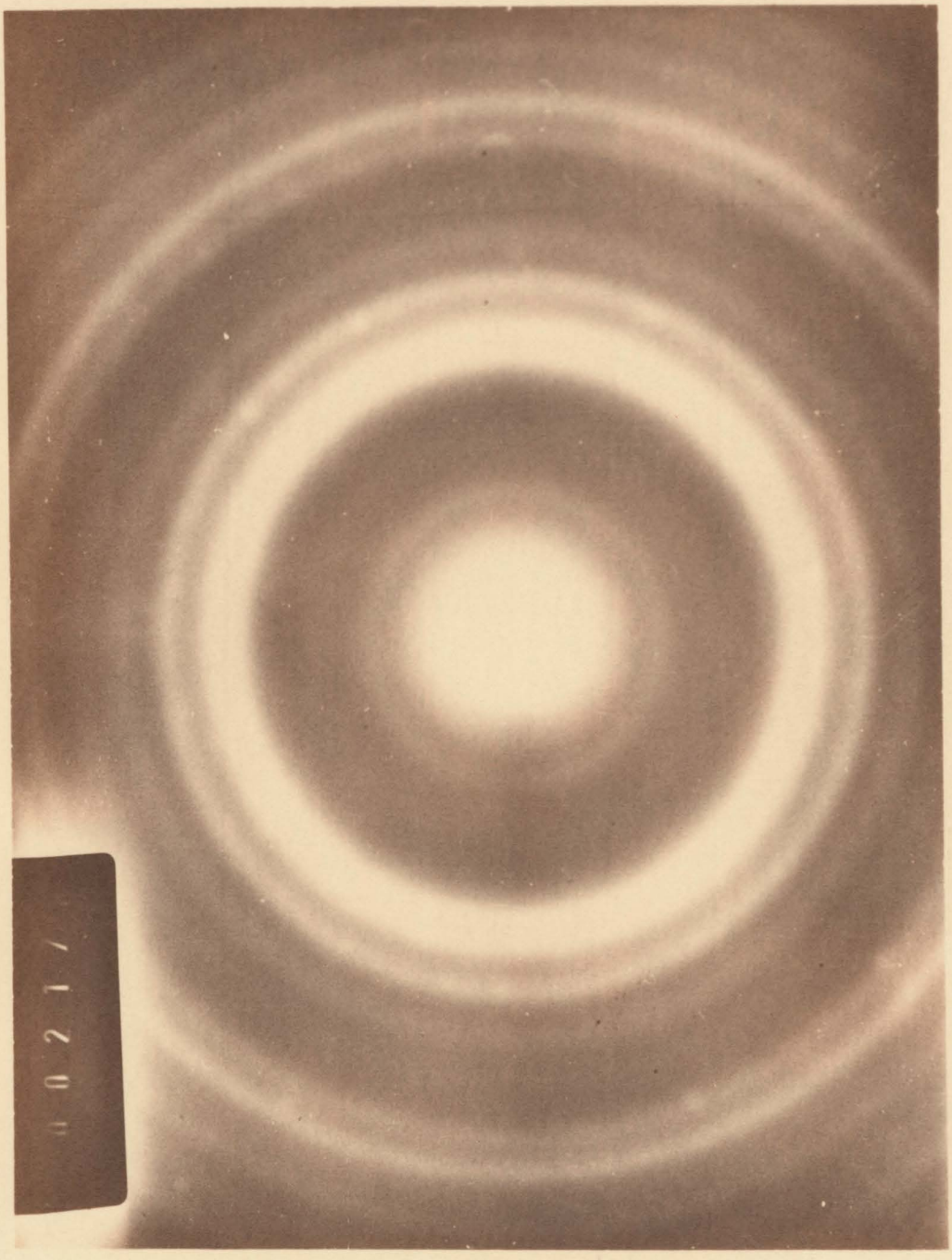

Figure 6'. Two-times magnification of Figure 6.

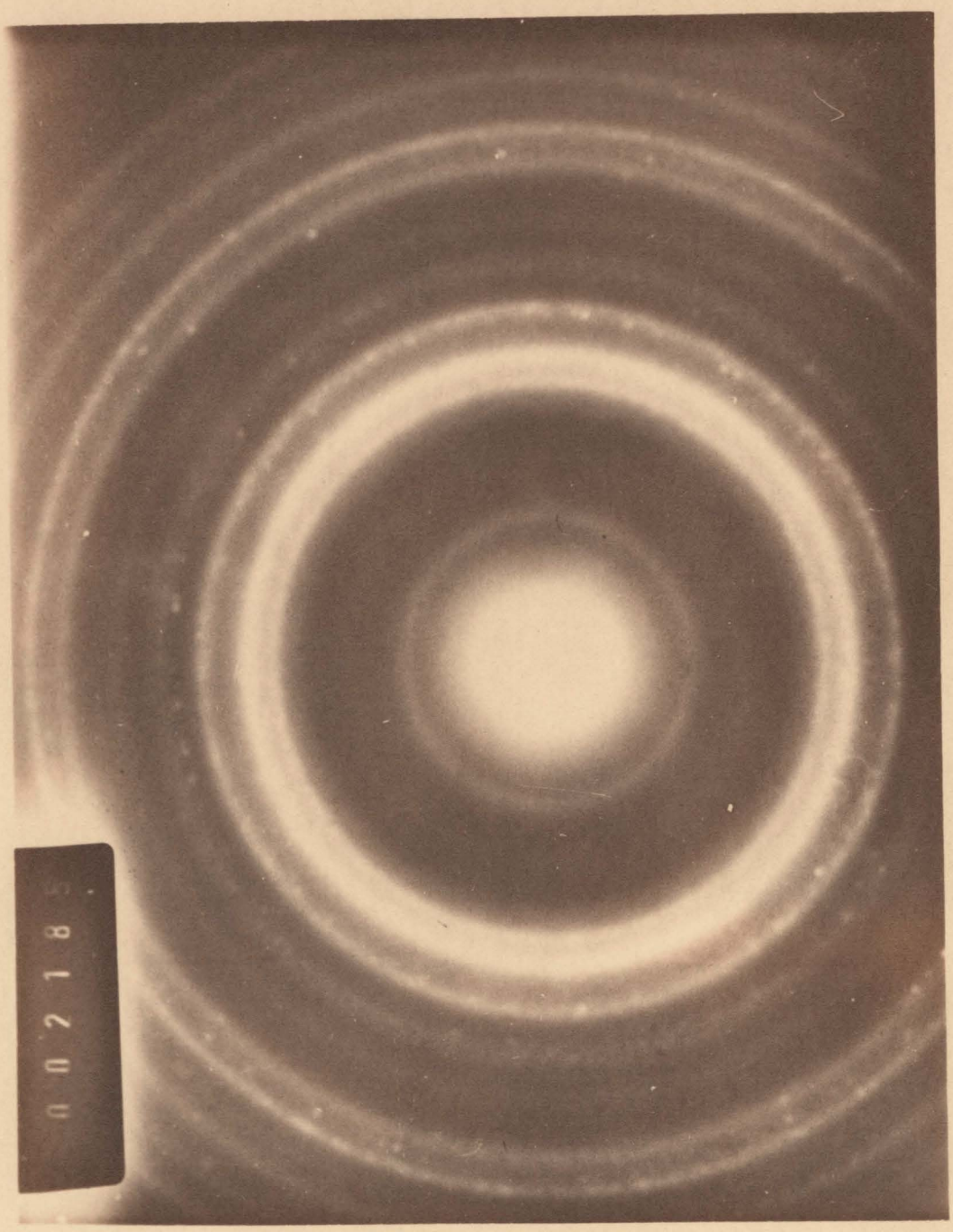

Figure 7'. Two-times magnification of Figure 7.

Table V

Diffraction Data for Tin Oxide

Data from Fig. 20'(d)	Data from Fig. 20'(f)	SnO_2 (Cassiterite) ASTM 5-0467
$R_1/R_2 = 0.8$	$R_1/R_2 = 0.79$	$d_2/d_1 = 0.787$
$R_3/R_2 =$ } 1.14	$R_3/R_2 =$ } 1.13	$d_2/d_3 = 1.114$
$R_4/R_2 =$	$R_4/R_2 =$	$d_2/d_4 = 1.142$
$R_5/R_2 = 1.254$	$R_5/R_2 = 1.25$	$d_2/d_5 = 1.245$
$R_6/R_2 = 1.51$	$R_6/R_2 = 1.495$	$d_2/d_6 = 1.495$
$R_7/R_2 = 1.58$	$R_7/R_2 = 1.55$	$d_2/d_7 = 1.578$
$R_8/R_2 = 1.67$	$R_8/R_2 = 1.66$	$d_2/d_8 = 1.66$
$R_9/R_2 = 1.77$	$R_9/R_2 = 1.79$	$d_2/d_9 = 1.765$

Table VI

Diffraction Data for Tin Oxide

SnO_2 (Cassiterite) ASTM 5-0467	Data from Fig. 20'(b)
$d_2/d_1 = 0.787$	$R_2/R_3 = 0.8$
$d_2/d_3 = 1.114$	$R_4/R_3 =$ } 1.13
$d_2/d_4 = 1.142$	$R_5/R_3 =$
$d_2/d_5 = 1.245$	$R_6/R_3 = 1.25$
$d_2/d_6 = 1.495$	$R_8/R_3 = 1.51$
$d_2/d_7 = 1.578$	$R_9/R_3 = 1.58$
$d_2/d_8 = 1.66$	$R_{10}/R_3 = 1.67$
$d_2/d_3 = 1.765$	$R_{11}/R_3 = 1.766$

Table VI'

Diffraction Data for Tin Oxide

SnO ASTM 6-0395	Data from Fig. 20'(b)
$d_2/d_1 = 0.616$	$R_1/R_2 = 0.694$
$d_3/d_1 = 0.555$	$R_1/R_3 = 0.554$
$d_4/d_1 = 0.499$	$R_1/R_4 = 0.490$
$d_5/d_1 = 0.42$	$R_1/R_5 = 0.443$
$d_6/d_1 = 0.392$	$R_1/R_6 = 0.40$
$d_7/d_1 = 0.371$	$R_1/R_7 = 0.368$
$d_8/d_1 = 0.331$	$R_1/R_8 = 0.35$
$d_9/d_1 = 0.308$	$R_1/R_9 = 0.332$

Table VII

Diffraction Data for Tin Oxide

Data from Fig. 15'(a)	Data from Fig. 16'(b)	SnO_2 (Cassiterite) ASTM 5-0467
$R_1/R_2 = 0.8$	$R_1/R_2 = 0.78$	$d_2/d_1 = 0.787$
$R_3/R_2 =$ } 1.12	$R_3/R_2 =$ } 1.13	$d_2/d_3 = 1.114$
$R_4/R_2 =$	$R_4/R_2 =$	$d_2/d_4 = 1.142$
$R_5/R_2 = 1.23$	$R_5/R_2 = 1.243$	$d_2/d_5 = 1.245$
$R_6/R_2 = 1.48$	$R_6/R_2 = 1.487$	$d_2/d_6 = 1.495$
$R_7/R_2 = 1.565$	$R_7/R_2 = 1.57$	$d_2/d_7 = 1.578$
$R_8/R_2 = 1.635$	$R_8/R_2 = 1.66$	$d_2/d_8 = 1.66$
$R_9/R_2 = 1.74$	$R_9/R_2 = 1.755$	$d_2/d_9 = 1.765$

Table VIII

Diffraction Data for Tin Oxide

Data from Fig. 4'	SnO_2 (Cassiterite) ASTM 5-0467	SnO ASTM 6-0395
$R_1/R_2 = 0.775$	$d_2/d_1 = 0.79$	$d_2/d_1 = 0.616$
$R_1/R_3 = 0.506$	$d_3/d_1 = 0.707$	$d_3/d_1 = 0.555$
$R_1/R_4 = 0.46$	$d_4/d_1 = 0.69$	$d_4/d_1 = 0.499$
$R_1/R_5 = 0.405$	$d_5/d_1 = 0.633$	$d_5/d_1 = 0.42$
$R_1/R_6 = 0.363$	$d_6/d_1 = 0.527$	$d_6/d_1 = 0.392$
$R_1/R_7 = 0.314$	$d_7/d_1 = 0.50$	$d_7/d_1 = 0.371$
$R_1/R_8 = 0.29$	$d_8/d_1 = 0.475$	$d_8/d_1 = 0.331$
$R_1/R_9 = 0.275$	$d_9/d_1 = 0.447$	$d_9/d_1 = 0.308$

3.9 Films Deposited on SnO_2 Single Crystal

The sputtering conditions were the same as before. Films were examined by reflection electron diffraction with the microscope operating at 80 KV. Diffraction patterns have been recorded of the single crystal support (Fig. 22(a)), of the film as sputtered (Fig. 22(b)) and after heat treatment in air for hold times of 6 min. at 185, 200, 225, 325°C (Fig. 23(a) (b) (c) and (d)). The crystallization temperature was found in this way to be about 225°C and we note that this is similar to what was observed in section 3.5 for films which, like those here, were supported during heating.

3.10 Film Deposited on Sintered SnO_2 Pellets

3.10.1.

Films were examined by reflection electron diffraction, with the microscope operated at 80 KV. Sputtering conditions were the same as usual.

Reflection electron diffraction patterns of pressed and sintered SnO_2 substrates (Fig. 24(a)) and of SnO_2 films as deposited (Fig. 24(b)) have been recorded. The films appear crystalline as deposited (Fig. 24(b)), like those in section 3.6.

3.10.2.

Upon first considering this result, we thought that the films were not thick enough, so that we were actually looking at the substrates rather than at the films, as shown in the sketch below.

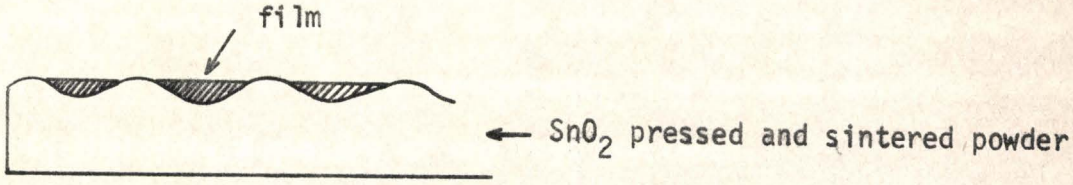

Therefore we increased the sputtering time of half an hour and we used both SnO_2 and KCl supports at the same time, to be able to check on KCl supports (by wet-stripping) that we really obtained an SnO_2 layer. Nevertheless results were the same and therefore we have to infer that films deposited on SnO_2 pellets are crystalline at the deposition temperature.

3.11 Films Obtained from Anodic Oxidized Tin

3.11.1.

The electrolyte tank was a glass vessel, the cathode was a polished aluminum sheet, while the anode was a tin sheet polished by a solution of one part of H_2SO_4 and four parts of water. First we tried to anodize by a solution of Ethylen Glycol (90 c.c.) and Ammonium Pentaborate (10 gr.) but it did not work out as evidenced by a lack of interference colors and a steady high current. Increasing the Ammonium Pentaborate amount to 30 gr. we have been able to obtain non-porous oxide film exhibiting well-defined interference colors.

3.11.2.

Anodic oxide films can be prepared under one of three different conditions. The first method consists of growing under constant-voltage conditions until the current is conveniently small. In the second, the one we used, a constant current is passed through the cell and the film thickness is proportional to the time for which the current is passed. The third method involves a constant current period followed by constant voltage. During formation at constant current, each new layer of oxide of thickness dD requires an extra potential dV to be added across the film to maintain the field in the oxide and hence the current. The voltage developed across the film is therefore a measure of the film thickness.

3.11.3.

There is, however, a limit to the thickness that can be obtained.

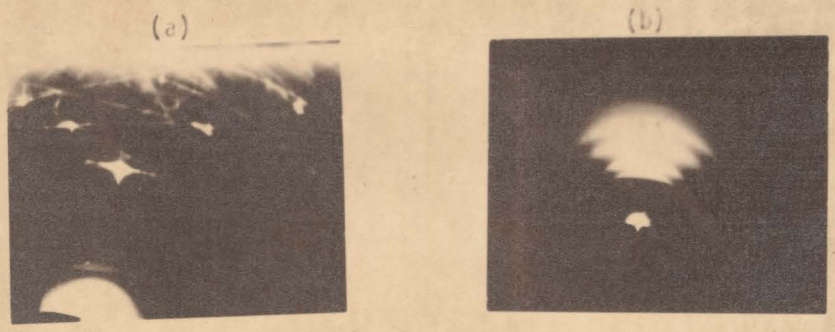

Figure 22. Reflection electron diffraction patterns of (a) SnO_2 single crystal and (b) SnO_2 film deposited on SnO_2 single crystal.

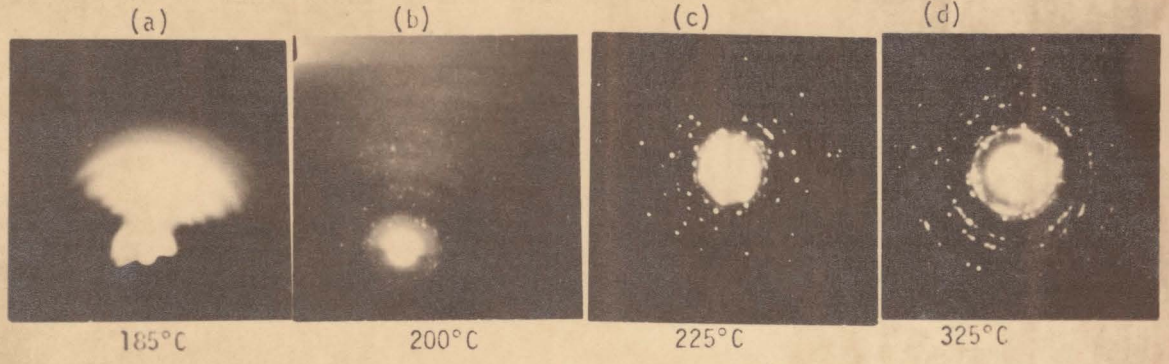

Figure 23. Effect of heat treatment in air of SnO_2 film deposited on SnO_2 single crystal.

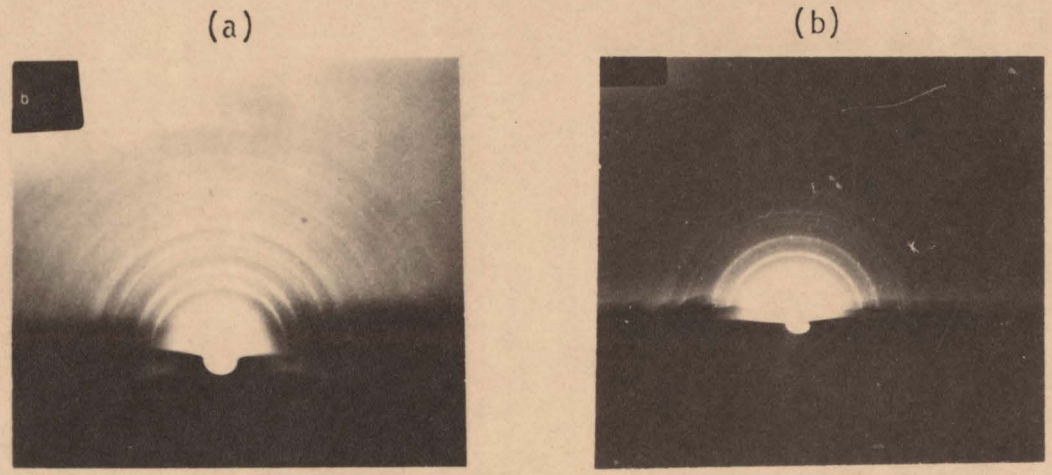

Figure 24. Reflection electron diffraction of

(a) SnO_2 pressed and sinterized powder

(b) SnO_2 film deposited on SnO_2 pressed and sinterized powder.

Either the film will break by arcing, or field recrystallization will occur. In the first case the maximum voltage and hence thickness attainable is a function of the purity of substrate, composition of electrolyte, and various other features. Field recrystallization, too, occurs because of the applied voltage; all anodic oxides show this to some extent; the recrystallized areas will often be electrical shorts through the film due, for example, to the possibility of grain boundary conductivity.

We have reached a maximum tension of 55 volts. The film obtained in this way was stripped by a solution of iodine in methanol at 50°C (as kindly suggested by Mr. N. Khoi), and directly picked up on electron microscope grids.

3.11.4.

The film was white, hence stoichiometric (see sections 3.7.2. and 3.7.3.). Films were thick compared to the thicknesses suitable for transmission electron microscopy. Nevertheless, we examined them by looking at a film edge (Fig. 25(a)). Fig. 25(b) is the corresponding electron diffraction pattern, showing a polycrystalline structure. Films all showed this structure, even if at different degrees of crystallization (Fig. 26(a), (b) and (c)).

The film structure was worked out from Fig. 26(c), and it was found to be cassiterite, as shown in Table IX. Fig. 27 shows a reflection electron diffraction pattern of anodic oxided tin (55 volt).

Table IX

Diffraction Data for Tin Oxide

Tin Oxide Film (Fig. 26(c))	SnO_2 (Cassiterite) ASTM 5-0467
$R_1/R_2 = 0.78$	$d_2/d_1 = 0.787$
R_3/R_2 } = 1.11 R_4/R_2	$d_2/d_3 = 1.114$ $d_2/d_4 = 1.142$
$R_5/R_2 = 1.247$	$d_2/d_5 = 1.245$
$R_6/R_2 = 1.495$	$d_2/d_6 = 1.495$
$R_7/R_2 = 1.562$	$d_2/d_7 = 1.578$
$R_8/R_2 = 1.644$	$d_2/d_8 = 1.66$
$R_9/R_2 =$	$d_2/d_9 = 1.765$

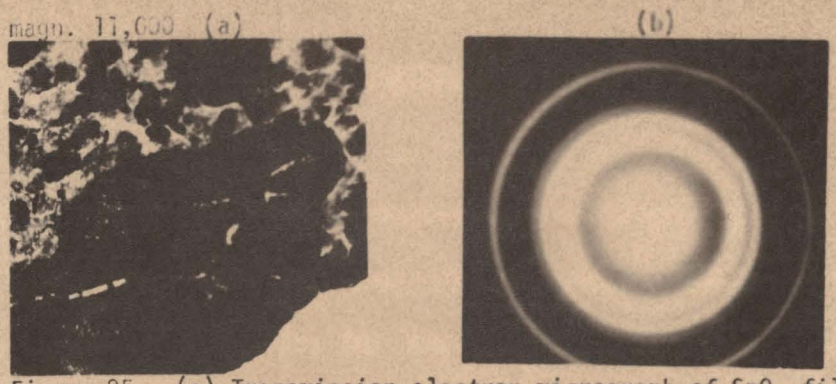

Figure 25. (a) Transmission electron micrograph of SnO_2 film stripped from anodic-oxidized tin. (b) Corresponding electron diffraction pattern (a) magn. 11,000.

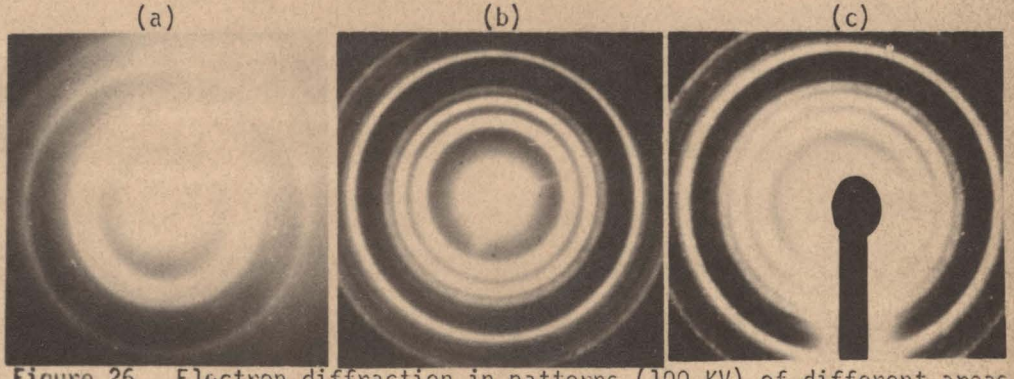

Figure 26. Electron diffraction in patterns (100 KV) of different areas, showing different degree of crystallization in the SnO_2 films. Films were stripped from anodic-oxidized tin.

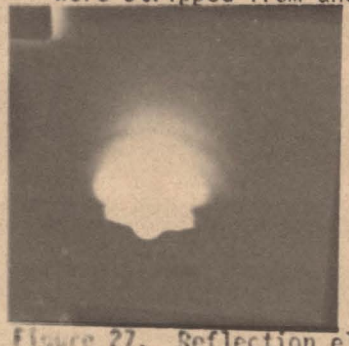

Figure 27. Reflection electron diffraction (80 KV) of anodic-oxidized tin.

Chapter 4

Summary

4.1

As we said in the Introduction, sprayed or anodized (in a solvent electrolyte) layers of SnO_2 show, as prepared, a crystalline structure. We have confirmed this also for the case of SnO_2 films, prepared (apparently for the first time) by anodic oxidation of metallic tin in a non-solvent electrolyte.

4.2

For vacuum evaporated films, other researchers have found an amorphous structure of the material as deposited, while no data on crystallization temperature have been reported.

4.3

For the case of ion-beam sputtered SnO_2, films have been reported to present a polycrystalline structure as deposited (Yamanaka and Oohashi (1969)). Using this technique we have been able to obtain both polycrystalline as well as amorphous SnO_2 films, the latter showing crystalline structure at 350°C (vacuum heated).

4.4

Our major investigation has been centered about reactively sputtered films. Table X shows crystallization temperatures for reactively sputtered amorphous tin oxide films as reported in the literature, together with values obtained from our work.

Also reported are: (i) deposition temperature, (ii) substrate nature and (iii) type of heat treatment. We note the correlation between supported films and a low crystallization temperature.

4.5

We obtained a quite surprising result in the case of films deposited on SnO_2 pellets. They turned out to be crystalline as deposited.

4.6

The crystalline product structure, mentioned in the literature as a not better specified than a "rutile like" structure, has been worked out to be cassiterite, under most of the different ways of deposition explored. After the example of GeO_2, Bi_2O_3, ZrO_2, whose amorphous states crystallized in the structure they present at high temperature, we were looking for a new phase (different from cassiterite), appearing from the crystallization process of our amorphous films. Their structure, instead, has been confirmed to be cassiterite, the implication being that SnO_2 has only one crystal form up to the melting point (note that the phase relations of SnO_2 are unknown above about 1700°C due to the onset of vaporization). On the other hand, in various occasions, we passed thru a different phase, as pointed out in the report. A new series of experiments, as suggested in the next section, will probably enable us to fully establish the nature of this new phase though it seems at present to be simply SnO formed by loss of oxygen.

4.7

The structure of the as deposited amorphous film, as revealed by transmission electron microscopy, presented interesting features: continuous structure in the case of high temperature deposition, "island structure" in the case of low temperature deposition. Besides, in the latter case, heat treatment showed the film to maintain the "island structure" in the case of unsupported films, while the structure resulted continuous when the heat treatment was performed on supported specimens.

Table X

Crystallization temperatures (°C) for amorphous Tin Oxide films deposited by reactive sputtering. Note how a low crystallization temperature correlates with the films being supported during heating.

Films deposited on unheated silica substrates (Sinclair and Peters, 1963).	400
Films deposited on refrigerated (liquid nitrogen) substrates (ground and polished Corning Code 7900 glass). Thermal treatment in air of supported films. (Lieberman and Medrud, 1969).	250 (1 hour)
Films deposited on cooled (KCl) substrates and unsupported during heat treatment in air (present work). Island structure.	550 (6 min)
Films deposited on cooled (KCl) substrates and supported during heat treatment in air (present work).	300 (6 min)
Films deposited on heated substrates (KCl) and unsupported during heat treatement in vacuum (present work). Continuous	500
Films deposited on heated substrates (SnO_2 single crystal) and supported during heat treatment in air (present work). Continuous	225 (6 min)

4.8

Finally, to be confirmed by future investigations, but already clearly indicated by the results obtained in the case of deposition on water cooled substrates, is the dependence of SnO_2 film structure on film thickness.

Chapter 5

Future Experiments

5.1

We plan to expand the tools of our research to have our SnO_2 films investigated by a three probe analysis: electron microscopy, resistivity measurements and gas-release measurements.

We want to go again thru the properties we have been checking so far by electron microscopy, and relate them to electrical properties (resistivity measurements). The measured electrical properties of SnO_2 films will be correlated to the structural parameters as obtained by transmission electron microscopy (to our knowledge nothing or very little has been done so far in this sense, though limited information is available about relations between electrical and optical properties).

A third source of information will be the data obtained on diffusivity in SnO_2 by gas release: i.e. inert-gas mobility will be used as a means of estimating intrinsic self-diffusional mobility. The validity of this approach has been demonstrated by Kelly and Jech, as shown in Table XI.

5.2

Second, we plan to expand the objectives of our research.
(a) Taking advantage of the reactive sputtering apparatus we have built, we can sputter Sn in argon/oxygen atmospheres which contain 0 to 100% of oxygen. The effect of addition of oxygen to the atmosphere when Sn is sputtered may be studied with respect to various (resistivity, structure, composition) properties of the films: a range of composition, and hence of physical characteristics, from pure metal to completely stoichiometric

Table XI

Comparison of temperatures for stage-IIA gas-release and for volume self-diffusion

Energy, ion, target and reference	T_{50} for stage IIA in °C (observed)	T_{50} for volume self-diffusion in °C [calculated from eq. (5b)]	T_{IIA}/T_{s-d} in °K/°K	R_m[a]
40-keV Xe-Ag [1]	410	425	0.98	95
40-keV Xe-Al_2O_3 [1]	1145	1295 (Al)	0.90	75
40-keV Xe-Au (fig. 1)	(< 490[b])	405	....	70
30-keV Xe-Cu [6]	375	495	0.84	75
Tesla Kr-Fe_2O_3 (fig. 2)	775[c]	885 (Fe)	0.90	5
		805 (O)	0.97	
10-keV Kr-Fe_2O_3 [21]	855	980 (Fe)	0.90	30
		920 (O)	0.94	
40-keV Xe-KBr [10]	280	430 (K)	0.79	
		460 (Br)	0.76	340
2-keV Kr-KCl (fig. 5)	210	335 (K)	0.80	12
		365 (Cl)	0.76	
40-keV Xe-KCl [32]	340	440 (K)	0.86	340
		470 (Cl)	0.83	
85-keV Rn-NaCl [48]	310	415 (Na)	0.85	720
		490 (Cl)	0.76	
9-keV Kr-Pt [28]	570	775	0.80	35
10-keV Kr-Si (fig. 3)	955[e]	1120	0.88	30
40-keV Xe-Ta [1]	1190	1320	0.92	70
40-keV Xe-ThO_2 [43]	1220	(1400)[d] (Th)	0.89	50
40-keV Xe-UO_2 [43]	1220	1400 (U)	0.89	50
1-keV Ne-W [4]	1625[e]	1980	0.84	10

[a] This is the value of R_m, in units of mean atomic spacings, used in calculating T_{50} for volume self-diffusion.

[b] Probably an upper limit, since the dose was high enough to have led to both stages IIA and IIB.

[c] Average value based both on the data presented here and on duplicate runs.

[d] Assumed to be the same as for U-UO_2.

[e] Applicable to the gas-release component lying in the region 1000–2100 °C as distinct from that at lower temperatures attributed to stage I-A.

oxide can be produced. In particular, using low enough values of the oxygen partial pressure, we might be able to deposit films presenting an island structure of the following kind: metallic islands surrounded by an insulating inter-island regions of amorphous SnO_2. This structure has been recently observed by Hardy et al. (private communication) in the case of reactive sputtering of Ta, and is also similar to that usually associated with cermet (ceramic + metal) films (Glang and others, 1967). It leads to electrical conductivity by tunneling instead of by normal electron mobility.

(b) The film colour variation can be recorded spectrophotometrically, with respect to its stoichiometry, and for films having the same degree of stoichiometry, we expect differences in the crystallization process (and resistivity) to occur when crystallization is carried on in vacuum and in air. We might also have sharp differences in structure (and resistivity), in films with different degrees of stoichiometry, as suggested by the example of ZrO_2, which exists, depending on temperature, in cubic, tetragonal and monoclinic form, and where the transformation temperatures depend on stoichiometry (El-Shanshoury et al., 1970). A systematic investigation of this kind, together with the one outlined in (a), may also give us an explanation about the origin of the different phases (with respect to cassiterite structure) we have been observing.

(c) A parameter whose effect might be quite interesting to take account of is the film thickness, as already suggested in our report. We expect that films may change spontaneously from an amorphous to a crystalline state with increasing their thickness. If it is so, we may investigate this effect with respect to substrate temperature, scanning from liquid nitrogen cooled, acetone-and-dry-ice cooled, running-water-cooled substrates, up to heated substrates.

(d) A complete spectrum of interference colours for anodic oxidized tin, at increasing values of applied voltage can be determined. We expect, in view of the relation of film thickness to structure with SnO_2, that anodic SnO_2 which is formed at the minimum possible voltage (e.g. 5 volt) may have a different structure from the one we determined using an applied voltage of 55 volt. If so this would be the first known instance where such an effect has occurred anodically (excluding of course, instances of field-induced crystallization). (e) Finally we propose to undertake investigations aimed to gain a better insight into the mechanism of tin reactive sputtering, e.g. where the site of oxidation is. Thus it is known from other work that the oxidation of sputtered material in fact happens at the substrate till a certain value of the oxygen partial pressure; beyond this value what actually happens is sputtering of an already oxidized target. We would hope to find the value of the critical oxygen pressure for the process, possibly by measuring the deposition rate.

Part Two

RADIATION DAMAGE STUDIES

CHAPTER 6

Radiation Damage in SnO_2 Films

6.1.

The impact of heavy ions on solids is known to lead in some cases to amorphization, in some cases to phase changes, whereas, in other cases the bombarded solid shows little or no change in its structure. The first indication of a radiation-induced phase change from the crystalline to the amorphous state was observed in natural minerals containing alpha-emitting radioactivity (e.g. Fassler, 1942). The damage regions could be transformed to the crystalline state again by annealing.

A large number of neutron-irradiation-induced phase changes from one crystalline form to another have been observed. A survey by Hauser and Schenk (1963) reviewed the phase changes in metals and in some ceramics, e.g. SiO_2, ZrO_2 and $BaTiO_3$. The same authors (1964) showed that the low temperature phase of TiO_2, crystalline brookite, is transformed to the amorphous state after a reactor irradiation of 2.8×10^{19} fast neutrons/cm^2.

Direct evidence of structural changes following ion bombardment was obtained for metals by several authors: e.g. Trillat (1956) reported that thin films of single-crystal gold became polycrystalline following bombardment with oxygen to very high doses; Gianolo (1957), using electron diffraction data, showed that surface layers of silicon are converted to a quasi-stable amorphous phase after bombardment with helium (6.6 $\mu Amin/cm^2$; 30 keV). Similar studies on silver (Ogilvie, 1959) showed that the surface contained misoriented crystallites $\sim$ 100Å in diameter following bombardment. Anderson et al. (1963), Izui and Suzuki (1963) and Parsons (1965) converted crystalline germanium to the amorphous form by ion bombardment. Pöhlan et al. (1964) noted destruction of the lattice structure of

GaAs after a dose of $3x10^{17}$ krypton ions/cm^2; Gonser and Okkerse (1958) noted a phase change in GaSb during bombardment with 12-MeV neutrons. Teodorescu (1966) bombarded with H^+ and N^+ (also O^+ and ionized air) pure Cu, Ag and Pd and impure Al, Mo, Ta and W, to study the surface corrosion due to the ionic beam; he noted the dependence of the corrosion on the energy of the incident beam.

Similar damage effects have been observed in non-metallic substances. Prince and Walker (1962) observed a formation of disordered regions along fission tracks in natural mica. Stech (1952) studied radiation damage following an alpha-particle bombardment to a dose estimated to be $10^{13\pm1}$ α particles/cm^2. A change from a crystalline to a quasi-amorphous state (metamictization) was found in substances with weak binding and/or low density of atomic packing in the unit cell. Damaged substances included potassium permanganate, arsenic trioxide, sodium oxalate, authracene, urea and tartaric acid.

Matzke and Whitton (1965) and Matzke (1968) bombarded with 40 keV xenon and krypton ions (to give integrated ion doses of up to $2x10^{16}$ ions/cm^2) single-crystal specimens or polycrystalline sinters of cubic NaCl, KCl, KBr, KI, MgO, CaO, NiO, UC, CaF_2, BaF_2, UO_2 and ThO_2 as well as anisotropic TiO_2, Al_2O_3, Cr_2O_3, Fe_2O_3, and U_3O_8. The specimens were examined by reflection electron diffraction for radiation damage in the form of a phase change from the crystalline to a quasi-amorphous state (metamictization). Damage of this kind was observed in all anisotropic crystals; observable lattice disorder without phase change was obtained for MgO. None of the other cubic materials showed any appreciable change in their diffraction pattern, even at the highest dose. The authors point out that the fact of a phase transformation from crystalline to a quasi-amorphous state occurring in all the anisotropic materials examined (U_3O_8,

Al_2O_3, Cr_2O_3, Fe_2O_3, TiO_2) supports the hypothesis of Berman et al. (1960) that anisotropic internal stresses resulting from expansion around the path of the bombarding ion contribute to the instability of the lattice.

Kelly and Naguib (1970) presented evidence for a new type of structural evolution following ion impact, such that bombardment of amorphous ZrO_2 leads to complete crystallization. The only previous indications of such an effect were with Ge, where Parsons and Balluffi (1964) observed very small extents of crystallization, and with SiO_2, where Weissmann and Nakajima (1963) found about 20% α-SiO_2 as the final product after prolonged exposure of vitreous SiO_2 to neutrons.

6.2.

Looking at these aspects of radiation damage, we submitted our reactively sputtered SnO_2 films to krypton ion bombardment.

Specimens were supported on 200-mesh copper grids set in small pockets on the target holder, and were bombarded with krypton ions at room temperature, using the same accelerator we used for ion-beam sputtering of SnO_2 pellets. Microscopic examinations were made after each bombardment.

6.3.

Fig. 28 shows transmission and diffraction micrographs of reactively deposited SnO_2 films, as described in Section 3.7. Bombarding these films with 35 KV ions and with the following doses:

6 μAx30 sec/cm^2

10μAx30 sec/cm^2

4 μAx1 min 15 sec/cm^2

6 μAx1 min/cm^2

6 μAx2 min/cm^2

the film structure was found to remain practically unchanged, i.e. amor-

phous, as shown in Fig. 29, Fig. 30, Fig. 31, Fig. 32 and Fig. 36 respectively. The top current we used was 10 μA.

Figure 37 shows that bombarding for 6 min. at 30 keV with a current fluctuating between 9 and 19 μA(dose $\simeq$ 70 μA min/cm^2, since current was $\sim$ 12μA most of the time), the amorphousness of the film remained unchanged. Fig. 38 shows that bombarding (with a 35 keV beam) an amorphous SnO_2 film for 30 min. with a current lower than 10 μA, film remains amorphous. Fig. 39 shows that when current reaches the value of 16 μA, film crystallizes.

6.4.

It seems therefore that, as far as structural change is concerned, what is crucial is not the dose but the current intensity; even at quite high dose, provided the current is below a certain value ($\sim$ 12 μA) there is no structure change, as shown in Fig. 38. On the other hand the structure change at current of 16 μA and higher is due, rather than to ion impact, to ion beam heating, i.e. it is a simple thermal crystallization.

6.5.

In a second set of experiments we bombarded samples already crystallized (thermally, either in air or in vacuum).

Fig. 40 shows transmission and diffraction micrographs of the starting material, i.e. SnO_2 film crystallized by 10 min of heat treatment in air at about 600°C (film supported on a Mo-grid during heat treatment). After bombarding with a current < 10 μA for 30 min and subsequently another sample for 60 min, no majorchange in structure was noticed, as shown in Fig. 41 and 42. At most a slight "decrease in crystallinity" can be noticed, in the sense that sharp rings in the diffraction pattern from undamaged SnO_2 are superimposed on diffuse haloes from the damaged layer.

As a matter of fact reflection electron diffraction would have been more appropriate for looking at damage. Thus, in reflection electron

diffraction experiments, the depth of the solid that contributes to the pattern is about 20-30Å and thus is comparable to the range of our gas ions in the solid (see Matzke and Whitton, (1966)). We would therefore regard the present result that SnO_2 remains crystalline following ion impact as possibly misleading for it contradicts the results of section 6.3, that amorphous specimens remained amorphous.

6.6.

The reasons why we plan for the future to pursue this research on ion bombardment of SnO_2 films are the following:

(a) The bombardment of solids by heavy ions has been carried out to increase knowledge of atomic collision processes, including how they relate to such phenomena as secondary electron emission and sputtering.

(b) In addition, the implantation of inert-gas ions followed by thermal treatment of the bombarded solid has been undertaken to study diffusion processes and thereby provide information on the damage induced by bombardment.

(c) More recently, ion implantation has become important as a means of changing the electrical and chemical properties of the bombarded material. Of particular interest is the doping of semiconductors in order to produce changes in the conductivity of the material in a highly controlled manner. In this field, the technique is not merely a diagnostic tool but may well become an important addition to the present-day industrial technology of production of solid-state circuits and devices. Specifically, ion implantation has the potential of supplementing or replacing the diffusion process as a method for making p-n junctions. Potential advantages of ion implantation doping over diffusion techniques are listed in an article by Fairfield and Crowder (1969).

In the specific case of SnO_2, very little has been done so far with

respect to radiation damage studies. This is particularly surprising, as research on its semiconducting properties, as influenced by ion impact, should be rather feasable. The electronic configuration of the outer shells of the Sn and O atoms are $5s^2$, $5p^2$ and $2s^2 2p^4$ respectively. Therefore, in forming solid SnO_2 the 5s and 5p electrons of the Sn atom are transferred to O atoms. Each O atom can accept two electrons in its 2p orbital to form a stable octet. On this basis a picture of the band structure of SnO_2 consists of a 5s conduction band and a 2p valence band, separated by a forbidden gap. As the 5s band is a broad band, broad-band semiconduction is expected. In fact, on the basis of electron mobilities calculated from the conductivities of Sb-doped polycrystalline specimens and the behaviour of the Seebeck coefficient of such specimens, Lock (1963) confirmed that SnO_2 is a broad-band semiconductor. This agrees with Kohnke's (1962) conclusion, which was based on the Hall mobility and donor activation energy in natural single crystals.

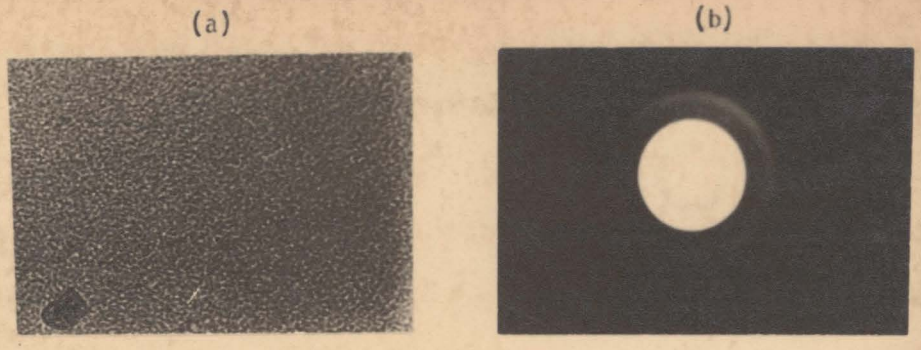

Figure 28. (a) Transmission and (b) diffraction micrographs of as deposited SnO_2. magn. 2.5×10^4-100KV.

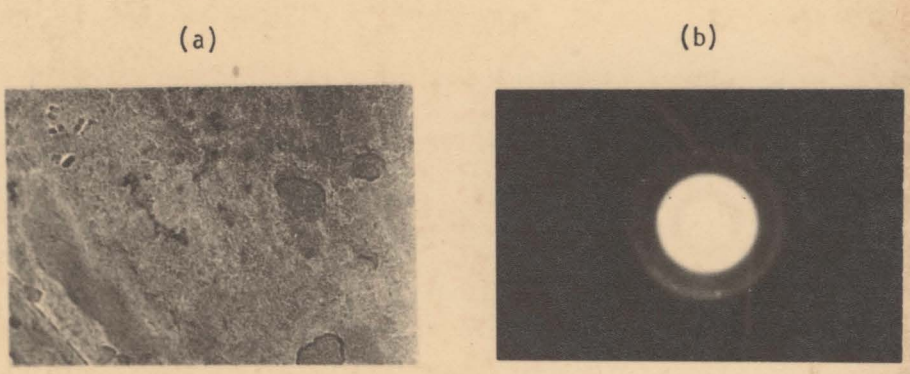

Figure 29. (a) Transmission and (b) diffraction micrographs of SnO_2 **films after bombardment with 35 keV krypton ions. Dose = 6μAx0.5 min/cm^2 magn. 2.5×10^4-100KV.**

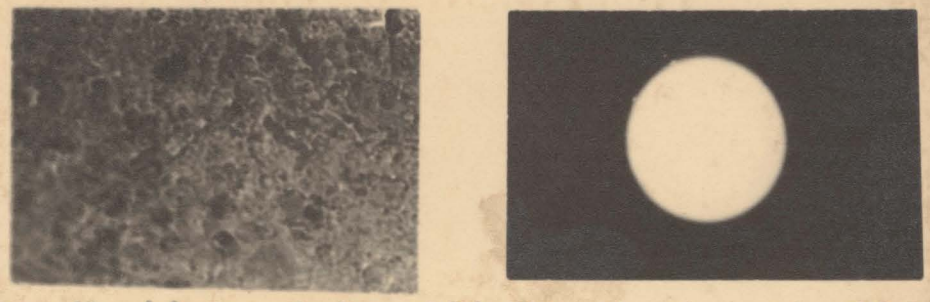

Figure 30. (a) Transmission and (b) diffraction micrographs of SnO_2 films after bombardment with 35 keV krypton ions. Dose = 10μAx30sec/cm^2. magn. 2.5×10^4-100KV.

(a) (b)

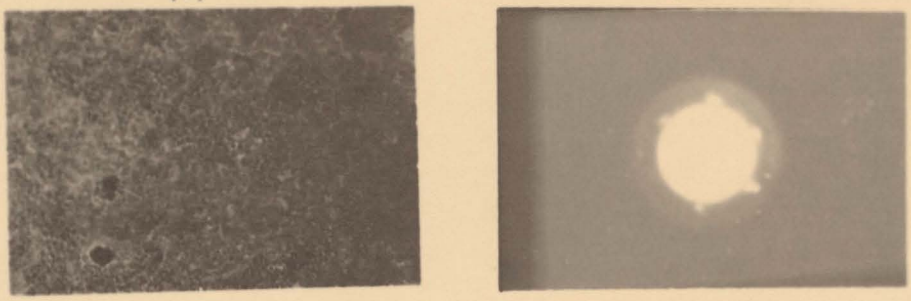

Figure 31. (a) Transmission and (b) diffraction micrographs of SnO_2 films after bombardment with 35 keV krypton ions. Dose: 4μAx1 min 15sec/cm^2. magn. $2.5x10^4$-100KV.

(a) (b)

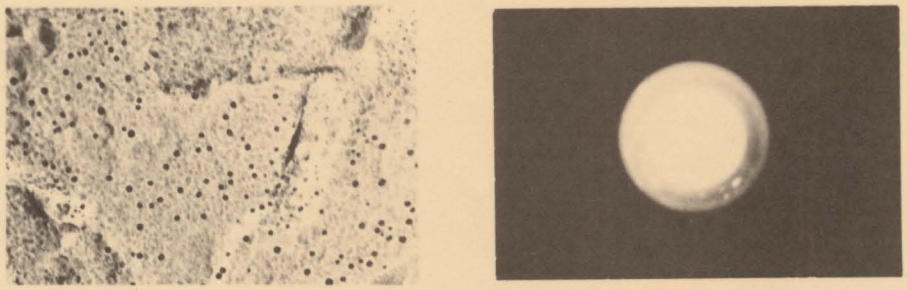

Figure 32. (a) Transmission and (b) diffraction micrographs of SnO_2 films after bombardment with 35 keV krypton ions. Dose: 6μAx1 min/cm^2. magn. $2.5x10^4$-100KV.

(a) (b)

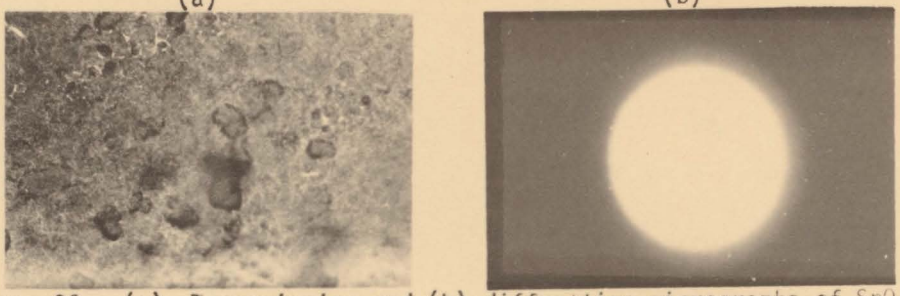

Figure 36. (a) Transmission and (b) diffraction micrographs of SnO_2 films after bombardment with 35 keV krypton ions. Dose: 6μAx2 min/cm^2. magn. $2.5x10^4$-100KV.

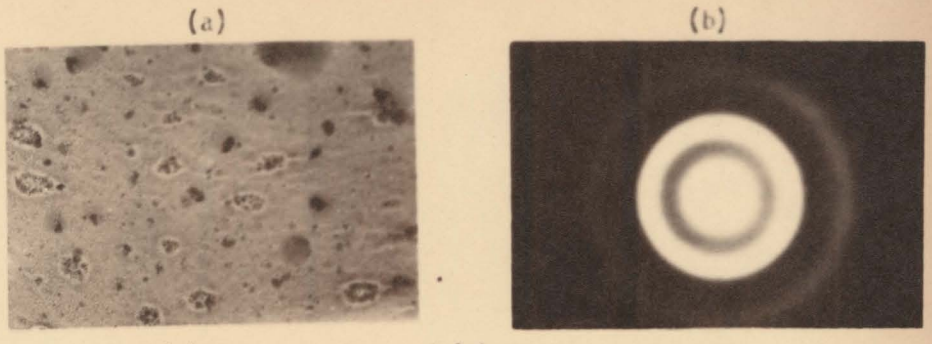

Figure 37. (a) Transmission and (b) diffraction micrographs of SnO_2 film after bombardment with 30 keV krypton ions for 6 min. Current $\simeq$ 12 μA magn. 10^4-80 KV.

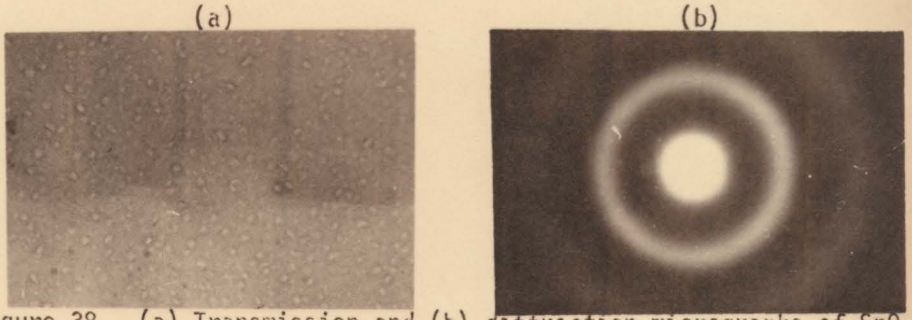

Figure 38. (a) Transmission and (b) diffraction micrographs of SnO_2 film after bombardment with 35 keV krypton ions for 30 min. Current $\leq$ 10 μA magn. 10^4-80KV.

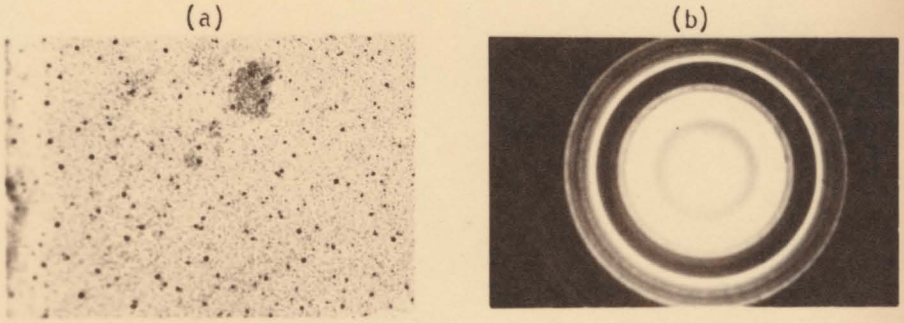

Figure 39. (a) Transmission and (b) diffraction micrographs of SnO_2 film after bombardment with 30 keV krypton ions. Dose: $\simeq$ 16 μAx2 min/cm^2 magn. 10^4-80KV.

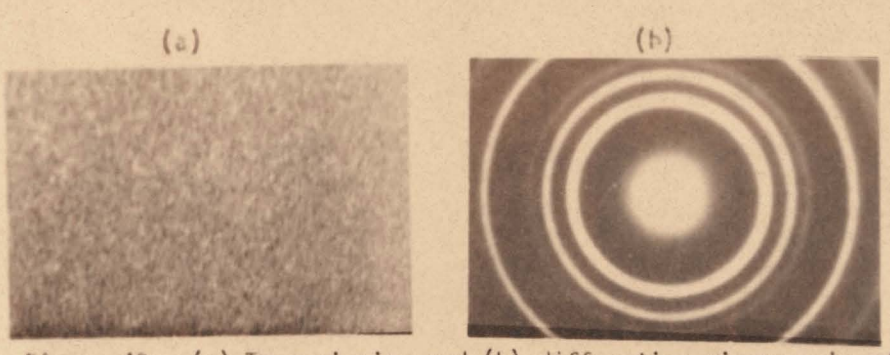

Figure 40. (a) Transmission and (b) diffraction micrographs of thermally crystallized SnO_2 film.

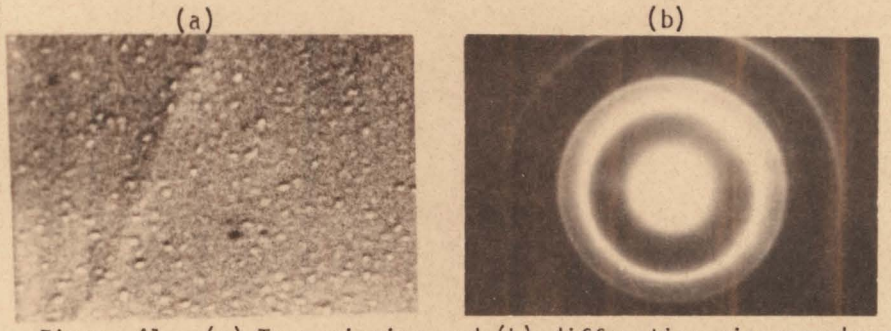

Figure 41. (a) Transmission and (b) diffraction micrographs of crystallized SnO_2 film, after bombardment with 35 keV krypton ions for 30 min. Current < 10 μA. magn. 10^4-80KV.

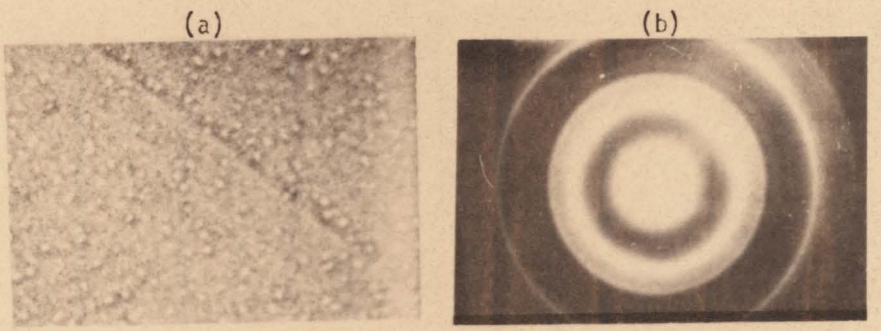

Figure 42. (a) Transmission and (b) diffraction micrographs of crystallized SnO_2 film, after bombardment with 35 keV krypton ions for 60 min. Current < 10 μA. magn. 10^4-80KV.

Part Three

RECENT EXPERIMENTS

Chapter 7

Crystallinity versus film thickness

7.1.

It was suggested in "Future experiments" (section 5.2c) that it would be of interest to investigate the dependence of crystalline state on film thickness, in the case of reactively sputtered SnO_2 films. Initial results have in the meantime been obtained.

7.2.

The substrates were not subjected to any thermal treatment, in the sense that their temperature was the one resulting solely by the glow-discharge effect.

7.3.

First of all we sputtered using a 50-50 mixture of argon and oxygen, a 3 KV tension, a 9mA current and 2 hours sputtering time: the purpose of this was to confirm, to begin with, the results (namely films crystalline as deposited) of section 3.6, where the same sputtering parameters had been used. The substrates temperature resulted to be, after 2 hr. sputtering, 65°C.

The result of section 3.6 was confirmed, as can be seen from Fig. 48.

7.4.

Then we started a systematic investigation, keeping constant all the sputtering parameters but the sputtering time, i.e. we used a 50-50 mixture of argon and oxygen, a tension of 2KV, a current of 4mA and the following choice of sputtering time: 15 min, 1 h., 1 h. 30 min., 2 h. 30 min., 3 h. 30 min. In all these cases the substrates temperature resulted to be 40°C. Films were wet-stripped from KCl supports and examined in the electron microscope.

Fig. 43, 44, 45, 46, 47, 48 show that films really change spontaneously from an amorphous to a crystalline state with increasing their thickness, at least at this value of substrate temperature. The trouble in recording diffraction patterns, as in Fig. 46, depends on the fact that the thicker the film, the less suitable for electron microscopy it becomes.

It should be noted that, in stripping films from KCl, some of them detach in two layers: first a thin surface layer and then the much thicker layer beneath: this in the case of very thick films, as when we sputtered for 2 hours with a current of 9 mA. Electron microscope examination reveals that both show the same structure, i.e. even the thin surface layer is crystallized (Fig. 48(a)(b) and (c)(d)).

In future experiments we will include among the KCl supports a clean Sn substrate so as to be able to estimate film thicknesses by interference colours.

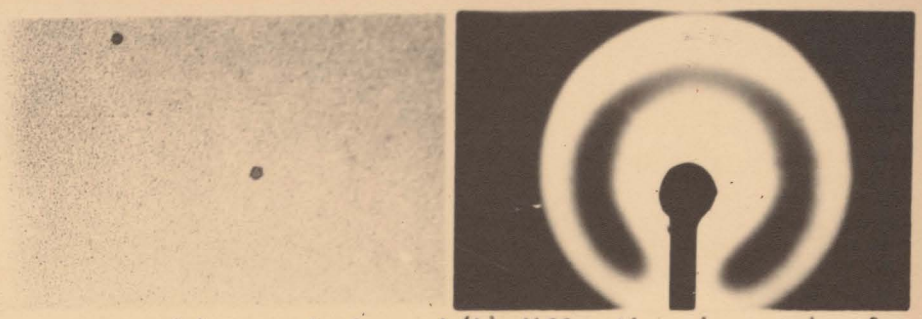

(b)

Figure 43. (a) Transmission and (b) diffraction micrographs of reactively sputtered SnO_2 film. Sputtering time: 15 min. (4mA-2KV). magn. 11,000-80KV. (60mAmin).

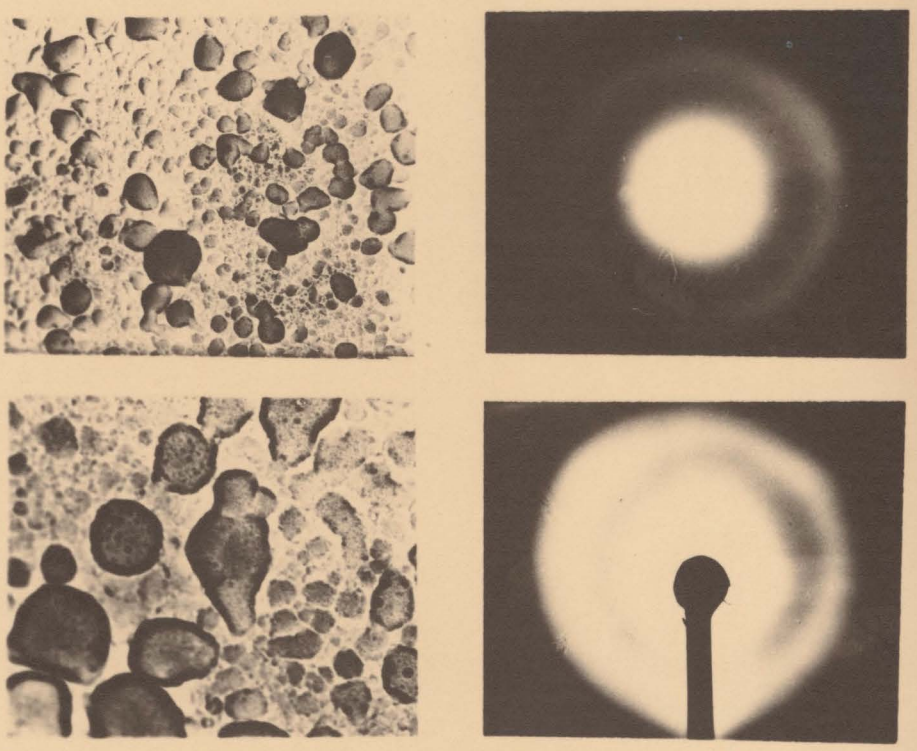

(b)

(d)

Figure 44. (a) (c) Transmission and (b)(d) diffraction micrographs of reactively sputtered SnO_2 film. Sputtering time: 1 hour (4mA-2KV) magn. (a) 11,000 and (c) 27,000-80KV (240mAmin).

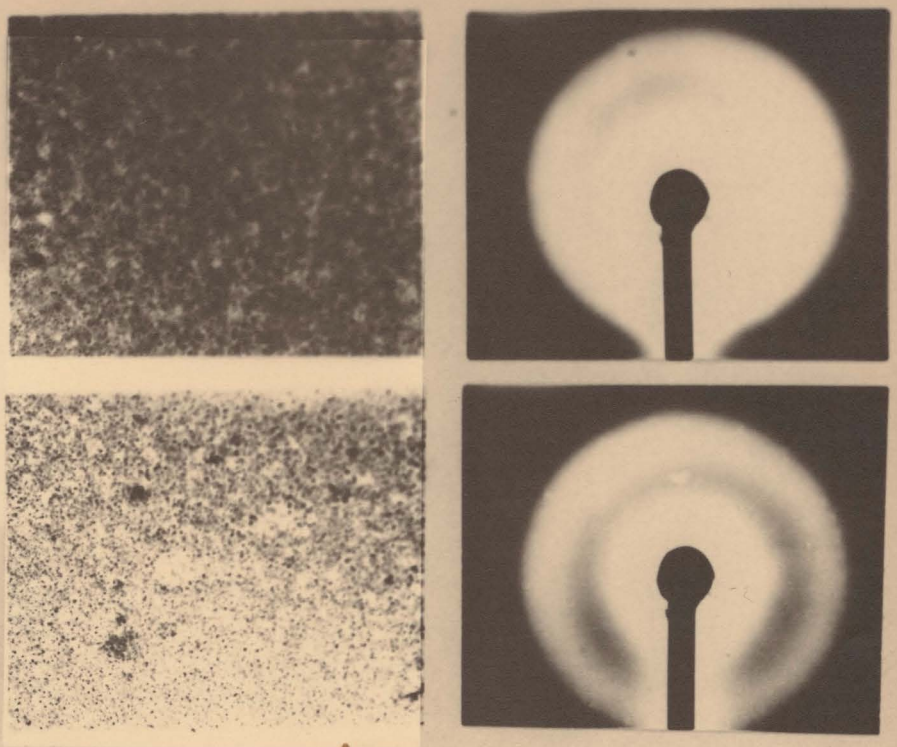

Figure 45. (a) (c) Transmission and (b)(d) diffraction micrographs of reactively sputtered SnO_2 film: Sputtering time: 2h. 30 min. (4mA-2KV) magn. 11,000-100KV. (360mAmin)

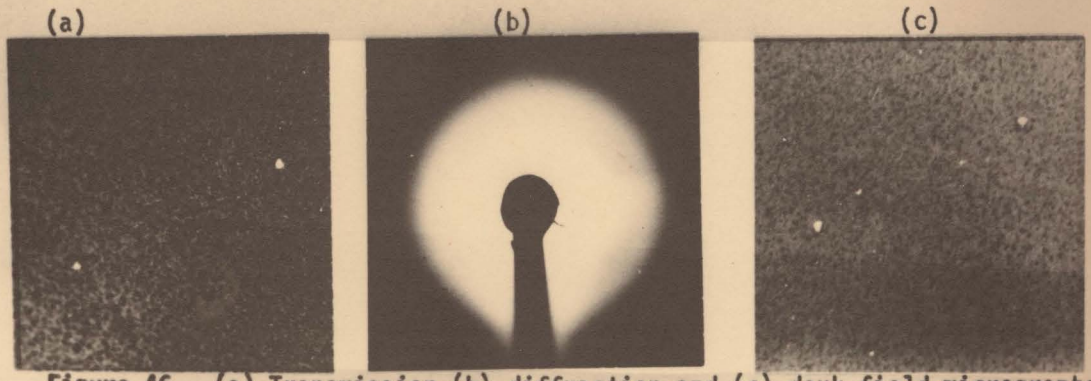

Figure 46. (a) Transmission (b) diffraction and (c) dark field micrographs of reactively sputtered SnO_2 film. Sputtering time: 2h. 30 min. (4mA-2KV) magn. 11,000-100KV. (600mAmin)

(a)

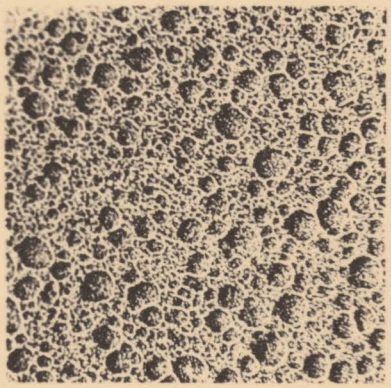

(b)

(c)

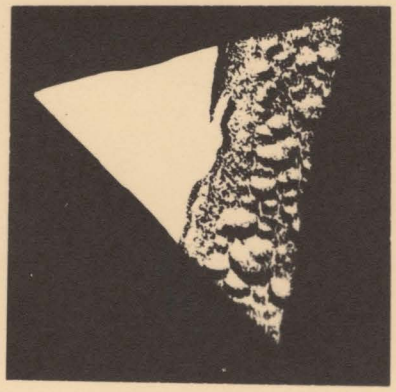

(d)

Figure 47. (a)(c) Transmission and (b)(d) diffraction micrographs of reactively sputtered SnO_2 film. Sputtering time: 3h. 30 min. (4mA-2KV). magn. 11,000-100KV. (840mÅmin)

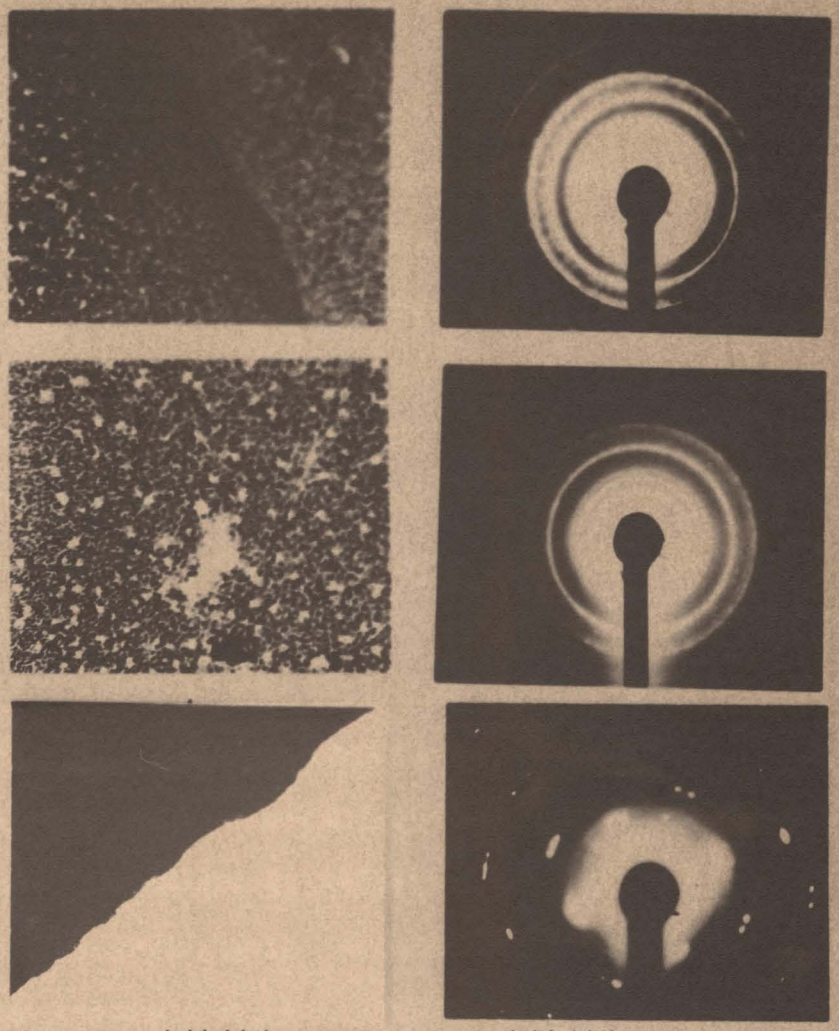

Figure 48. (a)(c)(e) Transmission and (b)(d)(f) diffraction micrographs of reactively sputtered SnO_2 film. Sputtering time: 2h (9mA-3KV).(1080mAmin)
(a)(c): thin surface layer of the film
(f): diffraction micrograph at film edge, as shown in (e).
magn. 11,000-100KV.

Chapter 8

Diffusion in Inert-gas Implanted SnO_2

8.1 General Comments

8.1.1.

As discussed in section 5.1 ("Future experiments"), Table XI demonstrates the validity of using inert-gas mobility as a means of estimating intrinsic self-diffusional mobility.

8.1.2.

During the past few years much work has been done on "rare gas release and diffusion" in nonmetallic systems (for an early survey see Matzke and Lindner, 1964). Kelly and Matzke (1965) and Kelly and Jech (1969) have proposed that diffusion in inert-gas bombarded solids can be described in terms of five basic processes or stages. Figure 49 shows a systematic sketch, for an annealing schedule with a linear increase of temperature with time; with such a heating schedule, a clear separation of the Stages is achieved since one Stage goes to completion before the next starts. Frequently, however, other experimental heating schedules are employed, e.g. isochronal annealing with fixed arrests at different temperatures. The release curves obtained in these studies (F-vs-T) represent the integral of the dF/dt-vs-T curves of Fig. 49. A separation of Stages is still easily possible. Finally, isothermal annealing is often used, and here, an overlapping of release due to all Stages occurring below and at the experimental temperature will be observed.

In any practical case, some Stage or Stages will dominate depending on the system being studied. The main parameters affecting the release are gas concentration,damage concentration, the physical form taken by the radiation damage or defects, and the distance of the gas atoms to a free

surface. On the basis of how the various Stages respond to these variables it has been possible to infer their origin as follows:

Stage I involves gas mobility at unusually low temperatures, namely, it designates release processes at temperatures significantly below those of normal volume diffusion. The latter starts to be the dominant process between 0.4 to 0.5 of the melting point on the absolute temperature scale. Stage Ia is probably due to gas fortuitously located in high mobility sites, e.g. in interstitial positions; Stage Ib is now well-established to be due to annealing of structural radiation damage, the most common form of which is radiation induced amorphousness.

Stage II involves gas mobility at normal temperatures i.e., temperatures similar to those of self-diffusion of the lattice atoms. Stage IIa is due to unperturbed mobility of single gas atoms probably involving vacancies, though perhaps vacancy clusters; Stage IIb is due to temporary trapping of the gas, i.e. to weak interactions of gas atoms with radiation damage, with pre-existing defects, or with other gas atoms.

Stage III involves gas mobility at unusually high temperature and is due to strong trapping of the gas at pre-existing defects or in gas-filled bubbles.

8.1.3.

Stage IIa, as we said, is probably due to gas in sites similar to normal substitutional sites. Kelly and Matzke showed that for F, the fractional release of Stage IIa gas, equal to 0.5 the following is true for virtually all geometries:

$$\Delta H/T_{50} = 75.0+4.58\log_{10}\{t_{min}D_o/(R_m^2 0.3)\} \qquad (5.a)$$

SYSTEM OF STAGES IN GAS RELEASE

$T \ll T_{sd}$	$T \approx T_{sd}$	$T > T_{sd}$
	range of self diffusion	
stage I	stage II	stage III

Figure 49

Here isochronal heating for t_{min} minutes is assumed, $D = D_o \exp(-\Delta H/RT)$ is the diffusion coefficient for Stage IIa in cm^2/sec, T_{50} is the temperature for 50% gas release in °K, ΔH is in cal/mole and R_m is in units of λ, mean atomic spacing ($\lambda \simeq 2.5\mathring{A}$). Similarly the peak value of dF/dt for experiments carried out with linear temperature rise also infers a value of $\Delta H/T$:

$$\Delta H/T_m \simeq 68 + 4.6 \log_{10}\{T_m D_o / R_m^2 \beta_{min} 0.3\} \qquad (5.b)$$

where β_{min} is in °C/min ($T=\beta t$) and T_m is the temperature at which the gas release rate dF/dt maximizes in an experiment involving a linear increase in temperature. It is permissible with many metals, halides and oxides to replace $D_o/0.3$ by $10^{0\pm1}$ (Lazarus, 1960; Kelly and Matzke, 1965). Table XII and XIII (from Kelly and Matzke, 1966) give $\Delta H/T$ formulae for use with measurements of F or dF/dt. Note that the peaked or "xe^{-x}" distribution is used for low-mass, polycrystalline targets, and the exponential or "e^{x}" distribution for high-mass, polycrystalline targets. R_p indicates the most probable or peak range, R_m the median or 50% range, i.e. the thickness of the layer in which 50% of the ions have come to rest. For an xe^{-x} geometry, the theoretical median range is $R_m = 1.68R_p$.

Equations (5a) and (5b) can be used to derive "self-diffusion temperatures" from conventional volume self-diffusion parameters. Table XI shows that for a wide variety of systems, all of which involve low or moderately low doses, release components occur having similar temperatures to those of volume self-diffusion. The resulting correlation with self-diffusion is such that the following is true:

$$T_{IIa} = (0.86\pm0.10)T_{self\text{-}diffusion} \qquad (6)$$

Table XII

$\Delta H/T$ formulae for use with measurements of cumulative gas-release †.

Geometry or type of diffusion	A for $F_1=0.1$	A for $F_1=0.5$	A for $F_1=0.9$	B (in units of λ)
plane source	78.8	75.2	68.5	R_p or R_m
"xe^{-x}"	80.9	75.2	67.9	R_m
"e^{-x}"	83.3	75.0	67.2	R_m
sphere with radius a	89.3	82.2	78.8	a
single-jump diffusion with discrete ΔH	81.3	77.5	75.1	(unity)

† The basic expression is $\Delta H/T = A + 4.6 \log_{10} t_{min}/B^2 + 4.6 \log_{10} k_0/10^{15}$, where ΔH is in cal/mole, t_{min} is in min and k_0 is in sec^{-1}.

Table XIII

$\Delta H/T$ formulae for use with measurements of dF_1/dt under conditions of linearly increasing temperature †.

Geometry or type of diffusion	kt/B^2 for $d^2F_1/dt^2=0$	A for $d^2F_1/dt^2=0$	B (in units of λ)
plane source	1	69.5	R_p or R_m
"xe^{-x}"	1.8	68.3	R_m
"e^{-x}"	2.7	67.5	R_m
sphere with radius a	0.16	73.2	a
single-jump diffusion with discrete ΔH	1 ††	69.5 ††	(unity)
single-jump diffusion with spectrum of ΔH's	no maximum [27]	.....	.....

† The basic expression is $\Delta H/T_m \approx A + 4.6 \log_{10} T_m/B^2\beta_{min} + 4.6 \log_{10} k_0/10^{15}$, where ΔH is in cal/mole, β_{min} is in °C/min and k_0 is in sec^{-1}.

†† This result agrees with [26, 28].

where T stands for absolute temperature.

One possible conclusion is that Stage-IIa data serve as a surprisingly effective indication of the volume self-diffusion comportment of a solid.

An alternative use of eq. (5) is to use the temperatures of stage-IIa gas-release to infer activation enthalpies. For an extensive review of such ΔH's, one is referred to work by Matzke (1968), where he also says that ΔH for low-dose gas release can be attributed to Stage IIa and is found to be about 32±4 times the melting temperature. In addition, Matzke has demonstrated the following correlation:

$$\Delta H_{IIa} = (0.80 \pm 0.10) \Delta H_{self\text{-}diffusion} \qquad (7)$$

where ΔH is that appropriate to self-diffusion of the slower moving ion.

It is to be noted that Stage IIa correlates, though with several unexplained exceptions, mainly with low doses and with low energies (see Kelly and Matzke, 1965 and Matzke, 1967).

8.1.4.

What is summarized above is another track we are going to follow in our experiments with SnO_2. Specifically our program has been first of all to try to deduce, by gas release technique, self-diffusion and melting temperatures. It is worth noting that the melting point for tin oxide is variously reported in different handbooks between 1127 and 1900°C. The 1127°C value has been checked by Sinclair et al. (1965), and they claim it is certainly wrong; likewise, in our own work, we find no melting point at 1400°C. But the 1900°C temperature may be wrong too, for it appears to be a sublimation temperature.

Supposing we can determine, using a certain annealing schedule of our Kr-implanted SnO_2, the peak corresponding to Stage IIa. If so, we

can deduce the temperature range for self-diffusion (of the less mobile lattice species) and the melting point using the empirical rules given in section 8.1.3.

As it appears from Table XI, XII and XIII, in order to properly evaluate gas-release data, it is necessary to know the initial location of the injected atoms. Depth distributions are usually obtained by the techniques of anodizing-stripping (Davies et al. 1963) or low-energy sputtering (Heinen et al. 1964). The first technique is applicable to some metals only, while the second has the disadvantages both of needing a complicated experimental set-up and of giving perturbed ranges (Kelly, 1968). Recently, however, a mechanical method employing a vibratory polisher has been shown to be useful in removing thin (20Å) layers from a variety of materials including non metals, provided the materials is not too soft (Whitton, 1965 In the latter case, a chemical dissolution method can be used: range curves can be obtained by immersing the specimens, after bombardment, for appropriate times in the proper solvent and then counting the radioactivity remaining in the crystal.

In the case of SnO_2 we have derived, by interpolation, an approximate value for 35 keV Kr^{85} ions. We have plotted R_m values (in $\mu g/cm^2$) versus molecular weight, for 35 keV ions in Al_2O_3, WO_3 and Ta_2O_5. Data were obtained from articles by Domeij et al. (1964) and J.P.S. Pringle (unpublished data).

In this way we have figured out an approximate value of 134± 44 Å for R_m of 35 keV ions in SnO_2.

Another aspect we'll take care of is the annealing of structural radiation damage, the most common form of which is radiation induced amorphousness. Stage Ib is the one related to such annealing. In such a

way we should be able to confirm the values of crystallization temperature we determined by electron microscopy. This would presuppose the usual assumptions that the implanted ions come to rest within the amorphized layers, i.e. not in the crystalline matrix, and are swept out during the crystallization process.

As a matter of fact, the most straight forward mechanism for disorder annealing, as pointed out by Jech and Kelly (1969), follows from the correlation with cation self-diffusion, namely it is similar to the growth of a finite crystal into an undercooled liquid, the growth proceeding both from the macroscopic disorder-crystal interface and from any remnant crystalline regions. This phenomenon has been discussed in detail by Hartshorne (1949) and by Turnbull and Cohen (1960). In the case of bombardment-induced disorder, the disorder-crystal interface would be expected to sweep along the bombarding ions, e.g. inert gas, and finally cause their release at the surface.

8.2 Experimental

8.2.1.

The SnO_2 specimens used throughout this study were prepared from tin oxide powder. Pellets were pressed and then sintered in air at 1100°C for 2 hours. Labelling of SnO_2 with radioactive Kr^{85} gas was performed using the accelerator described in Section 3.2.1. Charge build up was avoided by using beam areas larger than the sample, so that secondary electrons were produced on the metal target support (see Kelly and Matzke, 1965). Beams of 10, 25, 30, 35 KV were used.

Ion doses used were: 1.25; 3; 4.5; 10; 15; 20; 25; 40 μA min/cm^2. Currents were: 2; 2.5; 4; 5; 6; 9; 10; 20 μA, the low values of current being used to make sure not to heat the sample, since heat can anneal amorphousness created by ion impact, if any. Ion doses in terms of ions/cm^2

can be derived using the relation $1\mu Amin/cm^2 = 3.74x10^{14}$ ions/cm^2 (Matzke and Whitton, 1966).

After labelling, the samples were transferred into a quartz container which was inserted into an electric furnace. A thermocouple served to measure the temperature in the sample when the latter was subjected to thermal treatment. Through the container with the sample a stream of gas was passing at a rate of 100 ml/min and served to carry the released radioactive gas away. The thermal treatment consisted in raising the temperature of the sample linearly at a rate of 25°C/min. The release was followed by measuring the activity in the gas stream as it passed through a counting cell with one wall being placed next to an end window GM counter. The counter was connected to a recorder, so that gas-release spectra were obtained directly. The experimental arrangement used is shown schematically in Fig. 50.

Annealings were performed in a stream of either oxygen (to avoid reduction) or helium.

8.2.2.

Diffusion measurements were carried out also in a different way: after bombardment, specimens were step heated, i.e. alternately heated isothermally in air with hold times of 10 min., and then cooled to room temperature for counting. The heatings were spaced at intervals $\geq$ 75°C so that each heating could be treated without regard to those preceding it (cf. Section 4.5 of Kelly and Matzke, 1966). Specimens analyzed by step-heating had been bombarded at 35 KV with doses of 20μA min/cm^2 and 10μA min/cm^2 of radioactive Kr^{85} ions.

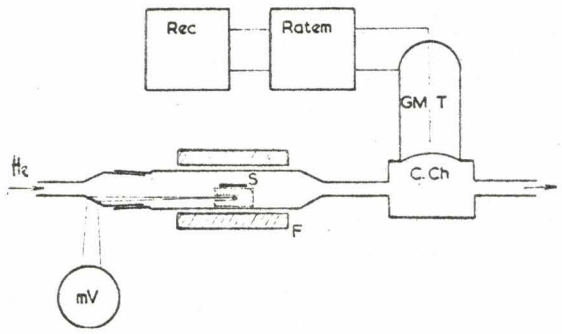

Figure 50. Apparatus used for differential gas-release measurements. Shown are voltmeter for thermocouple (mV), sample sitting on Sintox boat (S), quartz tube furnace (F), counting chamber (C.Ch.), Geiger-Müller tube (GMT), count rate meter (Ratem), and recorder (Rec.).

8.2.3.

Finally we have performed measurements of gas release in ion implanted (radioactive Kr^{85}) metallic tin. Beams of 35 KV were used, and two different doses: 20μA min/cm^2 and 10μA min/cm^2. Current used were 20μA and 10μA. Annealings were carried on in either a stream of oxygen or hydrogen, and heating rates used were 25°C/min and 10°C/min.

8.3 Results

8.3.1.

In all SnO_2 annealing experiments under conditions of linearly increasing temperature, diffusion of implanted ions did not occur before $\lesssim$ 1000°C. The maximum release rate was observed at $\lesssim$ 1200°C, which was also similar to the highest temperature reachable in our furnace (exactly 1230°C).

A typical example of differential release curve obtained with Kr^{85}, showing the bell shaped peak at $\sim$ 1200°C, is that of Fig. 51, where a heating rate of 25°C/min was used.

Reported in ordinates is the fractional release rate, dF/dt, in

arbitrary units. Approximately 20% of the activity remained at the highest temperature reached, since the activity of the sample decreased from $\sim$ 5800 counts/20 sec before annealing to a value of $\sim$ 1200 counts/20 sec after annealing.

The above SnO_2 pellet had been labelled with a beam of 35 KV, and a dose of 9μAx30 sec/cm^2, and release was carried on in oxygen flow. On the other hand all the rest of the experiments showed similar results, independently of the different experimental parameters listed above.

8.3.2.

In order to be able to observe gas release behaviour at higher temperature than 1200°C, specimens were alternately heated isothermally in air with hold times of 10 minutes, as already mentioned. A furnace has been used, that allowed for temperatures as high as 1400°C to be reached. While we have confirmed diffusion occurring not before $\sim$ 1000°C, we have found in this way that inert gas atoms are completely annealed out at $\sim$ 1400°C.

Fig. 10 is the integral release curve showing the percentage of activity remaining in the sample, versus temperature. As already mentioned the samples used here were bombarded at 35 KV with doses of 20μAx30 sec/cm^2 and 20μAxmin/cm^2.

8.3.3.

Finally, after chemical polishing of metallic tin, we bombarded it with high energy (35 KV) Kr^{85} ions, in order to make a significant fraction of the ions go through the oxide layer inevitably present on the surface, and be implanted in the metal. No gas release occurred before the tin melting point (232°C), as was expected and as shown in Fig. 53.

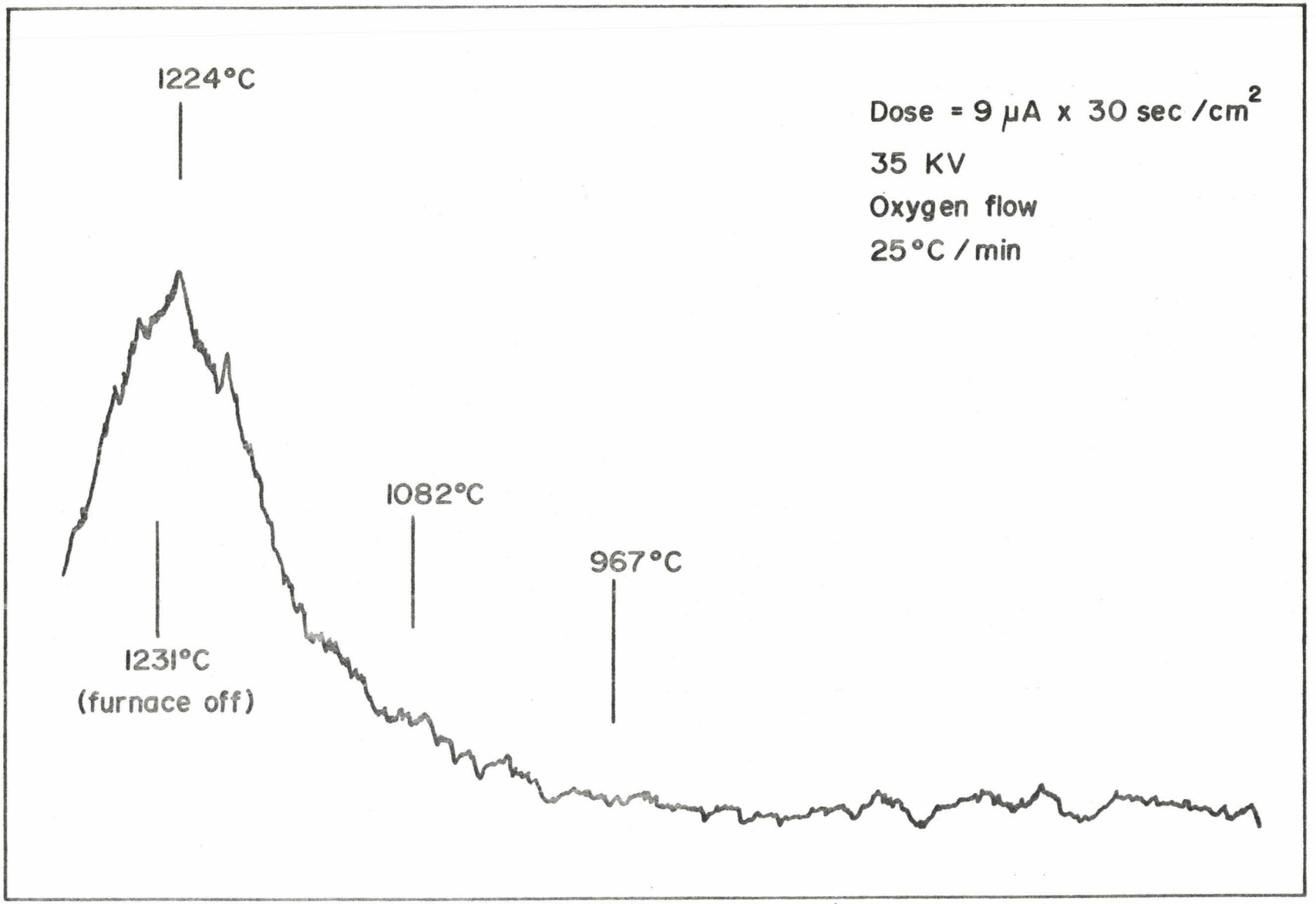

dF / dt vs. T°C

Figure 51

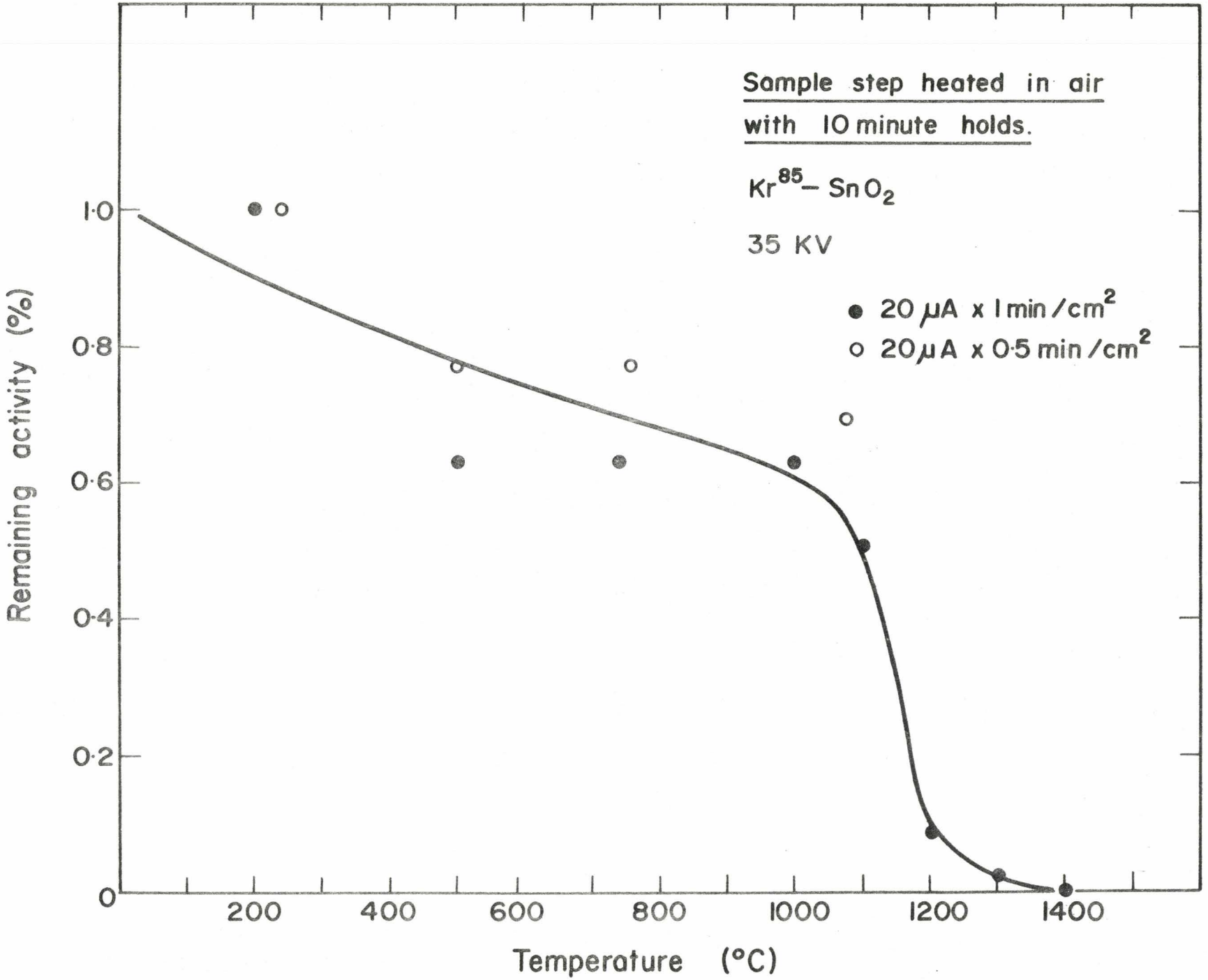
Sample step heated in air
with 10 minute holds.
Kr^{85}– SnO_2
35 KV
● 20 μA x 1 min/cm²
○ 20 μA x 0·5 min/cm²
Remaining activity (%)
1·0
0·8
0·6
0·4
0·2
0
200
400
600
800
1000
1200
1400
Temperature (°C)

Figure 52

Figure 53

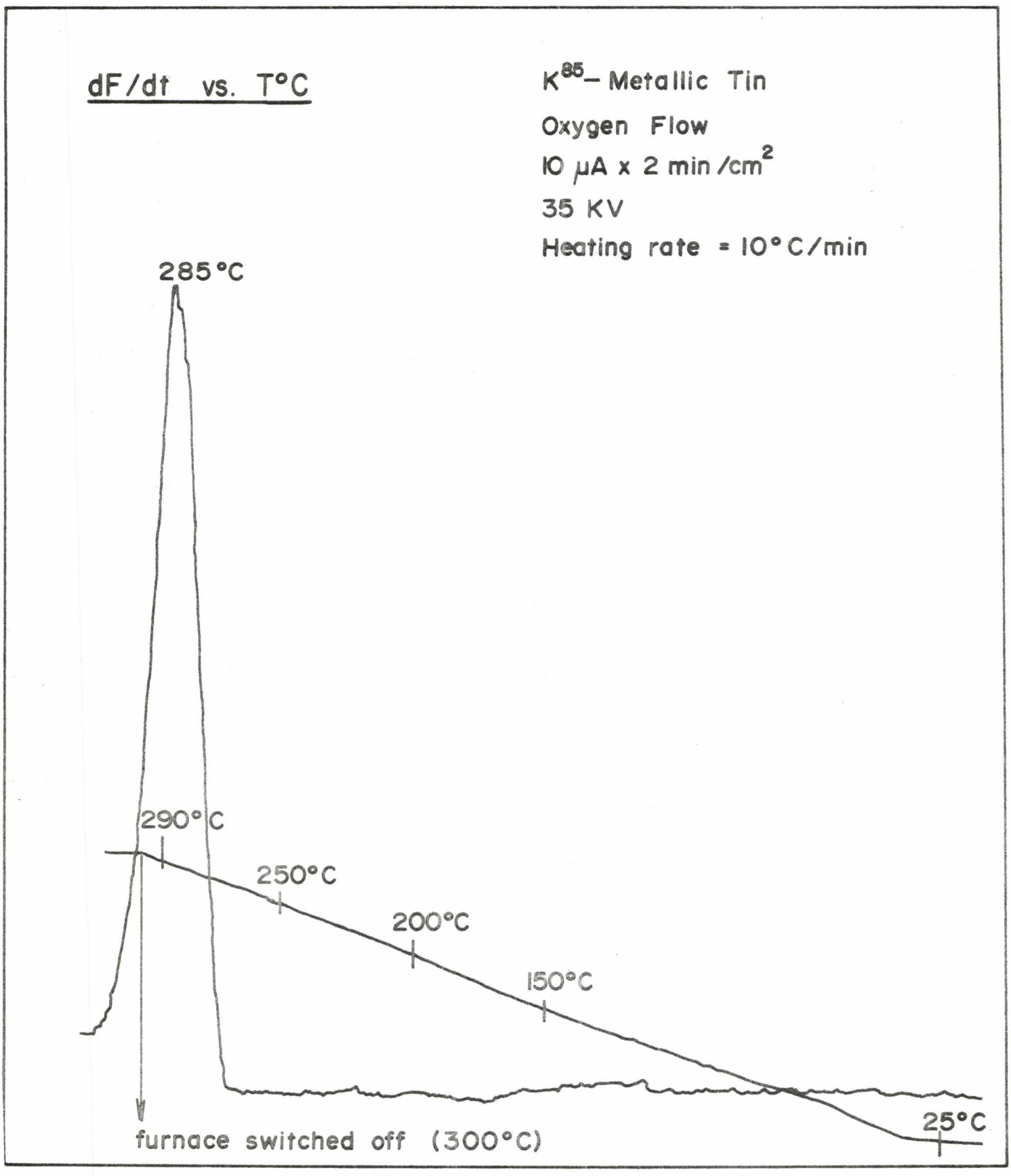
dF/dt vs. T°C
K85 – Metallic Tin
Oxygen Flow
10 μA x 2 min/cm2
35 KV
Heating rate = 10°C/min
285°C
290°C
250°C
200°C
150°C
25°C
furnace switched off (300°C)

8.4 Discussion

8.4.1.

The electron-microscope evidence of whether SnO_2 is amorphized by ion bombardment (cf. Chapter 6) was tentatively negative, while the gas-release evidence was strongly negative. There is thus apparent agreement. However, it is still possible that SnO_2 is really amorphized by ion impact, and the release experiments would thus show that crystallization occurs without the implanted ions being swept out. Such a phenomenum would be quite unusual, and has been observed only rarely: Fairfield and Crowder (1969) showed that for Arsenic implanted in Si at a concentration $\leq 10^{14}$ cm^{-2}, the dopant is not driven out during annealing (900°C). Also P doesn't move or get swept out at temperatures $\leq$ 800°C, while Bi, Rb, Cs, Se, and Sb appear to behave similarly. On the other hand, Meyer and Mayer (1970) showed that the usual correlation is established between the reordering of amorphous layer and decrease in the total number of implanted atoms for Zn, Cd, I and Hg implants in Si. The inert gases Kr and Xe also behaved normally in Si (Jech and Kelly, 1969; Matzke, 1970).

As a matter of fact dissolution experiments should be performed at this point. A solvent should be found in order to dissolve the amorphized layer but not the non-disordered part of the sample. In this way one could infer in still a further way what was the result of ion impact in SnO_2.

8.4.2.

It is worth noting that one of the problems with the gas-release apparatus used was that there is a time lag for the flowing gas to reach the counting chamber and a further hold-up within the counting chamber. This means that the apparent temperatures, as recorded in Fig. 51 and 53, are too high. Specifically in Fig. 53, where we have T_m = 285°C, the recorded temperature is too high by 53°C (since we know that the melting

point for tin is 232°C). This value of the temperature shift does not apply to Fig. 51, where, though the rate of flow of inert gas is the same, the heating rate is 25°C/min. Taking advantage of another gas release experiment in metallic tin, where the rate of inert gas flow and the heating rate were the same as for the experiment recorded in Fig. 51, we deduce that in the case of Fig. 51 the recorded temperature is too high by 83°C.

The following calculations have therefore been made by taking this into account.

8.4.3.

Since the temperature for the onset of gas diffusion (i.e. temperature for 10% gas release) is in our case approximately 1300°K, it is seen from Fig. 54 (Matzke, 1958) that the melting point of SnO_2 is between 2600 and 3150°K. This agrees roughly with what was already mentioned in section 8.1.2., i.e. that the temperature for 10% release ($\sim$1300°K in our case) is 0.4 - 0.5 of the melting point (this statement, actually, was deduced just from Fig. 54). On the other hand, applying relation (5b) and taking T_m = 1414°K (as from Fig. 51) we find for ΔH_{IIa} a value ranging between 78,500 and 91,500 cal/mole. Since, as we said, $\Delta H = (32 \pm 4)\ T_m$ cal/mole, we deduce for $T_{melting}$ a value ranging between 2200 and 3300°K.

We have thus estimated the melting temperature range for SnO_2 in two ways, i.e. using the experimental values of the temperature for 10% release and of the temperature at which gas release rate maximizes. The range for $T_{melting}$ common to both calculations is therefore between 2600 and 3000°K.

What makes the procedure employed reliable, is the fact that the linear relations in Fig. 54 and 55 are obtained by data from a great

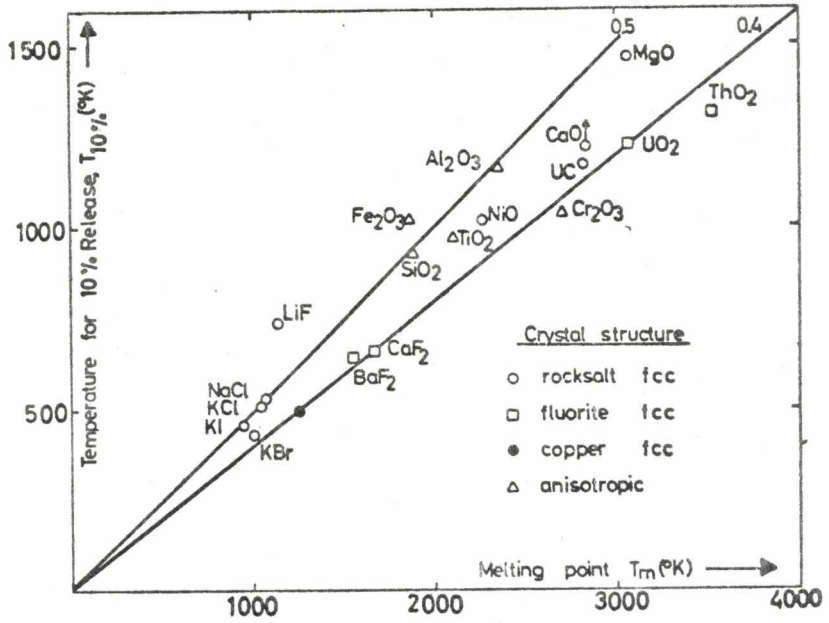

Fig. 54 The onset of the release of heavy rare gases as a function of the melting point on the absolute temperature scale (after Matzke, 1968).

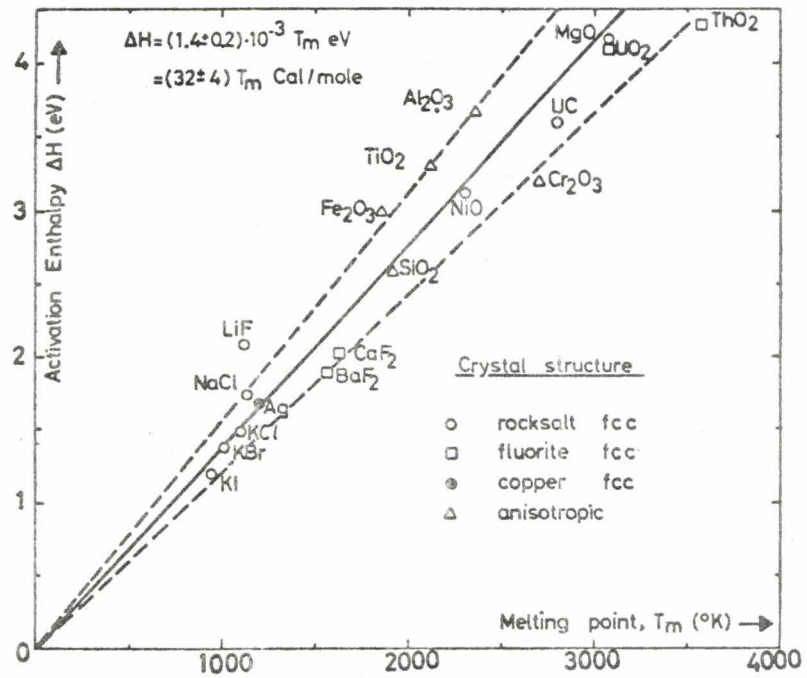

Fig. 55 The activation enthalpies for the release of heavy rare gases as a function of the melting point on the absolute temperature scale (after Matzke, 1968).

number of different materials, namely halides, oxides and a metal, both cubic and anisotropic substances. They imply a mechanism for the diffusion of the heavy rare gases similar to, though not necessarily identical with, that of the self-diffusion of the less mobile ion. In fact the latter has onset temperatures of about 0.5 $T_{melting}$ and follows approximately a relationship of the type $\Delta H = 39\ T_m$ cal/mole (Le Clair, 1965).

8.4.4.

We will now apply relations (6) and (7) to determine the self-diffusion temperature and activation enthalpy of the slower moving ion in SnO_2. The values we deduce are

$$T_{self\text{-}diffusion} = 1480 - 1870°K$$

$$\Delta H_{self\text{-}diffusion} = 87{,}200 - 131{,}000 \text{ cal/mole}$$

The problem enters now that there is virtually nothing in the literature with which one could determine the identity of the slower moving ion or with which one could compare the values of self-diffusion temperature and self-diffusion enthalpy we just found. Nothing is known about the defect structure in SnO_2 as well.

We can though report results given by investigations on similar materials and consider how feasible it is to apply them to SnO_2.

To have an idea of which one can be the slower moving ion, we'll consider other researchers' work on diffusion in CoO, Al_2O_3, MgO, Cr_2O_3. The choice of these oxides depends on the fact that, besides presenting ionic bonds, as SnO_2, they all have close packing of anions. In SnO_2, in fact, the cation has an octahedral coordination, while there is close packing of anions. The same applies to CoO, MgO, Al_2O_3, Cr_2O_3 and this fact can already be assumed to be an indication of the oxygen ions being the less mobile. Coordination numbers of cations and anions in SnO_2, CoO, MgO, Al_2O_3, Cr_2O_3, are respectively 6:3, 6:6, 6:6; 6:4; 6:4.

As reported by Holt (1967), CoO belongs to a group of defect solids in which the non stoichiometry results from a deficiency of the metal component. These vacancies in the cation sub-lattice, allied with the smaller ionic radius of the cobalt ion, account for the greater mobility of the cobalt ion with respect to the oxygen ion, since a diffusion coefficient depends on the concentration of vacancies as well as on the activation energy required for movement through the structure. Holt applied the ^{18}O proton activation technique to the study of volume diffusion of oxygen in CoO; using Thompson's (1962) gaseous exchange data and his own data on oxygen diffusion coefficient in CoO, he plots log D versus 1/T, from which we derive a value of the activation enthalpy $\leq$ 37,000 cal/mole. He reports also evidence of preferential diffusion of oxygen at grain boundaries, stating that oxygen will naturally move along the path of least resistance, such as grain boundaries, in oxides where cation vacancy concentration is much larger than the oxide ion vacancy concentration, a situation that is realized in the majority of oxides. Systems where oxygen grain-boundary diffusion has been experimentally verified include Al_2O_3 (Oishi and Kingery, 1960) and MgO (Holt and Condit, 1966). The presence of grain boundaries does enhance anion diffusion also in alkali halides (Laurent and Benard, 1955 and 1958).

Paladino and Kingery (1962) report that a comparison of oxygen diffusion data with aluminum ion diffusion in aluminum oxide indicates that aluminum ion mobility is greater than oxygen ion mobility (which is also consistent with ionic size consideration). Oxygen ion diffusion data obtained by Oishi and Kingery (1960) for polycrystalline aluminum oxide give a value of 110,000 $\pm$ 1,500 cal/mole for the diffusion enthalpy.

Oishi and Kingery (1960) studied the oxygen diffusion in Periclase (MgO) crystals. They found that the diffusion coefficient for oxygen

in this material is about two orders of magnitude less than that reported in the literature for magnesium. This is similar to results for alkali halides (Laurent and Benard, 1957) and is not unexpected for magnesium oxide which has the sodium cloride structure. Value reported for activation energy for diffusion is 62,400 cal/mole. By comparison with NaCl and also with Al_2O_3, they claim that this result corresponds to impurity-controlled or structure-sensitive diffusion.

Hagel (1965) studied anion diffusion in α-Cr_2O_3 and found that anion are the slower (three to four orders of magnitude) diffusing species in this oxide, and that the activation energy for anion self-diffusion is 101,000 cal/mole.

From all the above results (except CoO), it is therefore very likely that the value we found, 87,200 - 131,000 cal/mole, is the activation energy for oxygen ion diffusion. We have no explanation for the low activation energy for O motion in CoO, assuming that the value is in fact correct.

8.4.5.

In order to get a better understanding of the diffusion mechanism of the heavy rare gases in SnO_2 we might be able, in future, to undertake the recently developed "channeling technique", by which the position of rare gas atoms can be studied directly. Such an experimental apparatus is under construction in our Department. Anyway, diffusion experiments on doped specimens and "channeling" experiments (as reported by Matzke,1968) prove that the heavy rare gases do not diffuse via single vacancies in ionic crystals. Interstitials sites are excluded for some materials as well, except for very short diffusion distances. Rather, a mobility in small equilibrium clusters is indicated. For the latter, stoichiometric associations of cation and anion vacancies are suggested, for example

divacancies for KCl and trivacancies for UO_2. Matzke (1970) reports that the most probable mechanism of stage IIa, the diffusion of single gas atoms in virtually undamaged UO_2, is confirmed to be via Schottky trios, i.e. molecular voids in UO_2.

8.4.6.

The question may arise if the release peak of Fig. 51 is really due to stage IIa.

Stage Ia, as we already said, is expected as a fast release process at low temperatures, most probably involving the release of gas atoms that fortuitously come to rest in a high mobility site, i.e. interstitial positions. The reason why we do not notice stage Ia in our experiment (see Fig. 51) is probably because stage Ia is most prominent at low bombardment energies and low doses, and can generally be suppressed by using high bombardment doses which lead to high concentration of trapping sites.

The reason why we do not notice stage Ib as well, has been given in section 8.4.1. - i.e. SnO_2 is apparently not amorphized by ion impact.

Stage III involves gas mobility at unusually high temperature and is due to strong trapping of gas at pre-existing defects or in gas-filled bubbles. But this can't be our case, otherwise we would have noticed such defects in transmission electron micrographs of bombarded samples (see Chapter 6).

We have thus shown by exclusion the feasibility of our interpretation (stage II) of the release peak in Fig. 51.

In order to decide if we are dealing with stage IIa or IIb, the argument of Kelly et al. (1968) can be followed.

As we said in section 8.1.3, stage IIa correlates, though with several unexplained exceptions, mainly with low doses and with low energies. The above mentioned authors propose that the low-dose release involves gas

motion without an implied gas-gas or gas-damage interaction. The high dose release seems, by contrast, to be affected by transient gas-gas or gas-damage interaction. The probability that a gas atom will escape without getting trapped is exp(-p/L), where p is the depth of the atom beneath the surface and L is the diffusion length for trapping (Kelly & Matzke, 1966; Hurst, 1962). L is in turn proportional to (volume of trapping zone)$^{1/2}$/(number of trapping centers)$^{1/2}$, i.e. approximately to (p/dose)$^{1/2}$ for gas-gas trapping and to 1/(dose)$^{1/2}$ for gas-damage trapping. It finally follows that p/L is proportional to either (p xdose)$^{1/2}$ or p(dose)$^{1/2}$ for the two kinds of trapping, so that the escape probability should be higher for low doses or low energies.

In our experiments, as reported in section 8.2.1, we have been using energies ranging between 10 and 35 kV, and doses ranging between 1.25 and 40 μAmin/cm^2 (all experiments showed results similar to the one recorded in Fig. 51). Precisely the combination of dose and energy was as follows:

dose (μAmin/cm^2)	energy (KV)
1.25	35
3	35
4.5	35
10	30
10	35
15	30
20	10
20	25
20	35
25	10
40	30

We have found out the median range for 35 kV (p (35)) but unfortunately we do not know its value at lower energies (e.g. p (10)), though, the product (p x dose) probably minimizes when the values of dose and energy used were respectively 1.25 and 35. In any case there seems to be a need for further experiments at lower doses in order to definitely attribute to stage IIa (and not stage IIb) the gas release peak in Fig. 51.

Besides, we'll have to make sure that the process we attribute to stage IIa is well distinguishable from release due to vaporization (see Kelly et al., 1968). With SnO_2, the relevant process is

$$SnO_2 = SnO + 1/2\ O_2$$

8.4.7.

Finally a few comments about gas release in ion implanted metallic tin.

Comparing release behaviour in metallic tin and in SnO_2, we note that in the case of SnO_2 the implanted ions never had a chance to meet grain boundaries, due to the short distance they penetrate with respect to grain size of the polycrystalline material. During release from metallic tin, instead, gas atoms do meet grain boundaries as they move freely at the interface between tin and the oxide skin, and therefore they do have a chance to diffuse via grain boundaries. Our experiments, e.g. the one recorded in Fig. 53, show that there is no grain boundary diffusion in SnO_2, at least up to $\sim$200°C.

Thus the lack of stage Ia in Fig. 51 is not simply due to the fact that the implanted ions do not have the possibility of being trapped at high mobility sites associated with grain-boundaries.

REFERENCES

1. Anderson, G.S., Wehner, G.K. and Olin, H.J., J. Appl. Phys. 34, (1963) 3492.

2. Behrisch R., Ergebuisse der exacten Naturwissenschaften, Springer, Berlin, 1964, p. 295.

3. Berman, R.M., Bleiberg, M.L. and Yeniscavich, W., J. Nucl. Mat. 2 (1960) 129.

4. Chin, F.K., private communication.

5. Davies, J.A., Brown, F. and McCargo, M. 1963 Can. J. Phys. 41, 829.

6. Domeij, B., Brown, F., Davies, J.A., and McCargo, M., Can. J. Phys. 42, (1964) 1624.

7. El-Shanshoury, I.A., Rudenko, V.A. and Ibrahim, I.A., J. Am. Ceram. Soc. 53 (5) 264 (1970).

8. Fairfield, J.M. and Crowder, B.L., Trans. Metallurg. Soc. AIME 245, (1969) 469.

9. Fassler, A., Z. Krist. 104 (1942) 81.

10. Garvie, R.C., J. Phys. Chem. 69 (4) 1238 (1965).

11. Gianolo, U., J. Appl. Phys. 28 (1957) 868.

12. Gillam, E., Phys. Chem. Solids, 11, 55 (1959).

13. Glang, R., Holmwood, R.A. and Herd, S.R., J. Vac. Sci. Technol. 4 (1967) 163.

14. Gonser, V. and Okkerse, B., J. Phys. Chem. Solids 7 (1958) 55.

15. Groth R., Kauer, E. and Van der Linden, Z. Naturf. 17a, (1962) 789-793.

16. Hardy, W.R., Shewchun, J., Kuenzing, D. and Tam, C., private communication.

17. Hartshorne, N.H., Disc. Faraday Soc. 5, 149 (1949).

18. Hauser, O. and Schenk, M., Kervenergie 6 (1963) 655.

19. Hauser, O., and Schenk, M., phys. stat. sol. 6 (1964) 83.

20. Heinen, H., Lutz, H., and Sizmann, R., 1964 Z. Naturforsch. 19a, 1131.

21. Helwig, G., Z. Phys. 132 (1952) 621.

22. Holland, L., The Vacuum Deposition of Thin Films, John Wiley & Sons, Inc., New York, 1956.

23. Holland, L. and Siddal, G., Vacuum 3 (1953) 375.

24. Hollands, E. and Campbell, D.S., J. Mater. Sci., 3, 544 (1968).

25. Ishiguro, K., Sasaki, T., Arai, T. and Imai, I., J. Phys. Soc. Jap. 13, 296 (1958).

26. Izui, K. and Suzuki, H., J. Phys. Soc. Japan 18, (1963) Suppl. III, 210.

27. Jackson, N.F., Hollands, E.J. and Campbell, D.S., Proc. Joint IERE/IEE Conf. Applications of Thin Films in Electronic Engineering, Imperial College, July 1966, p. 13-1.

28. Jech, C. and Kelly, R., J. Phys. Chem. Solids 30 (1969) 465.

29. Kaminsky, M., Atomic and Ionic Impact Phenomenan, Springer, 1965, p. 142.

30. Kay, E., Advances in Electronics and Electron Physics, Academic Press, Vol. 17, 1962, p. 245.

31. Kelly, R. and Matzke, Hj., J. Nucl. Mat. 17 (1965) 179.

32. Kelly, R and Matzke, Hj., J. Nucl. Mat. 20 (1966) 171.

33. Kelly, R., Can. J. Phys. 46 (1968) 473.

34. Kelly, R. and Jech, C., J. Nucl. Mat. 30 (1969) 122-133.

35. Kelly, R., and Naguib, H.M., Atomic collision phenomena in solids, North-Holland Publishing Company (1970).

36. Kelly, R., phys. stat. sol. 30, 37 (1968).

37. Kennedy, T.N., Hakim, R. and Mackenzie, J.D., Mat. Res. Bull. 2 (2) 193 (1967).

38. Klasens, H.A. and Koelmans, H., Solid State Electronics 7 (1964) 701.

39. Kohnke, E.E., J. Phys. Chem. Solids 23, 1557 (1962).

40. Kubaschewski, O. and Hopkins, B.E., Oxidation of Metals and Alloys, 1st edn., Butterworth's Scientific Publications (London, 1953).

41. Lazarus, D., Solid State Phys. 10 (1960) 71.

42. Libbey-Owens-Ford Glass Co. and McMaster, H.A., Brit. Pat. 632, 256 (Oct. 1942).

43. Lieberman, M.L. and Medrud, R.C., J. Electrochem. Soc. 116 (2) 242 (1969).

44. Littleton, J.T., U.S. Pat. 2, 118, 795.

45. Loch, L.D., J. Elec. Chem. Soc. 110 (1963) 1081.

46. Maissel, L.I., Physics of Thin Films, Academic, Vol. 3, 1966.

47. Maissel, L.I. and Glang, R., Handbook of Thin Film Technology, McGraw-Hill, 1970.

48. Matzke, Hj. and Lindner, R., 1964, Atomkernenergie 9, 2.

49. Matzke, Hj., Z. Naturf. 22a, 507 (1967).

50. Matzke, Hj., Can. J. Phys. 46 (1968) 621.

51. Matzke, Hj. and Whitton, J.L., Can. J. Phys. 44 (1966) 995.

52. McMaster, H.A., U.S. Pat. 2,429, 420.

53. Meyer, O. and Mayer, J.W., J. Appl. Phys. 41 (10) 4166 (1970).

54. Mogab, C.J. and Kingery, W.D., J. Appl. Phys. 39 (8) 3640 (1968).

55. Nelson, R.S., Phyl. Mag. 11 (1965) 291.

56. Nghi, L.Q. and Kelly, R., Can. J. Phys. 48 (2) 137 (1970).

57. Ogilvie, G.J., Phys. Chem. Solids 10 (1959) 222.

58. Parsons, J.R., Phil, Mag. 12 (1965) 1159.

59. Parsons, J.R. and Balluffi, R.W., J. Phys. Chem. Sol. 25 (1964) 263.

60. Pöhlan, C., Lutz, H. and Sizman, R., Z. Augew, Phys. 17 (1964) 404.

61. Polezhaev, Yu. M., Russian J. Phys. Chem. 41 (11) 1590 (1967).

62. Powell, C., Oxley, J. and Blocher, Jr., J., Vapour Deposition (J. Wiley and Sons, Inc., New York, 1966). p. 398.

63. Preston, J.S., Proc. roy. Soc. A 202 (1950) 449.

64. Price, P.B. and Walker, R.M., J. Appl. Phys. 33 (1962) 2656, 3400.

65. Pringle, J.P.S., unpublished.

66. Rol, P.K., Fluit, J.M. and Kistemaker, J., Physica 26 (1960) 1009.

67. Rosenberg, D. and Wehner, G.K., J. Appl. Phys. 33, 1842 (1962).

68. Sarjeant, P.T. and Roy, R., J. Am. Ceram. Soc. 50 (1967) 500.

69. Shiojiri, M. Morikawa, H. and Suito, E., Sixth Int. Congress for Electron Microscopy, Kyoto (1966) 467.

70. Sigmund, P., Phys. Rev. 184 (2) 383 (1969).

71. Sinclair, W.R. and Peters, F.G., J. Am. Ceram. Soc. 46 (1) 20-23 (1963).

72. Sinclair, W.R., Peters, F.G., Stillinger, D.W. and Koonce, S.E., J. Electrochem. Soc. 112 (1965) 1096-1100.

73. Spence, W., J. Appl. Phys. 38 (1967) 3767.

74. Stech, B., Z. Naturforsch. 7a (1952) 175.

75. Teodorescu, I., Studii Cercetari Fiz. 18 (5), 511-24 (1966).

76. Trillat, J.J., J. Chem. Phys. 53 (1956) 510.

77. Turnbull, D. and Cohen, M.H., Modern Aspects of the Vitreous State, p. 38 Butterworth,London (1960).

78. Vainshtein, V.M., Simp. Protsessy Sin. Rosta Krist. Plenok Poluprov. Mater., Tezisy Dokl., Novosibirsk (1965) 3-5.

79. Valletta, R.M. and Pliskin, W.A., J. Electrochem. Soc. 114, 944 (1967).

80. Van der Maesen, F. and Witmer, C.H.M., Philips Research Lab. (1963).

81. Ward, J.W., Applications and Industry 16 (Jan. 1955) 408.

82. Wehner, G., Advances in Electronics and Electron Physics, Academic Press, Vol. 7, 1955, p. 239.

83. Weissmann, S., and Nakajima, K., J. Appl. Phys. 34 (1963) 3152.

84. Whitton, J.L., 1965, J. Appl. Phys. 36, 3917.

85. Williams, J.C., Sinclair, W.R. and Koonce, S.E., J. Am. Ceram. Soc. 46 (4) 161 (1963).

86. Yamanaka, S. and Ochashi, T., Japan, J. Appl. Phys. 8 (1969) 1058.

87. Hagel, W.C., J. Amer. Ceram. Soc. 48 (2), 70 (1965).

88. Holt, J.B. and Condit, R.H., Mater. Science Research 3 (1966) 13.

89. Holt, J.B., Proc. Brit. Ceram. Soc. 9 (1967) 157.

90. Hurst, D.G., Chalk River (Canada) Rep. CRRP-1124 (1962).

91. Kelly, R., Jech, C., and Matzke, Hj., phys. stat. sol. 25, 641 (1968).

92. Laurent, J.F. and Benard, J., Compt. rend. 241, 1204 (1955).

93. Laurent, J.F. and Benard, J., J. Phys. Chem. Solids 3, 7-19 (1957).

94. Laurent, J.F. and Benard, J., J. Phys. Chem. Solids 7, 218 (1958).

95. LeClaire, A.D. 1965. Diffusion in body-centered cubic metals (Am. Soc. Metals, Metals Park, Ohio), pp. 3-25.

96. Matzke, Hj., Lecture at the Summer School on the Physics of Ionized Gases, Herceg-Novi, Yugoslavia 1970.

97. Matzke, Hj., radiation effects 3 (1970) 93-105.

98. Oishi, Y. and Kingery, W.D., J. Chem. Phys. 33, 480, 1960.

99. Oishi, Y. and Kingery, W.D., J. Chem. Phys. 33, (1960) 905.

100. Paladino, A.E. and Kingery, W.D., J. Chem. Phys. 37 (5), 957-962 (1962).

101. Thompson, B.A., Ph.D. Thesis, Rensselaer Polytechnique Institute, 1962.

Errata

Fig. 36, 37..., 55 should have been numbered Fig. 33, 34, ..., 52 respectively (note in fact the discontinuity in figure numbers, since Fig. 32 is followed by Fig. 36).

References 87-101 are not in alphabetical order with respect to the rest of the references.